UNIVERSIDAD NACIONAL DE COLOMBIA

Role of the Al-doping and epitaxial strain in the multiferroic behavior of $TbMnO_3$ bulk and thin films

Thesis submitted to the physics department in partial fulfillment
of the requirements for the degree of Doctor of Sciences (Physics)
at the Universidad Nacional de Colombia, Medellín campus

By

Jorge Luis Izquierdo Núñez

Advisor

Oswaldo Morán Campaña, Dr. rer. nat.

Medellín, 2017

Declaration

I declare that the work contained herein is my own work and that all supporting work has been noted and fully referenced. No portion of the work referred to in this thesis has been submitted in support of an application for another degree or qualification of this or any other university or institute of learning.

Signed .....

Jorge Luis Izquierdo Núñez

Supervisory committee

The undersigned have examined the thesis entitled Role of the Al-doping and epitaxial strain in the multiferroic behavior of $TbMnO_3$ bulk and thin films presented by Jorge Luis Izquierdo Núñez, a candidate for the degree of Doctor of Sciences (Physics) and hereby certify that it is worthy of acceptance.

_____ _____

Date Dr. Oswaldo Morán Campaña -Advisor

_____ _____

Date Dr. Álvaro Mariño Camargo -committee member

_____ _____

Date Dr. Carlos A. Parra Vargas -committee member

_____ _____

Date Dr. Juán M. Meza Meza -committee member

Acknowledgments

Firstly I would like to express my deepest thanks to Dr. Oswaldo Morán Campaña for all the support, guidance and advice throughout all the stages of my studies.

I would like to acknowledge the financial support from the Universidad Nacional de Colombia, Medellín Campus as well as the logistic support of the low-temperature group at the Universidad del Cauca in Popayán. Particularly, I thank Dr. Gilberto Bolaños, Ing. Alexánder Astudillo and Ing. Jonathan Martínez for the assistance with the sputtering system.

I would like to thank the professional and opportune assistance of MSc., Adrian Gómez with the XRD characterization.

Thanks are also extended to Dr. Diego Rubí, at the Comisión Nacional de Energía Atómica (CNEA) for their disposition and collaboration with the internship contract realized in Buenos Aires - Argentina

Finally, I would like to give thanks to my parents, brothers, Blanca and Maria Fernanda for their unconditional support.

Table of contents

Summary

The Ph.D. thesis reports on the experimental investigation of the structure and physical properties of the perovskite-type multiferroic $TbMnO_3$ when doped with aluminum ions in different atomic positions. The study is carried out both in bulk form and thin films. In thin film form, the material is additionally submitted to compressive/tensile epitaxial strain. Multiferroic compounds are a novel class of material, which feature both spontaneous electrical polarization and magnetization, within the same phase. Multiferroics are rare in nature and many research groups around the world have directed their efforts to the discovery/synthesis of new multiferroics. The main interest in this class of materials is the possibility of observing high magnetoelectric response in them. A strong coupling between the electrical and magnetic orders in these materials would open a wide spectrum of potential applications in spintronics and/or non-volatile 4-state memories. Nevertheless, the reported couplings up to now are still too weak, which hampers the practical applications. In this regard, plausible ways to enhance the response of the material are the use of an appropriate dopant (chemical pressure), the application of an external pressure or epitaxial strain. Whereas the theoretical aspects of the fundamental mechanisms related to the appearance of multiferroicity in some materials has experimented considerable advance over the last few years, the discovery or creation of new systems with enhanced magneto(-di) electric response represent a challenge for disciplines such as solid state physics and materials sciences.

The main objective of this thesis is to study the role of chemical doping and epitaxial strain on the structure and physical behavior of a multiferroic material. $TbMnO_3$ was chosen as test multiferroic because its spontaneous electrical polarization, due to a spiral spin ordering,

gives rise to a large magnetoelectric coupling. Furthermore, large strain effects are to be expected in such system because of the subtle balance between the magnetic interactions and its large magnetic frustration. For these reasons, a detailed study on the structure and properties of Al-doped $TbMnO_3$, both in bulk and thin film form, has been conducted in this thesis. We motivate the interest of fabricating thin films of $TbMnO_3$ because this allows one to visualize the effect compressive/tensile strain on the magnetic response of this challenging multiferroic.

In chapter 1, we introduce the multiferroic and magnetoelectric materials and their interest from the fundamental and from the applications point of view, as well as the compound subject of this thesis, $TbMnO_3$. The synthesis of bulk $TbMnO_3$ as well as the growth and study of thin films are introduced in chapter 2. In the same chapter, we present the experimental tools used for the characterization of the samples including high-resolution X-ray diffraction X-ray photoelectron spectroscopy, atomic force microscopy, electrical, magnetic and dielectric characterization techniques.

In chapter 3, we present and discuss the results achieved on undoped and Al-doped bulk $TbMnO_3$ samples synthesized by solid state reaction. In particular, the XRD patterns show that the Al ions are effectively entering in the crystalline structure of $TbMnO_3$. A clear distinction between de doping at the Tb and Mn places is observed. The Rietved refinement of the XRD patterns corroborates this assertion. The effect of the Al-doping is also evident from the results of the (di-)electrical, and magnetic measurements. Indeed, the Al-doping leads to a decrease in the value of the electrical resistance and consequently to an increase in the value of the conductance. Impedance analysis allowed us to separate the different contributions to the dielectric response and revealed Debye-like relaxation mechanisms. As to the magnetic response, it was shown that the dominant magnetic interactions in the

$TbMnO_3$ bulk material films are antiferromagnetic. Nevertheless, the doping with Al ions suggests that ferromagnetic interactions are present in the bulk samples below the Neel temperature, evidenced by a splitting between the field-cooled (FC) and zero-field-cooled (ZFC) magnetization curves. Although the origin of the ferromagnetic in this multiferroic is controversially discussed, it is generally accepted that the lattice distortion caused by the Al-doping is behind the effect. The thermal characterization of the bulk samples show that the system has a quite high Seebeck coefficient and a relatively low thermal conductivity, which would make the $TbMnO_3$ multiferroic a promissory thermoelectric material. Nevertheless, the low electrical conductivity at low temperatures conduces to a low figure of merit, which certainly hinders the practical applications of this material.

The growth, structure and properties of the $TbMnO_3$ thin films grown under compressive/tensile strain on single crystals of atomically flat MgO and $SrTiO_3$ substrates is reported in chapter 4. Films with different orientations are obtained on each substrate material and for different growing parameters. In spite of this, all films show well-defined ferromagnetic signal below the Curie temperature, which also varies according the substrate and growing parameters chosen. By optimizing the growing parameters, thin films can be epitaxialy grown on (001)-oriented $SrTiO_3$ substrates. The films (50-150 nm) show orthorhombic distortion and are partially relaxed. Thus, it is probable that a strained and a relaxed part coexist in the films with thicknesses within the range previously mentioned. The main results in this chapter can be summarized as follows: **a**. the successful stabilization of undoped and Al-doped $TbMnO_3$ thin films under compressive strain on $SrTiO_3$ substrates when sputtering is used as physical deposition technique. **b**. the magnetic measurements performed on the films show that the dominant magnetic interactions in the thin films are antiferromagnetic, similar to the bulk material, but that ferromagnetic interactions are present

in the undoped films below the Neel temperature. The magnetic response of the films is clearly improved upon Al-doping, which corroborates the central role of the chemical pressure in the magnetic behavior of the studied system. The orthorhombic distortion seems to be a good candidate to explain the origin of the induced ferromagnetism in the films. However, some reports found in the literature on the concerned system suggest apart from the structural distortion, the presence of domain walls can equally causes the ferromagnetism in the $TbMnO_3$ films. Although it is evident that further work is necessary in order to acquire a deeper insight into the multiferroic behavior of $TbMnO_3$, the results presented in this thesis contain valuable information that will contribute to extend the general knowledge on the $TbMnO_3$ multiferroic existent in the literature on the thematic.

Chapter 1

General introduction

1.1 Multiferroic materials

Recent years have seen an enormous increase in research activities in the field of multiferroic materials and magneto-electric effects. In December 2007 the Science Magazine listed multiferroic materials as one out of ten areas to watch in 2008, the only entry from the materials science/condensed matter area that was included in this list. By taking the original definition put forward by Schmid [1] into account, multiferroic materials are materials that combine two or more of the primary forms of ferroic order, i.e. ferroelasticity, ferroelectricity, and ferromagnetism. In practice, most of the recent research activities have focused on materials that combine some form of magnetic order (ferromagnetic, antiferromagnetic) with ferroelectricity. Hence, the term multiferroics is nowadays often used synonymous with magnetic ferroelectrics. Due to the combination of magnetic and dielectric properties, with eventual cross-coupling between these properties, multiferroics have immense potential for technological device applications and at the same time they pose very interesting and rich fundamental physics problems. It is probably this combination of applied and fundamental research that is partly responsible for the strong attraction that these materials have woken up in recent years.

Research on multiferroics (or magnetic ferroelectrics) is also intimately interwoven with research on the magnetoelectric effect, which is the property that in certain materials a magnetic field induces an electric polarization and, conversely, an electric field induces a magnetization. Traditionally, one distinguishes between linear, quadratic, and higher order

magneto-electric effects [2], but more recently the term magneto-electric effect is often (mis-)used to describe any form of cross-correlation between magnetic and (di-) electric properties. An example of this cross-correlation is the fact that the application of an external magnetic field may induce a phase transition between ferroelectric/non-ferroelectric phases. Here, it is important to note that not every magnetic ferroelectric exhibits a linear magneto-electric effect (in the original sense) and that not every material that exhibits a linear magneto-electric effect is also simultaneously multiferroic.

The search for materials showing the magnetoelectric effect began with the prediction of a possible magnetoelectric coupling [3]. The effect was then rapidly observed in Cr_2O_3 [4]. The renewed interest in the magnetoelectric effect during the last years is due to its potential for data storage and other applications [5]. Figure 1.1 shows the relationship between multiferroic and magnetoelectric materials, within the broader class of materials that are susceptible to polarize or magnetize under electrical or magnetic fields.

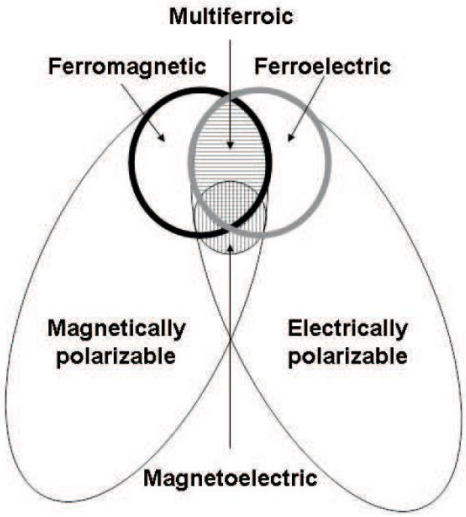

Figure. 1.1. Shown by black (grey) circle are ferromagnetic (ferroelectric) materials which possess spontaneous magnetization (polarization). The horizontally hatched region represents the multiferroics, i.e. materials in which both a spontaneous polarization and magnetization are present within the same phase. The vertical hatched region corresponds to the magnetoelectric materials, in which both the electrical and magnetic properties are coupled linearly to both applied magnetic and electrical fields. This figure has been adapted from reference [5].

Figure 1.1 shows that not all multiferroics display magnetoelectric coupling and that not all materials exhibiting magnetoelectric coupling are multiferroics. However, it is believed that the largest magnetoelectric coupling is to be found among the multiferroic materials. The nature of the coupling in multiferroic and magnetoelectric materials is still not fully understood and has attracted much interest in the past years.

Currently there is renewed interest in studying the perovskite-based multiferroic materials, such as the rare earth manganites $TbMn_2O_5$, $YMnO_3$, $BiMnO_3$, $HoMnO_3$ etc., which have been shown to display large magnetoelectric effect [6]. Although ferromagnetic multiferroics are preferred for applications, most of the multiferroics under investigation are antiferromagnets. This is because very few ferromagnets are good insulators, an important requirement for ferroelectricity [7]. In this connection, the $TbMnO_3$ (TMO) manganite seems to be one of those few materials in which the magnetic and electric ordering coexist in a close range of temperatures [8]. This material is considered to be one of the representative materials of the so called type II multiferroics [9], in which ferroelectricity is induced by the magnetic ordering. Anomalies in TMO single crystals have been observed at the Neel temperatue T_N=41 K, where the Mn^{3+} magnetic moments have sinusoidal antiferromagnetic (AF) order. At T_{lock}~27 K electric polarization appears, which increases to 800 $\mu C/m^2$ by decreasing temperature. At T_{N2}=7 K, the Tb^{3+} magnetic moments show a quasi-long-range-AF ordering [10]. Furthermore, it has been reported that polycrystalline TMO doped with other elements such as Na (in the Tb site) produces a shift of the AF ordering of the Tb^{3+} ions toward higher temperatures [11].

Similar to other technologically interesting materials, recent efforts have been made to synthesize new multiferroics in the form of thin films, which is desirable for some

applications [7, 12, 13]. Here, interesting substrate effects, due to the epitaxial strain, may be obtained such as stabilization of new phases that do not exist in bulk, modifications of the ferroelectric and magnetic exchange interactions or changes in electronic properties. Strain effects may be difficult to assess due to extrinsic effects such as secondary phases, difficulties in the synthesis of good quality materials and issues related to the characterization of very small volumes of material present in thin films. Therefore, a definitive explanation of the role of strain in multiferroic materials has still not been formulated. Owing to the fact that the main exchange interactions are sensitive to changes in the metal-oxygen bond angle and bond distances, not only the investigation of the physical response but also an exhaustive study of the structure is essential for understanding the physics behind epitaxial strain effects.

The proposed thesis is aimed to address the role of strain on the multiferroic behavior of the orthorhombic perovskite TMO. The strain will be generated by chemical pressure (doping with Al), epitaxial strain (deposition of thin films on crystalline substrates) or combination of both. As stated above, the structural distortion of the orthorhombic perovskite unit cell may lead to large modifications of the ferroelectric, magnetic and electronic properties of rare earth manganites. The fabrication of TMO in thin film form has the advantage of allowing one to change the crystallographic structure without modifying the cation on the transition metal or rare earth site. This, in turn, enables a detailed understanding of the relationships between the structure and the physical properties of the material in thin film form. The ultimate goal of this thesis is to try to tune the physical properties of TMO using chemical pressure and/or epitaxial strain, imposed by the substrate.

1.2 State of the art

Magnetic and ferroelectric materials have permeated every aspect of modern science and technology. For example, ferromagnetic materials with switchable spontaneous magnetization, *M*, driven by external magnetic field *H*, have been widely used in data storage industries. The discovery of the giant magnetoresistance effect (GMR) significantly promoted magnetic memory technology and incorporated it into the fascinating new technology called magnetoelectronics or spintronics. The fundamental and application issues associated with magnetic random-access memories (MRAMs) and related devices have intensively been pursued in order to achieve high-density integration and also overcome the large hurdle concerning the relatively high energy consumption by writing [14]. On the other hand, the sensing and actuation industry relies mainly on ferroelectric materials with spontaneous polarization *P*, reversible upon an external electric field *E*. Most ferroelectrics materials, especially those based on perovskite oxides, are high-performance ferroelastics or piezoelectrics with spontaneous strain. The coexistence of strain and polarization allows these materials to be used in a broad variety of applications, in which elastic energy is converted into electric energy or vice versa [15]. In addition, there has been continuous effort to promote the use of ferroelectric random-access memories (FeRAMs) [16] as novel non-volatile and high-speed memory media whose performance would be superior to semiconductor flash memories. In this sense, novel prototype devices based on multiferroic functions may offer particularly high performance for spintronics. For instance, the electric field necessary to reverse the spin states can also be used for writing the polarization states, which would contribute to overcome the high-writing energy required in magnetic random-access memories.

Although ferroelectricity and magnetism have been the focus of condensed matter physics and materials science since their discovery, a considerable number of issues challenges in dealing with multiferroicity have emerged both in aspects of fundamental physics and technological applications. There are, in principle, two basic issues to address in order to make multiferroicity physically understandable. The first one is the coexistence of ferroelectricity (electric dipole order) and magnetism (spin order) in one system (composite integration strategies for the two types of functions are excluded). In fact, the coexistence of two or more ferroic orders is quite hard to achieve because in most conventional ferroelectrics, the chemical bonding, which results in an off-centre position of the transition metal ions creating electric polarization, requires a formally empty *d*-electron band configuration [17]. Nevertheless, ferromagnetism requires unpaired *d* electrons, i.e. occupied *d*-bands. Then, the coexistence of the two properties seems to be incompatible with the local chemistry [17]. Nevertheless, the nontrivial problem of finding the microscopic conditions by which the two orders can coexist intrinsically in one system is still a current and exciting research subject occupying a many research groups around the world. The second issue is related with the fact that an efficient magnetoelectric coupling between the two orders in a multiferroic system seems to be even more important than their coexistence. This is so because such a magnetoelectric coupling represents the basis for multi-control of the two orders by either electric field or magnetic field. Investigations have demonstrated that a realization of such strong coupling has been even more challenging and, thus, it has become the core of recent research activity in the field of multiferroic materials.

Multiferroics constitute a very diverse class of materials and there is no unique theory of multiferroics. Thus, every material has practically to be studied on its own right, and

eventually involves very different physical mechanisms [18]. However, it has proven to be very useful to classify different multiferroics according to the mechanism that drives the ferroelectricity in the corresponding system [18]. In particular two major classes of multiferroics may be distinguished, namely: (1) Multiferroics, where the ferroelectricity is driven by hybridization and covalency or other purely structural effects. (2) Multiferroics, where the ferroelectricity is driven by some other electronic mechanism, e.g. correlation effects. Here, ferroelectricity always arises as a secondary effect that is coupled to some other form of ordering such as magnetic-or charge-ordering. Therefore, these systems may be classified as improper magnetic ferroelectrics. On the other hand, most materials in the first category are proper magnetic ferroelectrics where both the polarization and the magnetic order are primary order parameters that nevertheless may exhibit some coupling between them. Here, it is important to note that the hexagonal $YMnO_3$, belonging to the first class of multiferroics, has been classified as an improper ferroelectric. Although electric polarization is coupled to a different non-polar structural instability [19], polarization is not the primary order parameter.

As previously stated, the coexistence of two or more ferroic orders, particularly ferromagnetism and ferroelectricity, seems to be incompatible with the local chemistry. Therefore, non-conventional mechanisms are needed to explain the occurrence of multiferroicity in current materials and to design new multiferroics. Initially, partial substitution of ferroelectrics with paramagnetic cations was proposed [20]. In this case, the requirements for the *d*-shell are met and one crystallographic site may contain both an empty *d*-shell cation and a partially filled *d*-shell cation [20]. Examples of compounds where this mechanism is active are $PbFe_{1/2}Nb_{1/2}O_3$ [21]. Another mechanism leading to multiferroic

behavior is related to the possibility of using the stereochemical activity of Bi^{3+} and/or Pb^{2+} lone pairs, as in the case of $PbVO_3$, $BiFeO_3$ or $BiMnO_3$, although the multiferroic nature of $BiMnO_3$ is still not clear [22]. In such compounds, the ferroelectric distortion is caused by the 6*s* lone pair, while Fe/Mn/V are responsible for the magnetism [23]. Nevertheless, as ferroelectricity and magnetism in these materials have different origin, the coupling between these two properties is generally weak [17]. Other interesting mechanism is based on the fact that the polar state may be induced by an unconventional type of ordering such as in the geometric ferroelectrics. In these materials, the structure is distorted in a complex way. Hexagonal $YMnO_3$ is an example of such a multiferroic in which ferroelectricity is induced by a tilting of the MnO_5 bipyramids and buckling of the Y-O planes [24]. Another mechanism relates to charge ordering. In some materials, charge ordering may give rise to polarization. This was theoretically predicted and observed for $LuFe_2O_4$ [25]. Finally, important cases, in terms of the magnitude of the coupling, are those in which the polar state is directly induced by the magnetic ordering. Examples of such systems are the spiral magnets. In these materials, the polar state arises from the breaking of inversion symmetry by a spin cycloidal structure [26]. The TMO belongs to this class of spiral magnets.

1.3 Approach to the problem

1.3.1 Why perovskites?

Complex transition metal oxides are fascinating materials both from a basic science perspective as well as from a technological viewpoint (see Fig. 1.2). The unique electronic structure of these materials leads to a very strong coupling between structural, electronic, and magnetic properties. To understand this complex interplay between the various degrees of freedom is a great challenge for modern condensed matter physics. In addition, the same

interplay leads to a tremendous variety of physical properties, such as metallic, semiconducting, or insulating behavior, piezoelectricity, ferroelectricity, ferromagnetism, metal-insulator transitions, and high temperature superconductivity. These functional properties are extremely attractive for applications in modern electronic devices such as nonvolatile memories or new types of sensors and actuators. Thus, this kind of materials offers great perspectives for the development of future technologies. The unique features of transition metal oxides are a result of the partial occupation of the electronic *d* shell on the transition metal cation. The corresponding electronic orbitals are intermediate between being atomic-like and band-like, i.e. between being localized at the cation sites and being delocalized throughout the crystal by the formation of covalent chemical bonds. The extent to which these *d*-electrons form chemical bonds crucially depends on transition metal-oxygen bond length, bond angle (the angle formed by a transition metal-oxygen-transition metal structural unit), and the symmetry of the crystal-field, which is caused by the anion polyhedra surrounding the metal cation. One very common and probably the most studied crystal structure of complex transition metal oxides, the perovskite structure, is depicted in Fig. 1.3. In the perovskite structure the transition metal cations form a simple cubic lattice and are surrounded by octahedra of oxygen anions. The non-transition metal cations occupy the space in between these octahedra. Small distortions from the perfect perovskite structure or small changes in volume or electron configuration by e.g. doping may alter the nature of the orbitals becoming either more localized or more covalent. This, in general, can decidedly affect the degree and overall character of the magnetic ordering.

In spite of an apparent simplicity, perovskite-based materials are interesting systems due to the possibility of synthesize a large variety of possible chemical compositions, which show

amazing physical properties such as giant piezoelectricity, ferroelectricity, high-temperature superconductivity, giant magnetoresistance, etc. The large palette of properties is due to the high flexibility of the structure, i.e. possibility to adopt a series of small structural transformation such as tilting of oxygen-based octahedra and displacement of cations in different crystallographic directions as illustrated in Fig. 1.2. The structural transformation form complicated systems of ferroelectric domains and accommodate different types of structural disorder. One of the central problems is to understand the arrangement of ferroelectric and ferroelastic twin domains, which naturally appear upon the transition of a material from higher symmetry (cubic and paraelectric) to a lower symmetry (ferroelectric) phase.

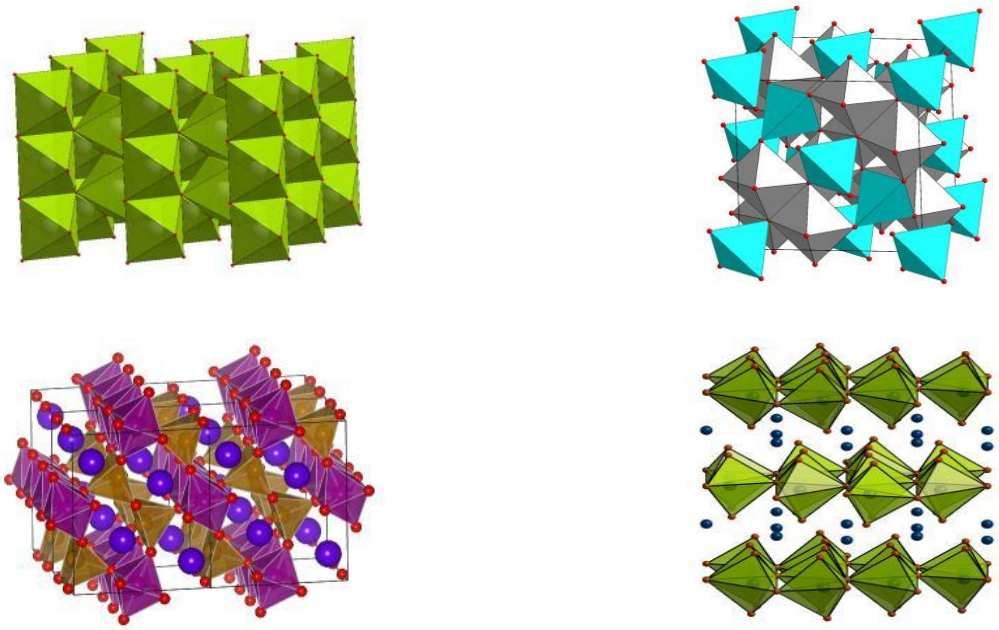

Figure. 1.2. Crystal structures of some complex transition metal oxides. Rutile VO_2 (top left) exhibits a metal-insulator transition coupled to a structural distortion. The spinel structure (general chemical composition AB_2O_4, top right) is adopted by many magnetic oxides. $TbMn_2O_5$ (bottom left) and $YMnO_3$ (bottom right) are examples of multiferroic materials that exhibit ferroelectricity simultaneously with magnetic order [27].

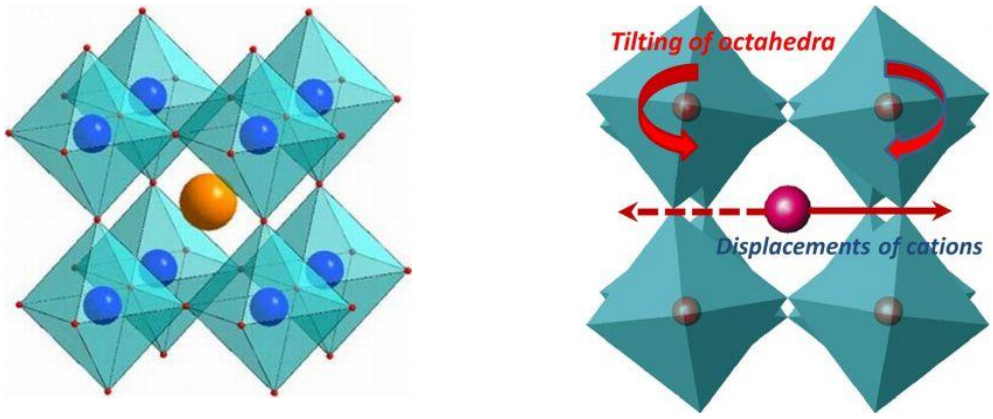

(a) (b)

Figure. 1.3. Ideal cubic perovskite structure (a) and distorted perovskite structure (b) as found for instance in $LaMnO_3$. The transition metal cations are located in the centers of octahedra formed by oxygen anions. The intermediate space is filled with non-transition metal cations (generally, this space is occupied by rare earth elements, such as Tb or Y). The small tilting of the oxygen octahedra (b) may lead to dramatically different physical properties of the compound [27].

The same strong coupling between structural, electronic, and magnetic degrees of freedom that result in the fascinating spread of properties in complex transition metal oxides on the other hand also represents an obstacle for the accurate experimental synthesis and characterization of these materials. Small changes in composition or the accidental presence of impurities or other defects can alter the properties significantly. It is therefore very important to carry out an exhaustive control of all parameters involved in the synthesis of the material both in bulk and in thin film form. It is also important to have reference models that provide means for obtaining an improved understanding of the underlying physics of the compounds which, in turn, will guide the experimental research efforts towards a reliable technological application of these promising materials.

1.3.2 Manganites thin films

It is forssen from the previous discussion that the fully understanding of the physical phenomena in complex systems needs the fabrication of single crystalline materials.

Nevertheless, the growth of high-quality single crystals can became a cumbersome, time-consuming, and expensive procedure for many novel oxides. In some cases, the complex crystal structures hamper the achievement of high quality single crystals to systematically study their interesting anomalous physical properties. Therefore, highly epitaxial thin films grown on crystalline substrates offer an alternative route for exploring the nature of these physical phenomena. In addition, for many applications in fields like sensing or reading/writing devices high-quality thin films are highly desirable. In this regard, recent progress in thin film fabrication together with advanced computational modeling facilitates the rational design of atomic scale devices with formerly unachievable properties. Complex transition metal oxides are extremely attractive for this purpose due to their great chemical and structural flexibility. Rare earth manganites ($RMnO_3$, R=rare earth ion) in thin film form have successfully been prepared by means of physical and chemical methods. The most studied system has being $LaMnO_3$ due to the observation of colossal magnetoresistance in bulk samples upon doping by Sr, Ba or Ca. For the current thesis project, high quality thin films of the multiferroic TMO (undoped and doped with Al ions) were grown by the author of this thesis at the low temperature laboratory in the Universidad del Cauca, Popayán (Colombia) using dc-magnetron sputtering technique. This research group is a part of the national collaboration established some years ago to the growth of oxide thin film by dc sputtering.

1.4 Theory

1.4.1. Compounds with perovskite-type structure

The relatively simple chemistry and structure of perovskites is very helpful when epitaxial growth is pursued. Several ferromagnets, diverse ferroelectrics and some of the most

important multiferroic materials feature perovskite-type structure. The general formula for perovskite-based materials is ABO_3, where A and B are cations with different sizes and/or valences. Normally, these sites are occupied by a lanthanide and transition metal elements [(Fig. 1.3(a)]. The B cation is located at the centre of 6 oxygen atoms with an octahedral coordination. The ideal perovskite structure is cubic, as shown in figure 1.3 (a) or 1.3 (b). The distortion of the perovskites from the cubic symmetry is measured by the so-called tolerance factor, defined by Goldschmidt according to the relationship: $t = (r_A + r_O)/\sqrt{2}(r_B + r_O)$. Here, r_A, r_B and r_O represent the ionic radii of A cation, B cation and oxygen O, respectively. Almost all perovskites have a tolerance factor between 0.75 and 1. The distortion of the unit cell increases as the tolerance factor decreases from 1, being this value for an ideal cubic perovskite.

1.4.2. Crystal field theory

Crystal field theory (CFT) is a model that describes the breaking of degeneracies of electronic orbital states, usually *d* or *f* orbitals, due to a static electric field produced by a surrounding charge distribution (anion neighbors). This theory has been used to describe various spectroscopies of transition metal coordination complexes, in particular optical spectra (colors). CFT successfully accounts for some magnetic properties, colors, hydration enthalpies, and spinel structures of transition metal complexes, but it does not attempt to describe bonding. CFT was developed by physicists Hans Bethe and John Hasbrouck van Vleck [28] in the 1930s. CFT was subsequently combined with molecular orbital theory to form the more realistic and complex ligand field theory (LFT), which delivers insight into the process of chemical bonding in transition metal complexes. According to CFT, the interaction between a transition metal and ligands arises from the attraction between the

positively charged metal cation and the negative charge on the non-bonding electrons of the ligand. The theory is developed by considering energy changes of the five degenerate *d*-orbitals upon being surrounded by an array of point charges consisting of the ligands. As a ligand approaches the metal ion, the electrons from the ligand will be closer to some of the *d*-orbitals and farther away from others causing a loss of degeneracy. The electrons in the *d*-orbitals and those in the ligand repel each other due to repulsion between like charges. Thus, the *d*-electrons closer to the ligands will have a higher energy than those further away which results in the *d*-orbitals splitting in energy. This splitting is affected by the following factors:

- The nature of the metal ion.
- The metal's oxidation state. A higher oxidation state leads to a larger splitting.
- The arrangement of the ligands around the metal ion.
- The nature of the ligands surrounding the metal ion. The stronger the effect of the ligands the greater the difference between the high and low energy *d* groups.

The most common type of complex structures is the octahedral one. Here, six ligands form an octahedron around the metal ion. In octahedral symmetry the *d*-orbitals split into two sets with an energy difference, Δ_{oct} (the crystal-field splitting parameter) where the d_{xy}, d_{xz} and d_{yz} orbitals will be lower in energy than the d_z^2 and $d_{x^2-y^2}$, which will have higher energy, because the former group is farther from the ligands than the latter and therefore experience less repulsion. The three lower-energy orbitals are collectively referred to as $\mathbf{t_{2g}}$, and the two higher-energy orbitals as $\mathbf{e_g}$. (These labels are based on the theory of molecular symmetry). Typical orbital energy diagrams are presented below.

Tetrahedral complexes are the second most common type; here four ligands form a tetrahedron around the metal ion. In a tetrahedral crystal field splitting the *d*-orbitals again

split into two groups, with an energy difference of Δ_{tet} where the lower energy orbitals will be d_z^2 and $d_{x^2-y^2}$, and the higher energy orbitals will be d_{xy}, d_{xz} and d_{yz} - opposite to the octahedral case. Furthermore, since the ligand electrons in tetrahedral symmetry are not oriented directly towards the *d*-orbitals, the energy splitting will be lower than in the octahedral case. Square planar and other complex geometries can also be described by CFT.

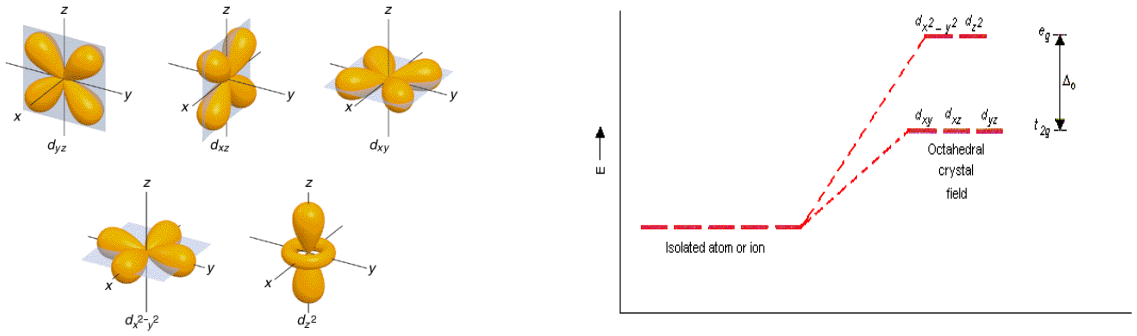

Figure. 1.4. (a) Configurations of the *d* orbitals. (b) Energy splitting for the *d* orbital in octahedral configuration

The size of the gap Δ between the two or more sets of orbitals depends on several factors, including the ligands and geometry of the complex. Some ligands always produce a small value of Δ, while others always give a large splitting. The reasons behind this can be explained by ligand field theory. The spectrochemical series is an empirically-derived list of ligands ordered by the size of the splitting Δ that they produce (small Δ to large Δ). The ligands producing the most splitting are those that may engage in metal to ligand back-bonding. The oxidation state of the metal may also contribute to the size of Δ between the high and low energy levels. As the oxidation state increases for a given metal, the magnitude of Δ increases. A V^{3+} complex will have a larger Δ than a V^{2+} complex for a given set of ligands as the difference in charge density allows the ligands to be closer to a V^{3+} ion than to a V^{2+} ion. The smaller distance between the ligand and the metal ion results in a larger Δ,

because the ligand and metal electrons are closer together and therefore the repulsion is stronger.

1.4.3. Spin states for *d* electrons

Within the description of transition metal coordination complexes, the term spin states refers to the potential spin configurations of the metal center's *d* electrons. Generally speaking, these spin states vary between high-spin and low-spin configurations. These configurations may be understood through the two major models used to describe coordination complexes, namely ligand field theory, which is an application of molecular orbital theory to transition metals, and crystal field theory, which has roots in the valence shell electron pair repulsion (VSEPR) theory [29]. The VSEPR rules are a model in chemistry used to predict the shape of individual molecules based upon the extent of electron-pair electrostatic repulsion. The VSEPR theory rely on the fact that the valence electron pairs surrounding an atom mutually repel each other, and will therefore adopt an arrangement that minimizes this repulsion. This determines then the molecular geometry. The number of atoms bonded to a central atom plus the number of lone pairs of its nonbonding valence electrons is called its steric number. VSEPR theory is usually compared and contrasted with valence bond theory, which addresses molecular shape through orbitals that are energetically accessible for bonding. Molecular orbital theory is another model for understanding how atoms and electrons are assembled into molecules and polyatomic ions.

As it was stated previously, the Δ splitting of the *d*-orbitals plays an important role in the electron spin state of a coordination complex. Factors like the period and the charge of the metal, and the field strength of the complex's ligands affect the magnitude of Δ. Ligands

which cause a large splitting Δ of the *d*-orbitals (e.g. CN^- and CO) are referred to as strong-field ligands. In complexes with these ligands, it is unfavorable to put electrons into the high energy orbitals. Therefore, the lower energy orbitals are completely filled before population of the upper sets starts according to the Aufbau principle. Complexes such as this are called low-spin (filling an orbital matches electrons and reduces the total electron spin). Thus, the condition for occurrence of low-spin splitting supposes that the energy cost of placing an electron into an already singly occupied orbital must be less than the cost of placing the additional electron into an e_g orbital at an energy cost of Δ. For example, NO_2^- is a strong-field ligand and produces a large Δ. The octahedral ion $[Fe(NO_2)_6]^{3-}$, which has 5 *d*-electrons, would have the octahedral splitting diagram shown in Fig. 1.5 (a) with all five electrons in the t_{2g} level. On the other hand, if the energy required to pair two electrons is greater than the energy cost of placing an electron in an e_g, high spin splitting occurs (populating the upper orbital avoids matches between electrons with opposite spin). In this regard, ligands (like I^- and Br^-), which cause a small splitting Δ of the *d*-orbitals, are referred to as weak-field ligands. As already mentioned, in this case, it is easier to put electrons into the higher energy set of orbitals than it is to put two into the same low-energy orbital, because two electrons in the same orbital repel each other. So, one electron is put into each of the five *d*-orbitals before any pairing occurs in concordance with Hund's rule and high-spin complexes are formed. For instance, Br^- is a weak-field ligand and produces a small Δ_{oct}. So, the ion $[FeBr_6]^{3-}$, with five *d*-electrons, would have an octahedral splitting diagram where all five orbitals are singly occupied [Fig. 1.5 (b)]. As noted above, e_g refers to the d_z^2 and $d_{x^2-y^2}$ which are higher in energy than the t_{2g} in octahedral complexes. If the energy required to pair two electrons is greater than the energy cost of placing an electron in an e_g, high spin splitting occurs.

(a) (b)

Figure. 1.5. (a). Low-spin $[Fe(NO_2)_6]^{3-}$ crystal field diagram (b) High Spin $[FeBr_6]^{3-}$ crystal field diagram

Within a transition metal group, moving down the series corresponds with an increase in Δ. The observed result is larger Δ splitting for complexes in octahedral geometries based on transition metal of the second or third row, periods 5 and 6 respectively. This Δ splitting is generally large enough that these complexes do not exist in a high-spin state. This is true even when the metal center is coordinated to weak field ligands. Octahedral coordination complexes which are centered on first row transition metals are the only ones fluctuating between high and low-spin states. The charge of the metal center also plays a role in the ligand field and the Δ splitting. For example, Fe^{2+} and Co^{3+} are both d^6. However, the higher charge of Co^{3+} creates a stronger ligand field than Fe^{2+}.

The crystal field splitting energy for tetrahedral metal complexes (four ligands) is referred to as Δ_{tet}, and is roughly equal to $(4/9)\Delta_{oct}$ (for the same metal and same ligands). Therefore, the energy required to pair two electrons is typically higher than the energy required for placing electrons in the higher energy orbitals. Thus, tetrahedral complexes are usually high-spin.

The use of the splitting diagrams may aid to the prediction of the magnetic properties of coordination compounds. A compound that has unpaired electrons in its splitting diagram will be paramagnetic and will be attracted by magnetic fields, while a compound that lacks

unpaired electrons in its splitting diagram will be diamagnetic and will be weakly repelled by a magnetic field.

1.4.4. Crystal field stabilization energy

The crystal field stabilization energy (CFSE) is the stability that results from placing a transition metal ion in the crystal field generated by a set of ligands. It arises due to the fact that when the *d*-orbitals are split in a ligand field (as described above), some of them have lower energies with respect to a spherical field known as the barycenter in which all five *d*-orbitals are degenerate. For example, in the octahedral case, the t_{2g} set has lower energy than the orbitals in the barycenter. As a result, if there are any electrons occupying these orbitals, the metal ion is more stable in the ligand field relative to the barycenter by an amount known as the CFSE. Conversely, the e_g orbitals (in the octahedral case) have higher energies than those in the barycenter, so putting electrons in these orbitals reduces the amount of CFSE (Fig. 1.6).

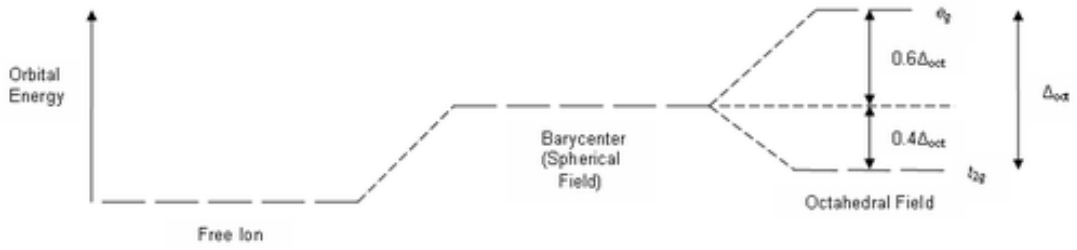

Figure. 1.6. Octahedral crystal field stabilization energy

If the splitting of the *d*-orbitals in an octahedral field is Δ_{oct}, the three t_{2g} orbitals are stabilized relative to the barycenter by $(2/5)\Delta_{oct}$, and the e_g orbitals are destabilized by $(3/5)\Delta_{oct}$. As examples, one can consider the two d^5 configurations shown previously. The low-spin example has five electrons in the t_{2g} orbitals, so the total CFSE is $5x2/5\Delta_{oct}=2\Delta_{oct}$. In the high-spin example, the CFSE is $(3x2/5\Delta_{oct})-(2x3/5\Delta_{oct})=0$. Thus, the stabilization generated by the

electrons in the lower orbitals is canceled out by the destabilizing effect of the electrons in the upper orbitals.

Crystal Field stabilization is applicable to transition-metal complexes of all geometries. Indeed, many d^8 complexes show square-planar structure due to the very large amount of crystal field stabilization that this geometry produces with this number of electrons.

1.4.5. Ferroelectricity

A (proper) ferroelectric possesses a spontaneous polarization of the electric dipoles, which may be switched by the application of an electric field. The polarization is due to a lack of inversion symmetry within the crystal structure. Indeed by considering the classic perovskite ABO_3 in which a central positive B-ion (a transition metal element) is surrounded by an octahedron of negatively charged oxygen ions (Fig. 1.7). A shift in the position of the B-site ion would break the inversion symmetry and cause the induction of a dipole moment. This in turn generates ferroelectric order as shown in Fig. 1.7.

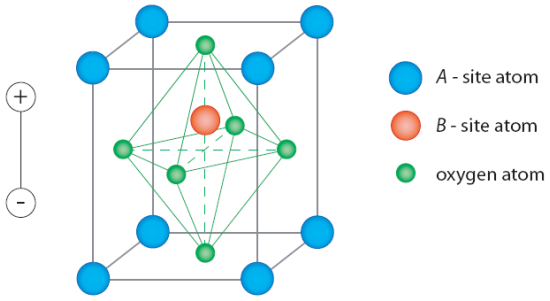

Figure. 1.7. Electric dipole moment generated by displacement of the B-site atom in the perovskite crystal structure.

The displacement of the B-site atom in the ABO_3 structure may occur during structural phase transitions in which the system moves from a high to low symmetry state (e.g. cubic to tetragonal). One of the best known examples of a proper ferroelectric is $BaTiO_3$ [30]. In most

of ferroelectric perovskites, the B-site atom has an empty *d*-electron shell which allows covalent bonding with the full *p* orbitals of the oxygen atoms. Ferroelectricity may also occur due to the existence of lone pairs of electrons on the outer shell of the A-site atom, which are highly susceptible to polarization. This is the cause of ferroelectricity in $BiFeO_3$. On the other hand, in an improper ferroelectric, the spontaneous polarization is provoked by a polar displacement of the ions which, nevertheless, occurs as a result of some other effect within the material. In a geometric ferroelectric, the dipole moment occurs due to non-polar lattice distortions, due to e.g. electrostatic forces rather than changes in chemical bonding. Examples of such materials are TMO and $YMnO_3$, where a ferroelectric state is due to a buckling of the rigid MnO_5 bipyramids [24]. In charge ordered ferroelectrics, the spontaneous polarization is dependent on electron correlations in the material [31]. Such charge ordered ferroelectricity is observed in $LuFe_2O_4$ [32]. Improper ferroelectricity may also occur due to magnetic order, which will be treated with more detail in the thesis itself.

1.4.6. Magnetism

Magnetic order in a material occurs due to the interactions between magnetic moments. The interactions between neighboring spins $\boldsymbol{S}_i$ and $\boldsymbol{S}_j$ are described by the Heisenberg model with the Hamiltonian given by $H=-\Sigma_{ij}\, J_{ij}\boldsymbol{S}_i\cdot\boldsymbol{S}_j$. Here, the value J_{ij} is the exchange constant, and describes the nature of the interaction between $\boldsymbol{S}_i$ and $\boldsymbol{S}_j$. If J_{ij} is positive, neighboring spins favor a parallel alignment, and the system is ferromagnetic. If J_{ij} is negative, neighboring spins favor an antiparallel alignment, and the system is antiferromagnetic. Antiferromagnetism may exist in many forms in which sublattices of moments arrange so as to cancel each other out giving no net magnetization in the absence of an applied magnetic field. If the sublattices are not equally opposed (such that a net magnetization is present), the

system is called ferrimagnetic. Antiferromagnetic order may be described as commensurate (i.e. the periodicity of the spins is linked to the crystal structure) or incommensurate. Examples of commensurate antiferromagnetic order are A-type and G-type order, as shown in Fig. 1.8. Examples of incommensurate antiferromagnetic order are sinusoidally modulated spin density waves, and cycloidal order in which the spins change orientation along the propagation direction inside a circular or ellipsoidal envelope.

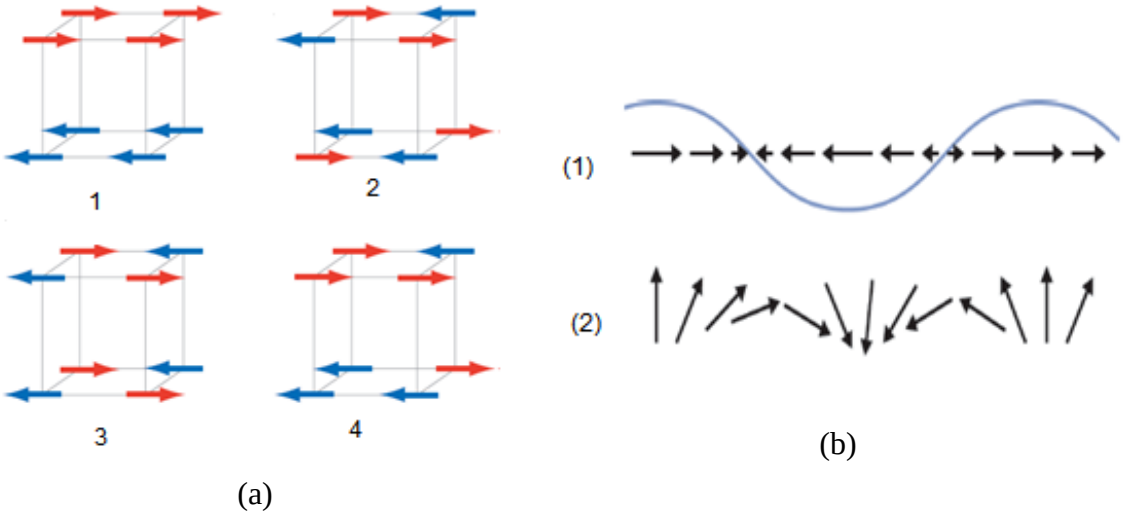

Figure. 1.8. (a). (1) A-type, (2) G-type, (3) C-type and (4) E-type commensurate antiferro magnetic order. (b). (1) sinusoidal and (2) cycloidal incommensurate antiferromagnetic order.

1.4.7. Crystalline Structure of parent $TbMnO_3$

The terbium manganite compound possesses an orthorhombic unit cell (space group Pbnm), as indicated in Fig. 1.9(c). The factor *t* (tolerance factor) for the parent compound amounts to 0.89, and the lattice parameters are a_0=5.293(1) Å, b_0=5.838(4) Å, and c_0=7.402(5) Å [33]. The lattice parameters reported for bulk/single crystal samples, particularly the *c*-lattice parameter, may vary significantly as consequence of different growth conditions and most likely different oxygen contents [34, 35]. A very important point concerning the crystalline structure of TMO has to do with the fact that the unit cell is rotated by 45° around the *c*-axis,

with respect to the primitive cubic cell. The unit cell is also doubled along the *c* axis and multiplied by √2 along the *a* and *b*-axis. The unit cell thus contains 4 formula units [Figure 1.9 (b)]. This is due to the distortion and tilt of the oxygen octahedra (antiphase rotation of the oxygen octahedra along the *a* and *b* axes of the pseudo cubic unit cell and the in-phase rotation along the *c* axis of the pseudocubic unit cell), which is known as $GdFeO_3$ distortions [36]. This type of distortion is associated with orthorhombic lattice parameters that follow the relationship $c_0/\sqrt{2} > a_0$ and $a_0 < b_0$. In case of TMO, the lattice parameters have a different relationship ($c_0/\sqrt{2} < a_0$), indicating that the Pbnm structure of TMO presents another distortion superimposed on the $GdFeO_3$-like rotations. Certainly, the manganese ions in the structure are in an octahedral coordination and possess a valence of 3+. In the high spin state (S=2), three electrons occupy the t_{2g} orbitals and one electron occupies the doubly degenerate e_g orbitals. This implies that the high spin state of manganese in TMO is Jahn-Teller active [37]. This is based on the fact that by the Jahn-Teller distortion, the energy of the molecule decreases and the degeneracy is lifted. Hence, wave functions that would have the same energy in the high-symmetric molecule now can have different energies. The lowest of these is non-degenerate and lies below the energy of the undistorted molecule. The manganese ions may also exist in a low spin state (S=1) with fourth electrons occupying the t_{2g} orbitals, leading to a weak Jahn-Teller effect in this spin state. In octahedral complexes, the Jahn-Teller effect is most pronounced when an odd number of electrons occupy the e_g orbitals. This situation arises in complexes with the configurations d^9, low-spin d^7 or high-spin d^4 complexes, all of which have doubly degenerate ground states. This is because the e_g orbitals point directly at the coordinating oxygen atoms. The effect also occurs for a strong degeneracy of electrons in the t_{2g} orbitals. However, the effect is much less noticeable than when e_g orbitals are involved. This is because the t_{2g} orbitals do not point directly in direction

of the coordinating oxygens implying that here there is a much smaller lowering of repulsion on taking ligands further away from the t_{2g} orbitals. The same is true for tetrahedral complexes (e.g. manganate. Here, distortion is very subtle because the ligands are not pointing directly to the orbitals).

As stated above, the Jahn-Teller effect provokes the lifting of degeneracy of the e_g orbitals stabilizing the d_z^2 or $d_{x^2-y^2}$ orbitals depending on if the Jahn-Teller distortion compresses or expands one of the directions of the oxygen octahedra (Q_3 mode). Certainly, the compression in the (ab)-plane stabilizes the d_z^2 orbital whereas expansion stabilizes the $d_{x^2-y^2}$ orbital (Fig. 1.10). The Jahn-Teller distortion can also produce an effect of orthorhombic distortion of the oxygen octahedra (Q_2 mode), stabilizing the superposition of the d_z^2 and $d_{x^2-y^2}$ orbitals [Fig. 1.10 (c)]. Particularly, in case of TMO, the longest Mn-O bond is on the (ab) plane, whereas the shortest Mn-O bond is along the out-of-plane direction [Fig. 1.11(a)]. This means that the $d_{3x^2-r^2}$ and $d_{3y^2-r^2}$ orbitals are stabilized in TMO as shown in figure 1.11 (a). Finally, a cooperative Jahn-Teller distortion in a thin film under epitaxial strain might influence the cation-ligand-cation superexchange interactions. This issue is going to be discussed in the next section.

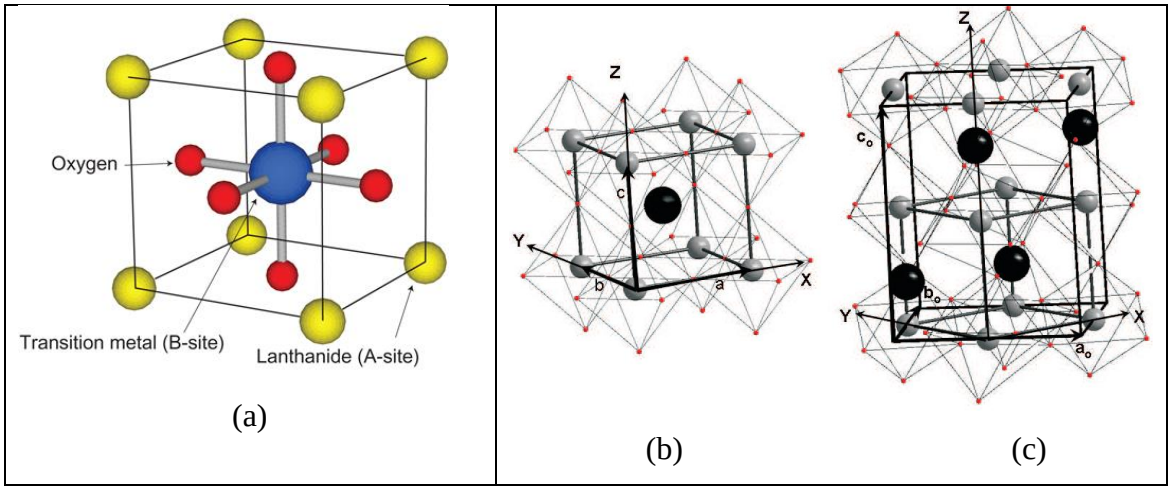

Figure 1.9. (a) Basic ABO_3 crystal structure. (b) ABO_3 structure in its cubic form showing the oxygen atoms in octahedral configuration. (c) Crystal structure of TMO in its room temperature orthorhombic symmetry as indicated by black contour. The pseudo cubic unit cell is drawn inside the orthorhombic unit cell as grey contour [6].

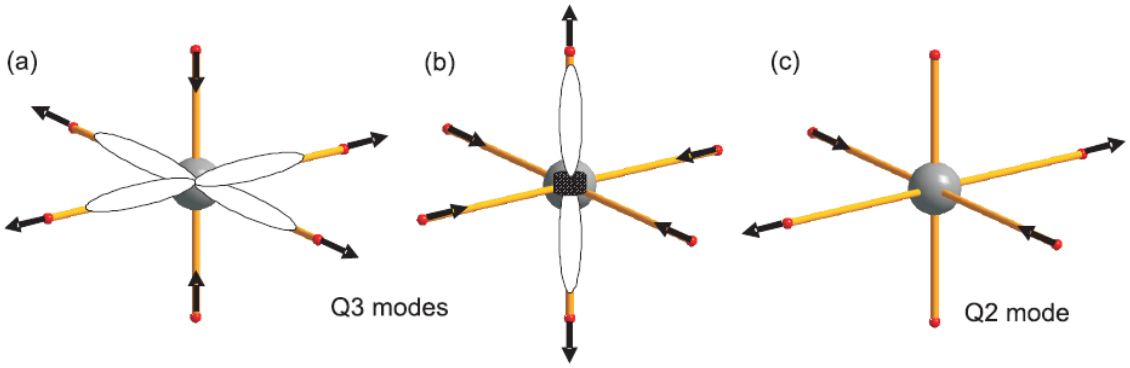

Figure 1.10. (a), (b) Two types of Q_3 mode of Jahn-Teller distortion stabilizing the $d_{x^2-y^2}$ and d_{z^2} orbitals. (c) Q_2 mode of the Jahn-Teller distortion favouring a superposition of $d_{x^2-y^2}$ and d_{z^2}.

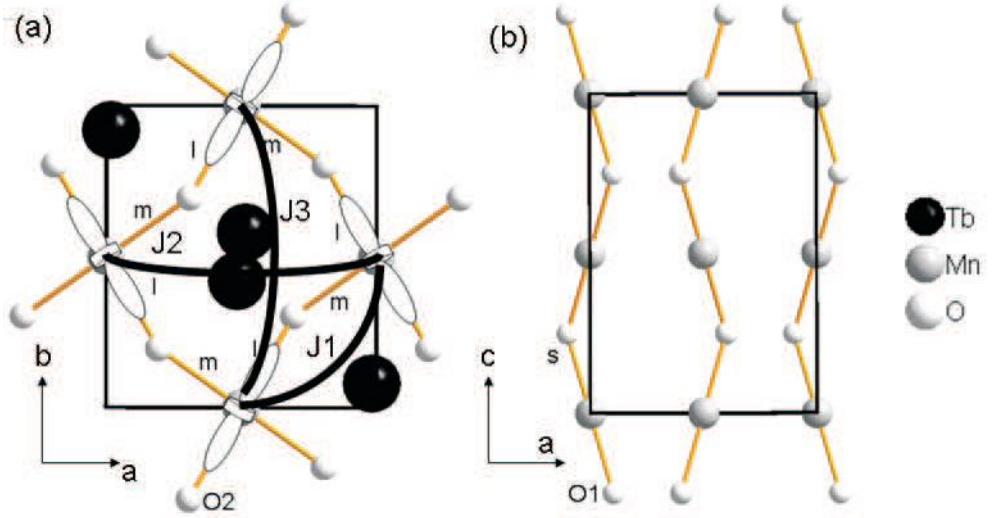

Figure 1.11. (a) Representation of the structure of TMO in the (ab) plane. The alternating medium and long bond length are indicated as *m* and *l*, respectively. The stabilized $d_{3x^2-r^2}$ and $d_{3y^2-r^2}$ are represented by their classical shape. The nearest neighbour superexchange (J1), next nearest neighbour along *a* (J2), and next nearest neighbour along *b* (J3) interactions are shown in the picture. (b) Representation of the structure of TMO in the (ac) plane. The short bond length is indicated as *s* in the picture. This representation emphasizes the tilting of the oxygen octahedra along the *c*-axis of the structure.

1.4.8. Magnetic interactions

1.4.8.1. Superexchange interactions

Long range magnetic order occurs due to the exchange interaction between magnetic moments. Direct exchange refers to the interaction between neighboring moments, but if the process occurs via some intermediate process it is termed indirect exchange or superexchange. A typical example would be a system with two magnetic atoms, each with a single *d*-orbital electron, separated by an oxygen atom. In an ionically bonded system, the oxygen ion will have two electrons in its *p*-orbital which will overlap with the *d*-orbitals of the magnetic atoms (Fig. 1.12).

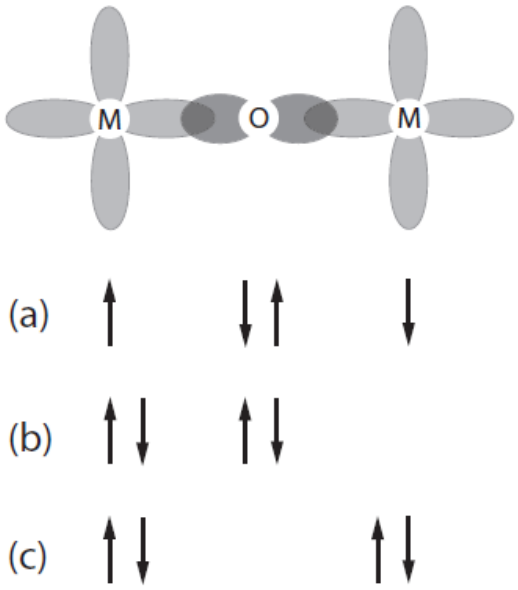

Figure 1.12. Two magnetic atoms, *M*, separated by an oxygen atom, O. (a) Antiferromagnetic alignment of the magnetic atoms is favored due to superexchange since this gives the electrons on the oxygen atom freedom to move as shown in (b) and (c) [38].

The energy of the system is lowered if the magnetic atoms order antiferromagnetically, since the electrons are then free to move from the oxygen ion to either magnetic ion. Conversely, if the magnetic ions order ferromagnetically, the oxygen electrons will not be able to move due to the Pauli' exclusion principle.

Superexchange dominates the magnetic interactions in TMO. Here, superexchange magnetic coupling occurs between two ions (Mn^{3+}) through a nonmagnetic intermediate anion (O^{2-}). Nevertheless, in crystals like MnO, the Mn atoms interact magnetically despite having a nonmagnetic oxygen ion between them [39]. Anderson later refined the superexchange model (Kramers' model) [40]. The main features of the superexchange interactions are usually summarized by the so-called Goodenough-Kanamori-Anderson (GKA) rules. According to these rules, the 180° superexchange between two magnetic ions, in which the magnetic ion-ligand-magnetic ion angle is closest to 180°, is strongly antiferromagnetic. The 90° superexchange (magnetic ion-ligand-magnetic ion angle close to 90°) interaction is weakly ferromagnetic. Moreover, the 180° superexchange is maximum for an angle of 180° allowing maximum overlap of the relevant orbitals. The 180° superexchange becomes weaker as the angle decreases [41]. The GKA rules are valid for transition metals that are not Jahn-Teller active. For Jahn-Teller distorted systems, the 180° superexchange rules are different. Superexchange adheres to the quantum mechanics requirement of an antisymmetric total wave function. In this regard, the cooperative Jahn-Teller effect is a phase transition, which is driven by the interaction between the electronic states of one of the constituent species of ions in a solid and the collective lattice vibrations or phonons. The phase transition may be of first or second order and in both these cases involves a symmetry-lowering distortion of the crystal lattice and a splitting of the electronic energy levels. For cooperatively Jahn-Teller distorted perovskites (the cooperative Jahn-Teller distortion of the octahedral leads to alternating short and long Mn-O distances in the plane *ac*), the antisymmetric wave function is imposed by the antiferromagnetic distorted structure. The latter is the result of the corner-sharing octahedra of the perovskite structure. Thus, the orbital part of the wave function imposes the antisymmetric symmetry and thus the magnetic

interaction is ferromagnetic in the *a*-*b* basal plane. For Pbnm symmetry perovskites, the interactions along the *c*-axis are antiferromagnetic. This is due to the mirror symmetry perpendicular to the *c*-axis, which results in the same orbital occupation along this axis.

1.4.8.2. Double-exchange interactions

For mixed valence compounds exists another interaction apart from superexchange. For instance, for Mn^{3+}-O-Mn^{4+} configuration, charge transport leads to stabilization of the ferromagnetic interactions. This mechanism operates for doped compounds and is known as double-exchange. Here, it involves the simultaneous charge transfer of an electron from Mn^{3+} to O^{2-} and another from O^{2-} to Mn^{4+}. For high enough doping, it may lead to a metallic ferromagnetic state as in $La_{1-x}Ca_xMnO_3$ for $0.2<x<0.5$.

1.4.8.3. Dzyaloshinskii-Moriya interaction

The Dzyaloshinskii-Moriya (DM) interaction is a process similar to superexchange, where the intermediate process is via spin-orbit interaction rather than an oxygen ion [42]. An exchange interaction occurs between the excited state of a magnetic ion and the ground state of the neighboring ion. For spins $\boldsymbol{S}_i$ and $\boldsymbol{S}_j$, a new term in the Hamiltonian is then given by $H=\boldsymbol{D}\cdot(\boldsymbol{S}_i\times\boldsymbol{S}_j)$. The DM vector $\boldsymbol{D}$ is finite when the crystal field does not have inversion symmetry with respect to the centre between $\boldsymbol{S}_i$ and $\boldsymbol{S}_j$. The effect of the DM interaction is often to provide a small canting of the moments in an antiferromagnetic structure, resulting in weak ferromagnetism. The DM interaction favors non-collinear spin ordering, which has important implications for multiferroic properties.

1.4.9. Complexity of $TbMnO_3$

In perovskite-type manganites, the doping of the A-site with divalent alkaline elements can give rise to different magnetic structures. In particular, if the doping elements are not magnetic, e.g. Al, the changes in the phsysicochemical properties of the parent compound, in bulk form, can be adscribed to chemical pressure. The magnetic structure of bulk TMO is complex due to the competition between ferromagnetic and antiferromagnetic interactions, leading to frustration and incommensurability of the spin structure [6]. This competition arises as the Mn-O-Mn bond angle gives rise to intermediate interactions between antiferromagnetic 180° superexchange and ferromagnetic 90° superexchange [41]. This fact facilities the study of the epitaxial strain in the material. Figure 1.14 shown that TMO lies in between two different magnetic structures. For Mn-O-Mn bond angles higher than 146°, an A-type antiferromagnetic structure is found, as in $LaMnO_3$ [43]. For bond angles lower than 144°, an E-type antiferromagnetic structure is found, as in the case of $HoMnO_3$ [44].

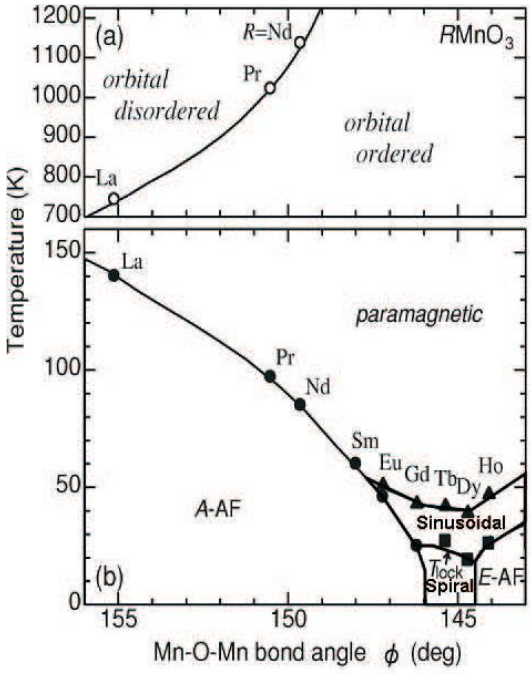

Figure 1.14. Magnetic phase diagram for orthorhombic rare earth manganites showing temperature as a function of the Mn-O-Mn bond angle [45]. The TMO manganite lies in an intermediate region between the A-type and E-type antiferromagnetic magnetic structures. The upper plot indicates that all the rare earth manganites (from La to Ho) are orbitally ordered at room temperature.

Orbital-ordering gives rise to the anisotropy of the electron-transfer interaction. This favors, or disfavors, the double-exchange interaction or superexchange interaction in an orbital direction-dependent manner and hence gives rise to a complex spin-orbital coupled state. The orbital-ordering is coupled with Jahn-teller distortion (Fig. 1.15).

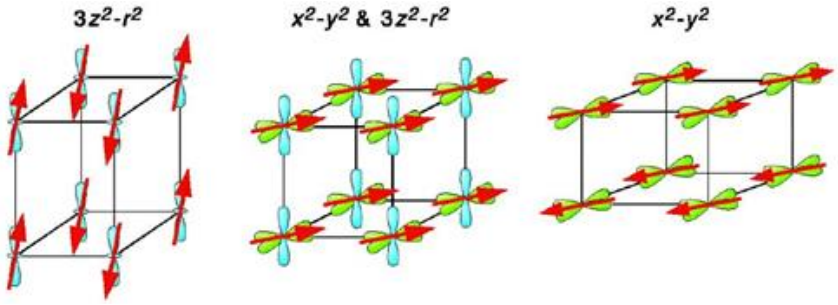

Figure 1.15. Different types of orbital ordering occurring in manganese-oxides perovskites.

As observed in Fig. 1.14 (upper panel), the rare earth manganites $RMnO_3$ (from La to Ho) are all orbitally ordered at room temperature. This is traced to the Jahn-Teller active Mn^{3+} ion with an increasing ordering temperature as the ionic radius decreases [46]. The orbital ordering temperature for TMO is about 1500 K [46].

The magnetic structure of TMO has been exhaustively studied by several groups [45,47]. The structure displays an incommensurate antiferromagnetic sinusoidal spin ordering below 40 K. A transition to a non-collinear antiferromagnetic cycloid spin ordering along the *b*-direction follows below 27 K (Fig. 1.16).

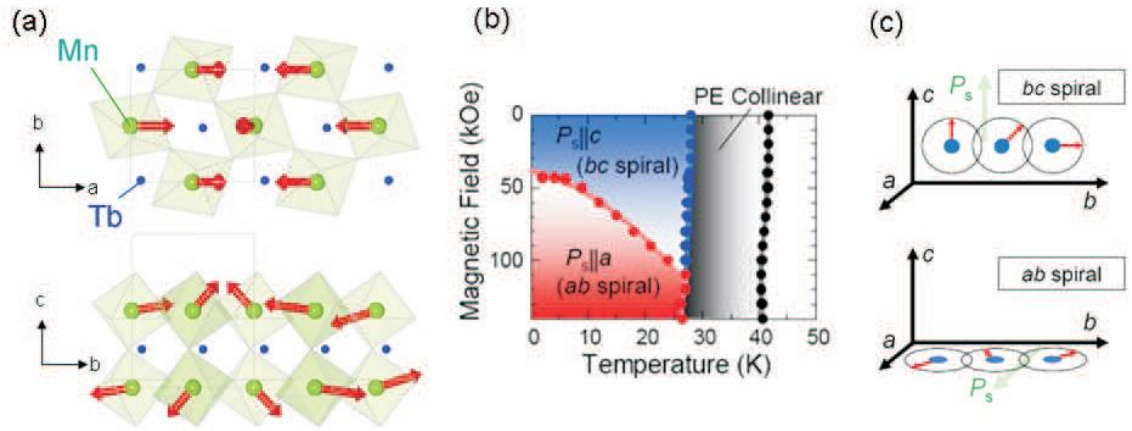

Figure 1.16. (a) Magnetic structure of TMO in the spin cycloid state. The spin cycloid is indicated by arrows and projected in the (*a*,*b*) plane (top panel) and (*b*,*c*) plane (bottom panel). (b) Applied magnetic field versus temperature phase diagram for TMO. (c) Schematic representation of the polarization flip transition under field [48].

In a phenomenological model, a way to generate the cycloidal phase is to consider that the ferromagnetic nearest neighbor (NN) superexchange is frustrated by a sufficiently strong antiferromagnetic next-nearest-neighbor (NNN) superexchange allowing for the observed incommensurability of the magnetic structure with respect to the lattice periodicity [25]. This is the so-called J1-J2-J3 model, using classical spins, where J1 is the NN superexchange, J2 and J3 are the NNN superexchange along the *a* and *b* directions, respectively, as shown in Fig. 1.11 [49]. Using Landau free energy, it has been shown that the cycloidal ordering breaks the inversion symmetry and allows for a polarization, perpendicular to both the wave vector ($\boldsymbol{q}$) and the spin rotation axis ($\boldsymbol{e}_3$) of the cycloid ($\boldsymbol{P} \propto \boldsymbol{e}_3 \times \boldsymbol{q}$) [34,50]. For TMO, the wave vector is along the *b*-axis and the spin rotation is around the *a*-axis, as depicted in Fig. 1.17. Therefore, the experimentally observed polarization along the *c*-direction confirms the theory. Microscopically, two possible mechanisms have been used to explain the appearance of the ferroelectric polarization at the cycloidal ordering: (a) an electronic contribution due to spin-orbit coupling [51, 52] and (b) a cation displacement due to the inverse

Dzyaloshinskii-Moriya interaction [$P \propto \boldsymbol{D}.(\boldsymbol{S}_i \times \boldsymbol{S}_j)$] [53, 54]. However, it has recently been theoretically shown that the inverse effect of the Dzyaloshinskii- Moriya interaction [55, 56] and its related atomic displacement, is the mechanism that explains the emergence of a net ferroelectric polarization in TMO [57, 58]. Indeed, the cycloidal arrangement of the spins induces an orientation of the local electric polarizations along the same direction, due to the inverse Dzyaloshinskii-Moriya interaction, and allows for a net macroscopic polarization as shown in Fig. 1.17 (a) for the case of a clockwise cycloid.

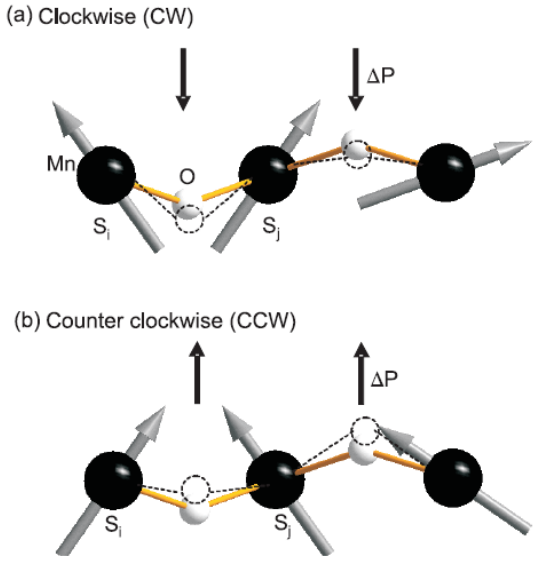

Figure 1.17. Schematic drawing of the local polarization in a clockwise cycloid (a) and in a counter-clockwise cycloid (b). The related local electric polarizations are shown as black arrows, the spins as grey arrows, and the manganese and oxygen atoms as black and white spheres, respectively. The shifts of oxygen atoms, due to the spin canting of neighbouring atoms, are indicated as dashed lines [6,59].

On the other hand, it is also expected, that due to the asymmetric DM interaction [$(\boldsymbol{S}_i \times \boldsymbol{S}_j) = -(\boldsymbol{S}_j \times \boldsymbol{S}_i)$], the polarization may be switched by time reversal of the cycloid, as shown in Fig. 1.17 (b) for a counter-clockwise cycloid. In the case of a cycloidal ordering, a strong coupling may be expected between the electric and magnetic orders, as they are associated with a single mechanism. Even though cycloidal spin structures and related polarizations usually

appear at low temperatures, such systems are of special fundamental interest because of this large coupling between the magnetic and electric orders, and the fundamental challenges they pose. Indeed, it has been shown for TMO that a field of around 5 T along the *a*-direction flips the spin rotation axis and simultaneously the polarization from the *c*-axis to the *a*-axis [47, 60], as shown in the phase diagram plotted in Fig. 1.14.

1.5 Growth modes of thin films

The occurrence of the epitaxial growth modes depends on various parameters of which the most important are the thermodynamic driving force and the misfit between substrate and layer. The growth mode characterizes the nucleation and growth process. There is a direct correspondence between the growth mode and the film morphology, which gives the structural properties such as flatness and interface abruptness of the layers. The growth mode is determined by the kinetics of the transport and diffusion processes on the surface. Different atomistic processes may occur on the surface during film growth, namely deposition, diffusion on terraces, nucleation on islands, nucleation on second-layer island, diffusion to a lower terrace, attachment to an island, diffusion along a step edge, detachment from an island, or diffusion of dimmer (see figure 1.18).

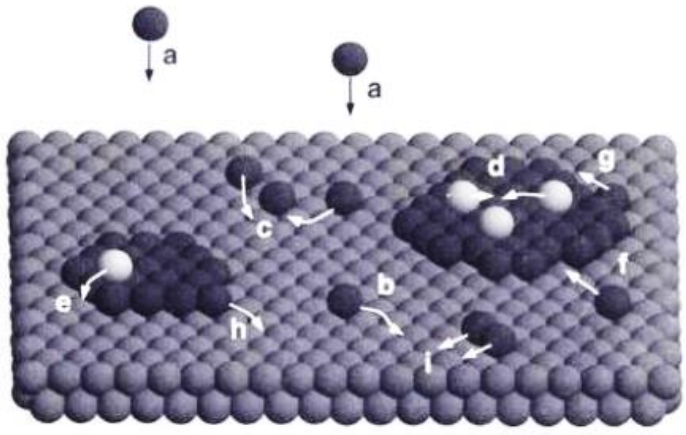

Figure 1.18: Atomistic processes during the growth: a) deposition, b) diffusion on terraces, c) nucleation on islands, d) nucleation on second-layer island, e) diffusion to a lower terrace, f) attachment to an island, g) diffusion along a step edge, h) detachment from an island, i) diffusion of dimmer.

Usually growth modes are classified into three categories, namely, the layer-by-layer or Frank-van der Merwe, the island or Volmer-Weber, and the layer-plus-island or Stranski-Krastanow growth mode (see figure 1.19) [61]. In addition to the three well-known epitaxial growth modes mentioned above there are four distinct growth modes labeled as: step flow mode, columnar growth, step bunching, and screw-island growth [62].

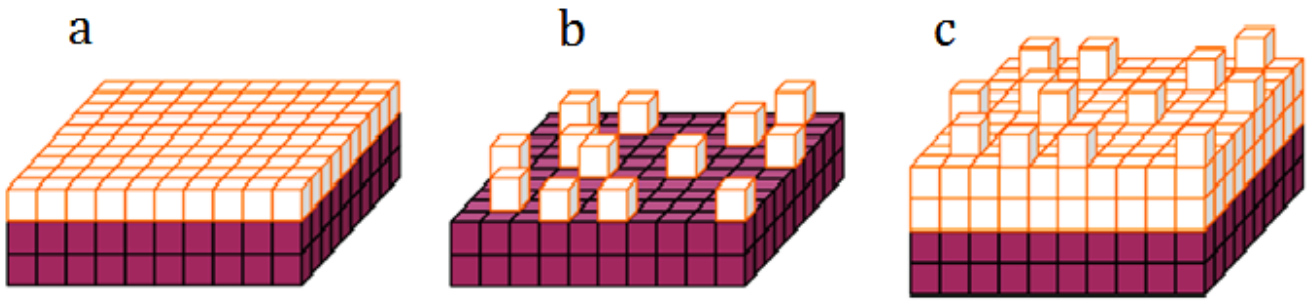

Figure 1.19: Schematic presentation of the (a) Frank-van der Merwe mode (2D growth mode), (b) Volmer-Weber mode (island growth mode), and (c) Stranski-Krastanow growth mode.

During Frank-van der Merwe or layer-by-layer growth mode a new layer is nucleated only after completion of the layer below. This growth occurs over long distances in ideal case. However crystals are not perfect and contain defects like dislocation that acts as a 'sink' for growth species. Normally there are continues step sources like screw dislocations or other defects, so Frank-van der Merwe growth mode works continuously and it can spread growth steps over macroscopic distances. The optimum layer homogeneity can be achieved by one dimensional movement of steps in Frank-van der Merwe mode initiated by a precisely controlled small angle substrate misorientation. In lattice-matched systems, the growth mode is determined by the relation between the energies of two surfaces and the interface energy.

If the sum of the surface energy (γ_f) of the epitaxial layer and the energy of the interface (γ_i) is lower than the substrate surface energy (γ_s), i.e. $\gamma_f + \gamma_i < \gamma_s$, upon deposition, the top material will cover the substrate, leading to the Frank-van der Merwe growth mode (Fig. 1.19(a)). In other words, in a layer-by-layer growth mode, the deposited atoms are more strongly attracted to the substrate than they are to one another. Most epitaxial techniques take advantage of the Frank-van der Merwe growth mode. Changing the value of $\gamma_f+\gamma_i$ may result in a transition from this growth mode to the Volmer-Weber growth mode where 3D islands are formed (Fig. 1.19(b)). In this growth mode, the deposited atoms are more strongly bound to each other than they are to the substrate. A Volmer-Weber growth mode consists in first phase of a large number of surface nuclei and in second phase of their spreading. Thus, Volmer-Weber growth often results in a high mosaicity of the material inside the layer. Usually, continues growth of the layer, after initial Volmer-Weber growth, occurs by columnar growth. A typical example of Volmer-Weber growth mode is when a metal is deposited on top of a semiconductor. In a lattice-mismatched material system, such as GaAs/InAs heterostructures with 7 % lattice mismatch, only the first few deposited monolayers form strained epitaxial layers with the lateral lattice constant equal to that of the substrate. When a critical thickness is exceeded, the significant strain occurring in the top layers leads to the spontaneous formation of randomly distributed islands which contribute to relax the elastic energy stored in the system. The phase transition from the two-dimensional epitaxial structure to the random arrangement of three-dimensional islands is called the Stranski-Krastanow transition [Fig. 1.19(c)]. Hence, Stranski-Krastanow mode is considered as intermediate between the Frank-van der Merwe and Volmer-Weber growth modes, and it is caused by significant lattice misfit between film and substrate. The lattice mismatch between the substrate and the

film creates a build-in strain as a consequence of the increasing elastic energy with increasing layer thickness. The first deposited layer is atomically smooth (Frank-van der Merwe growth mode) and compressively strained up to a certain thickness called critical thickness. When the film exceeds the critical thickness, a phase transition to islands rapidly takes place (Volmer-Weber growth mode) because the non-uniform strain field can reduce the strain energy by an island array, compared with a uniform flat film, resulting in the Stranski-Krastanow growth mechanism. As to the other growth modes, it should be pointed out that step flow growth mode [fig. 1.20 (a)] is clearly distinct from layer-by layer growth in Frank-van der Merwe mode. Unidirectional step flow is induced by substrate missorientation (off-cut angle). This trick is often used to avoid island formation, their coalescence and following columnar growth in epitaxy from the vapor phase. Step bunching is observed when a high density of steps moves with large step velocities over the growth surface (fig. 1.20 (b)). By fluctuations, higher steps catch up with lower steps and then move together as double, triple or in general as macro steps that can exceed thickness of thousands of monosteps. The microsteps cause different incorporation rates of impurities and dopands due to locally varying growth rate. Coalescence of larger number of initial growth islands may lead to screw dislocations due to the layered structure resulting in spiral-island growth mode (Fig. 1.20 (c)).

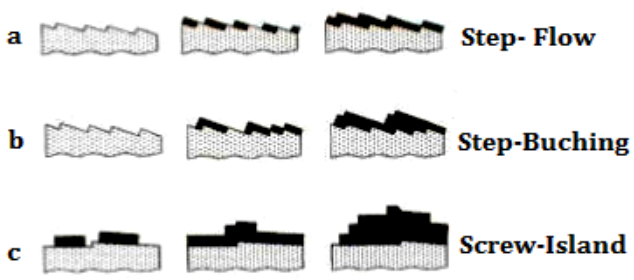

Figure 1.20: additional growth modes of thin films.

References

[1] Schmid H 1994 Multi-ferroic magnetoelectrics *Ferroelectrics* **162** 317.

[2] Schmid H 1973 On a magnetoelectric classification of materials *Int. J. Magn.* **4** 337.

[3] I. Dzyaloshinskii and L. Pitaevskii, Soviet Phys.- JETP **9**, 1281 (1959).

[4] D. N. Astrov, Soviet Phys.- JETP **11**, 708 (1960).

[5] W. Eerenstein, N. Mathur, and J.F. Scott, Nature **442**, 759 (2006).

[6] Christophe Daumont, Ph.D thesis, University of Groningen (Netherlands), 2009.

[7] R. Ramesh and N. A. Spaldin, Nature Mater. **6**, 21 (2007).

[8] T. Kimura, G. Lawes, T. Goto, T. Tokura, and A. P. Ramirez, Phys. Rev. B **71**, 224425 (2005).

[9] D. Khomskii, Phys. **2**, 20 (2009).

[10] R. Kajimoto, H. Yoshizawa, H. Shintani, T. Kimura, and Y. Tokura, Phys. Rev. B **70**, 012401 (2004).

[11] T. S. Chan, R. S. Liu, Y. H. Lien, C. Y. Huang, and J. G. Lin, Chin. J. Phys. (Taipei) 43(3-II), **757** (2005).

[12] L.W. Martin, S. P. Crane, Y.-H. Chu,M. B. Holcomb,M. Gajek,M. Huijben, C.-H. Yang, N. Balke, and R. Ramesh, J. Phys.: Condens.Mat. **20**, 434220 (2008).

[13] W. Prellier,M. Singh, and P.Murugavel, J. Phys.: Condens.Mat. **17**, R803 (205).35.

[14] S. A. Wolf, D. D. Awschalom, R. A. Buhrman, J. M. Daughton, S. von Molnár, M. L. Roukes, A. Y. Chtchelkanova, and D. M. Treger, *Science* **294**, 1488 (2001). 1-4.

[15] M. E. Lines and A. Glass, *Principle and Application of Ferroelectric and Related Materials* (Oxford University Press, Oxford, 2001).

[16] J. F. Scott, *Ferroelectric Memories* (Springer-Verlag, Berlin, 2000).

[17] N. A. Hill, Journal of Physical Chemistry B **104**, 6694 (2000).

[18] Silvia Picozzi and Claude Ederer, J. Phys.: Condens. Matter **21** (2009) 303201.

[19] Fennie C J and Rabe K M 2005 Ferroelectric transition in $YMnO_3$ from first principles *Phys. Rev.* B **72** 100103(R).

[20] G. A. Smolenskii, A. I. Agranovskaia, S. N. Popov, and V. A. Isopov, Sov. Phys. Tech. **3**, (1981-1982).

[21] Y. Yang, J. Liu, H. Huang,W. Q. Zou, P. Bao, and Z. G. Liu, Phys. Rev. B **70**, 132101 (2004).

[22] P. Baettig, R. Seshadri, and N. Spaldin, J. American Chem. Soc. **129**, 9854 (2007).

[23] R. Seshadri and N. A. Hill, Chem.Mater. **13**, 2892 (2001).

[24] B. V. Aken, T. Palstra, A. Filippetti, and N. Spaldin, Nature Materials **3**, 164 (2004).

[25] S.-W. Cheong and M.Mostovoy, Nature Materials **6**, 23 (2007).

[26] M. Mostovoy, Phys. Rev. Lett. **96**, 067601 (2006).

[27] Ederer, C. Novel materials for the future. interconnect, **4**, (2010).

[28] Van Vleck, J. *Physical Review* **41** (1932) 208.

[29] Miessler, Gary L.; Donald A. Tarr (1998). *Inorganic Chemistry (2nd edition)* Upper

[30] Merz, W. J. Physical Review **76** (1949) 1221.

[31] Portengen, T., ¨Ostreich, T., and Sham, L. J. Physical Review B **54**, 17452 (1996).

[32] Ikeda, N., Ohsumi, H., Ohwada, K., Ishii, K., Inami, T., Kakurai, K., Murakami, Y., Yoshii, K., Mori, S., Horibe, Y., and Kito, H. Nature **436**, 1136 (2005).

[33] J. A. Alonso, M. Martinez-Lope, M. Casais, and M. Fernandez-Diaz, Inorganic Chemistry **39**, 917 (2000).

[34] M. Kenzelmann, A. B.Harris, S. Jonas, C. Broholm, J. Schefer, S. B. Kim, C. L. Zhang, S.-W. Cheong, O. P. Vajk, and J.W. Lynn, Phys. Rev. Lett. **95**, 087206 (2005).

[35] N. Aliouane, D. N. Argyriou, J. Strempfer, I. Zegkinoglou, S. Landsgesell, and M. V. Zimmermann, Phys. Rev. B **73**, 020102 (2006).

[36] A. Maignan, C. Martin, G. Van-Tendeloo, M. Hervieu, and B. Raveau, Phys. Rev. B **60**, 15214 (1999).

[37] H. Jahn and E. Teller, Proceedings of the Royal Society of London. Series A, Mathematical and Physical Sciences **161**, 220 (1934-1990).

[38] Blundell, S. Magnetism in Condensed Matter. Oxford University Press, (2001).

[39] H. A. Kramers, Physica **1** 182 (1934).

[40] P.W. Anderson, Phys. Rev. **350** (1950).

[41] J. Goodenough, in *Magnetism and chemical bonds*, edited by J. Wiley and Sons (Interscience publishers, New York, 1963).

[42] Daniel Thomas O'Flynn, Ph.D thesis, University of Warwick (England), 2010.

[43] G. Matsumoto, Journal of the Physical Society of Japan **29**, 606 (1970).

[44] A. Muñoz, M. Casáis, J. A. Alonso, M. J. Martínez-Lope, J. Martínez, and M. Fernández-Diaz, Inorganic Chemistry **40**, 1020 (2001).

[45] T. Goto, T. Kimura, G. Lawes, A. P. Ramirez, and Y. Tokura, Phys. Rev. Lett. **92**, 257201 (2004).

[46] G. Maris, Ph.D. thesis, PhD Thesis, Rijskuniversiteit Groningen, 2004.

[47] T. Kimura, T. Goto, H. Shintani, K. Ishizaka, T. Arima, and Y. Tokura, Nature **426**, 55 (2003).

[48] Y. Yamasaki, H. Sagayama, N. Abe, T. Arima, K. Sasai, M. Matsuura, K. Hirota, D. Okuyama, Y. Noda, and Y. Tokura, Phys. Rev. Lett. **101**, 097204 (2008).

[49] T. Kimura, S. Ishihara, H. Shintani, T. Arima, K. Takahashi, K. Ishizaka, and Y. Tokura, Phys. Rev. B **68**, 060403 (2003).

[50] J. L. Ribeiro, Phys. Rev. B **76**, 144417 (2007).

[51] H. Katsura, N. Nagaosa, and A. Balatsky, Phys. Rev. Lett. **95**, 057205 (2005).

[52] C. Jia, S. Omoda, N. Nagaosa, and J. Han, Phys. Rev. B **74**, 224444 (2006).

[53] I. A. Sergienko and E. Dagotto, Phys. Rev. B **73**, 094434 (2006).

[54] Q. C. Li, S. Dong, and J.-M. Liu, Phys. Rev. B **77**, 054442 (2008).

[55] I. E. Dzyaloshinskii, Soviet Phys.- JETP **19**, 960 (1964).

[56] T. Moriya, Phys. Rev. **120**, 91 (1960).

[57] C. Jia, S. Onoda, N. Nagaosa, and J. H. Han, Phys. Rev. B **76**, 144424 (2007).

[58] H. J. Xiang, S.-H. Wei, M.-H. Whangbo, and J. L. F. D. Silva, Phys. Rev. Lett. **101**, 037209 (2008).

[59] T. Kimura, Annu. Rev. Matter. Res. **37**, 387 (2007).

[60] N. Abe, K. Taniguchi, S. Ohtani, T. Takenobu, Y. Iwasa, and T. Arima, Phys. Rev. Lett. **99**, 227206 (2007).

[61] T. Fukuda, H.J. Scheel, Crystal Growth Technology. Wiley, New York (2003).

[62] C.J. Brinker, S.W. Scherer, Sol–Gel science: the physics and chemistry of sol–gel processing. Academic Press, New York (1990).

Chapter 2

Experimental methods

For the current Ph.D. thesis, high-quality TMO bulk samples and thin films were prepared in the laboratorio para materiales cerámicos y vítreos at the Universidad Nacional de Colombia, Campus Medellín, and laboratorio para bajas temperatures at the Universidad del Cauca, in Popayán, Colombia. In this chapter, technical aspects of the performed experiments as well as the analytical tools employed to the structural, morphological, electrical, dielectric and magnetic characterization of TMO samples, both in bulk and thin film form, are briefly discussed.

2.1 Synthesis of polycrystalline TMO samples

Polycrystalline samples of the $Tb_{1-x}Al_xMnO_3$ system (x=0, 0.05, 0.07, 0.1, 0.2, 0.3), $TbMn_{1-x}Al_xO_3$ system (x =0.05, and 0.1) were fabricated by means of standard solid-state reaction. This ceramic method is the simplest and most common way of preparing among others complex novel oxides. The process consists in heating together stoichiometric amounts of nonvolatile solids, which react to form the required product. For preparing TMO samples, stoichiometric amounts of Tb_4O_7, MnO_2, and Al_2O_3 powders with high purity, 99,998 %, 99,997 % and 99 %, respectively, were mixed and grounded in an agate mortar for about 1 h approximately. Polyvinyl alcohol (1% of the weight of the mixture) was added in order to facilitate the grinding. The homogeneous mixtures, with different concentrations, were palletized (1.3 cm in diameter and 2 mm thickness) using a cylindrical press at a pressure of 6 Ton. The pellets were preheated at 800 ºC for eight hours, and then sintered at 1200 ºC for 12 hours in air atmosphere.

2.2 Target preparation

The targets $Tb_{1-x}Al_xMnO_3$ (x=0, 0.05, 0.1, 0.3) and $TbMn_{1-x}Al_xO_3$ (x =0.05, and 0.1), were prepared by single-phase powder obtained by the method mentioned above. The powders were pressed in the form of pellets (~3.5 cm in diameter and thickness ~3 mm) using pressures as high as 7000 psi, the resulting pellets were slowly heated in air (~3 °C/min) up to 1200 °C and then sintered for 20 h. Once the procedure is completed sintering furnace was allowed to cool to room temperature, the targets was glued to a cooper holder using silver epoxy resin and the set was coupled to a sputter cannon (see Fig. 2.1). The targets were pre-sputtered by about 48 h before film deposition in order to remove possible contaminated surface layers formed during the sintering process.

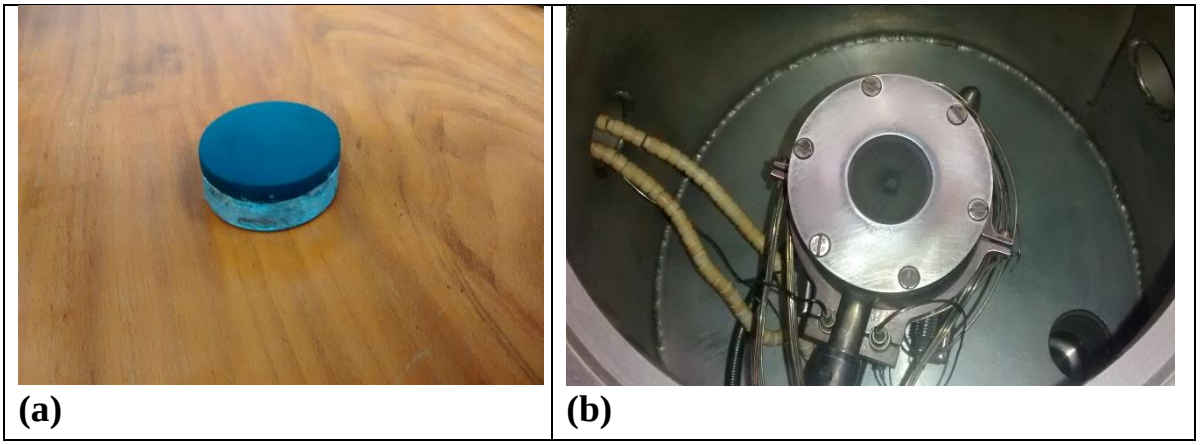

Figure 2.1: (a) TMO target mounted on a cooper holder. (b) TMO target coupled to a sputtering canon.

2.3. Thin films growth

2.3.1. Magnetron sputtering technique

In the basic sputtering process, a target (or cathode) plate is bombarded by energetic ions generated in a glow discharge plasma, situated in front of the target. The bombardment process causes the removal, i.e., sputtering, of target atoms, which may then condense on a

substrate as a thin film [1]. Physical sputtering is then driven by momentum exchange between the ions and atoms in the materials, due to collisions. Secondary electrons are also emitted from the target surface as a result of the ion bombardment, and these electrons play an important role in maintaining the plasma. The basic sputtering process has been known for many years and many materials have been successfully deposited using this technique [2]. However, the process is limited by low deposition rates, low ionization efficiencies in the plasma, and high substrate heating effects. These limitations have been overcome by the development of magnetron sputtering. Magnetrons make use of the fact that a magnetic field configured parallel to the target surface can constrain secondary electron motion to the vicinity of the target. The magnets are arranged in such a way that one pole is positioned at the central axis of the target and the second pole is formed by a ring of magnets around the outer edge of the target. Trapping the electrons in this way substantially increases the probability of an ionizing electron-atom collision occurs. The increased ionization efficiency of a magnetron results in a dense plasma in the target region. This, in turn, leads to increased ion bombardment of the target, giving higher sputtering rates and, therefore, higher deposition rates at the substrate. In addition, the increased ionization efficiency achieved in the magnetron mode allows the discharge to be maintained at lower operating pressures (typically, 10^{-3} mbar, compared to 10^{-2} mbar) and lower operating voltages (typically 500 V, compared to 2 to 3 kV) than is possible in the basic sputtering mode. In a conventional magnetron, the plasma is strongly confined to the target region. A region of dense plasma typically extends some 60 mm from the target surface. Films grown on substrates positioned within this region will be subjected to concurrent ion bombardment, which can strongly influence the structure and properties of the growing film. The high energy of the bombarding ions can lead to defects in the growing film and increased film stress. This can be detrimental

to the overall film properties. Thus, it is difficult to deposit fully dense films on large or complex components using conventional magnetrons [3]. To deposit dense films without introducing excessive intrinsic stresses, a high flux (>2 mA/cm^2) of relatively low energy (<100 eV) ions is generally preferred [4]. These conditions are readily provided by raising the atmosphere pressure in the chamber to some mbars (high-pressure magnetron sputtering). In this way, it is possible that the ion current drawn at the substrate to be <1 mA/cm^2, which is generally insufficient to modify the structure of the film. For the deposition of the TMO films reported in the present thesis, a high-oxygen pressure magnetron sputtering machine was employed (see fig. 2.2).

(a) (b)

Figure 2.2. (a) High-oxygen pressure magnetron sputtering machine. (b) Photograph of plasma and target holder with the TMO target.

For the deposition of TMO thin films, commercially available (001)-oriented $SrTiO_3$ substrates (with size 5x5x0.5 mm^3) with the lattice parameters a=3.90 Å may offer reasonable conditions for a textured growth of TMO. Moreover, (001)-$SrTiO_3$ is preferred in studies of epitaxy in perovskites because it can be obtained with atomically flat surfaces, favoring high quality growth. Some films were also grown on MgO substrates (a=4.12 Å) in order to

generate a different grade of stress in the film. The TMO films discussed in the thesis were grown by *dc* and *rf* magnetron sputtering, using the system previously described in this chapter. In the case of the films grown by *rf* magnetron sputtering, a substrate temperature varied between 700° C and 750° C, Ar-pressure of $1x10^{-2}$ millibar and an *rf*-power of 60 W were chosen as deposition parameters. For films grown by *dc* magnetron sputtering, temperatures of 750, 780 and 800° C were tested as substrate temperature. The deposition at three different deposition temperatures is aimed to optimize this growing parameter. An oxygen pressure of 3 mbar (2250 mTorr) was established as the appropriate deposition temperature to get a stable and uniform plasma. The power was 30 W and the distance between the surface of the substrate and the surface of the target was kept at 4 cm. After deposition, the substrate temperature was lowered to 450 °C and the chamber was then flooded with oxygen at a pressure of ~800 mbar. The films were annealed under these conditions for 1 h. The thickness of the films was fixed to about 100 nm.

2.4. Characterization techniques

In this section, a description of the technical aspects of experimental techniques employed in this work will be briefly introduced. Experimental techniques embrace the analytical tools to characterize the structural, morphological, electrical, dielectric, thermal and magnetic properties of undoped and Al-doped TMO samples both in bulk and thin film form. The TMO system is increasingly recognized as a material of importance due to its rich physics and chemistry in their layered structure and potential technological applications. Therefore, a careful and detailed characterization of the material is necessary to gain a deep insight into the complex behavior of this novel oxide.

2.4.1. Structure and morphology

2.4.1.1. X-ray diffraction

The structural properties of undoped and Al-doped TMO manganites, both in bulk and thin film form, were studied by X-ray diffraction measurements using a Panalytical X'Pert Pro MPD diffractometer equipped with Cu Kα radiation [λ=0.154(1) nm] and a Bruker D8 Discover four-circle X-ray diffractometer using also Cu Kα radiation. The data were collected from 10-90° in step width of 0.013°. X-ray reciprocal space mapping studies were conducted on a representative TMO film using high-resolution X-ray diffractometry (HRXRD) in a four-circle diffractometer with monochromatic Cu Kα radiation.

An X-ray diffractometer mainly comprises three basic parts: an X-ray source, a sample holder and an X-ray detector. X-ray diffraction is an important tool used to identify phases by comparing the experimental data with data from known structures. The technique also allows one to determine the crystallographic structure (i.e. cell parameters, space group and atomic coordinates) of novel or unknown crystalline materials. Through this technique, it is equally possible to quantify changes in the cell parameters, orientation, crystallite size and other structural parameters. Generally speaking, the crystalline solids can be categorized as single crystal and polycrystalline solids. In single crystals, the regular periodic pattern of the atoms continues throughout the whole bulk of the solid without any interruption, whereas polycrystalline solids are composed of many grains which are randomly oriented and separated by grain boundaries. Crystal structure determination of the materials is important in the sense that their properties depend much upon the arrangement of the atoms and the strength of the bonds among them. The interaction of X-ray radiation with crystalline samples

is governed by Bragg's law, which depicts a relationship between the diffraction angles (Bragg angle), X-ray wavelength, and interplanar spacing of the crystal planes. According to Bragg's law, the X-ray diffraction can be visualized as X-rays reflecting from a series of crystallographic planes as shown figure 2.3. The path differences introduced between a pair of waves travelled through the neighboring crystallographic planes are determined by the interplanar spacing. If the total path difference is equal to nλ (n being an integer), the constructive interference will occur and a group of diffraction peaks can be observed, which give rise to X-ray patterns. The quantitative account of Bragg's law can be expressed as $2d_{hkl}Sen\theta = n\lambda$, where d is the interplanar spacing for a given set of ($hk\ell$) planes, and θ the Bragg angle [5]. For known values of λ and θ, the atomic spacing for a particular set of planes of a crystal can be determined from the last equation.

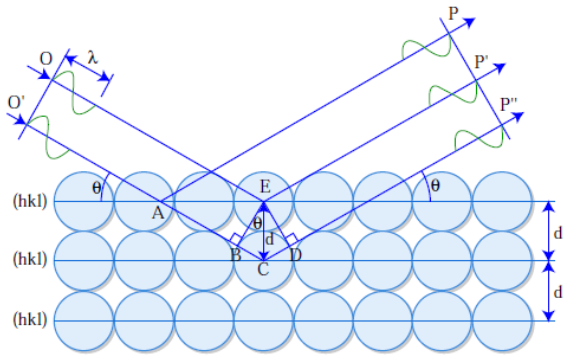

Figure 2.3: Diagram of the Bragg reflection process [6].

2.4.1.2. Field Emission Scanning Electron Microscopy (FESEM)

The morphological properties were evaluated with field emission scanning electron microscope (FESEM) (JEOL-7500, equipped with EDS analyzer). The scanning electron microscope (SEM) is one of the most versatile instruments available for the examination and analysis of the microstructure morphology and chemical composition characterizations. The

principal of electron microscope is the same as a light microscope but instead of using visible light it use very energetic electrons as a source. However, the resolution of the optical microscope is limited by its wavelength compared to accelerated electrons which have very short wavelength. This is what makes it possible to see very small features [7].

2.4.1.3. Energy-dispersive X-ray spectroscopy (EDS)

Energy-dispersive X-ray spectroscopy (EDS) is an analytical technique used for the elemental analysis of chemical characterization of a sample. It is one of the variants of X-ray fluorescence spectroscopy, which relies on the investigation of a sample through interactions between electromagnetic radiation and matter, analyzing X-rays emitted by the matter in response to being hit by electrons, its characterization capabilities are due, in large part, to the fundamental principle that each element has an unique atomic structure, allowing X-rays that are characteristic of an element's atomic structure to be identified uniquely from one another. An EDS system is comprised of three basic components, the X-ray detector, the pulse processor, and the analyzer, that must be designed to work together to achieve optimum results. In practice, the X-ray detector first detects and converts X-rays into electronic signal. Then, the pulse processor measures the electronic measures the electronic signals to determine the energy of each X-ray detected. Finally, the analyzer displays and interprets the X-ray data.

2.4.1.4. X-ray photoelectron spectroscopy (XPS)

The X-Ray Photoelectron spectroscopy technique allows one to perform chemical analysis of surfaces by gathering information of the elemental composition, valence and electronic states. The XPS experiments should be driven in ultra-high vacuum (UHV) conditions

(typically 10^{-9} -10^{-10} mbar). XPS spectra are obtained by irradiating the material with a beam of monochromatised X-ray photons stemming from aluminum or magnesium sources. Electrons, within a depth of a few nanometers, can absorb the X-rays and leave the material with a characteristic kinetic energy, directly related to their binding energy (E_b) [8]. In this regard, a typical XPS spectrum is a plot of the number of electrons arriving at the detector as a function of the binding energy of the collected electrons. The E_b of each emitted electron can be calculated through the equation: $E_b = E_{ph} - E_k - \Phi_{sp}$. Here, E_{ph} and E_k represent the energy of the absorbed X-rays and the kinetic energy of the emitted electron, as measured by the analyzer, respectively. In turn, Φ_{sp} is the work function of the spectrometer, taking into account the difference of kinetic energy seen at the detector with respect to the kinetic energy seen at the sample. The emerging characteristic peaks, or binding energies, identify the atoms present at the surface and their electronic configuration. The XPS technique is not restricted to crystals because it is a non-destructive technique that can measure the surface chemistry of any material. The XPS measurements described in the present work were carried out in a SSX-100 (Surface Science Instruments) photoemission spectrometer, with a monochromatic Al Kα X-ray source (hν=1486.6 eV, base pressure during measurement: 10^{-10} mbar).

2.4.1.5. Raman spectroscopy

Raman spectroscopy is used to probe the lattice vibrations of the solid and their coupling to magnetic properties. In solid state physics quantised lattice vibrations accessible for optical spectroscopy are called optical phonons. The investigation of phonons can be used to gather information about chemical composition, state of order or disorder within a crystal or their possible coupling to other order parameters (e.g. the magnetic structure). Raman spectroscopy is based on the analysis of inelastically scattered light, which goes along with

the generation or annihilation of a quasi-particles. Examples for such quasiparticles are elementary excitations of the lattice (phonons), the spin structure (magnons), or collective oscillations of the free electron density (plasmons). In a Raman experiment the spectral distribution of the scattered light is analysed relative to the position of the elastically scattered light [9]. The interaction of the incident photons with the investigated material leads to the creation or annihilation of optical phonons and, thus, to an energy loss or gain of the scattered photons, respectively. It manifests itself in the appearance of red– (lower energy) or blue–shifted (higher energy) lines with respect to the Laser line in the spectrum of the scattered light. These shifts are called Stokes and Anti–Stokes shift, respectively. The intensity ratio between Stokes and Anti–Stokes shift is essentially determined by the thermal occupation of the phonon states. Within this thesis the Raman spectra are investigated at room temperature. The information that can be directly extracted from a Raman spectrum are phonon frequency, linewidth and intensity (i.e. the scattering cross section). Depending on the sample system various physical properties can be deduced from these quantities. It is noted that the inelastically scattered Raman signals are rather weak. Thus, the experimental requirements for a Raman setup concerning e.g. stray light rejection or spectral resolution are rather strict. A micro-Raman setup is used for the experiments of this thesis. A Laser light source is coupled into an optical microscope via a beam splitter, where the beam is focused onto the sample. This way, a spatial resolution in the range of a few microns and a drastic increase of the beam power density can be achieved.

2.4.1.6. Atomic force microscopy (AFM)

Basically, the Atomic Force Microscope (AFM) consists of a microscale cantilever with a sharp tip at its end that is used to scan a sample surface. The cantilever is typically silicon or

silicon nitride with a tip radius on the order of 10 nanometers. When the tip is approached to the sample surface, forces between the tip and the sample lead to a deflection of the cantilever. Typically, the deflection of the cantilever is measured by detecting the movements of a laser spot that is reflected from the top of the cantilever into an array of photodiodes. The AFM can be operated in a number of modes, depending on the application, but the AFM images presented in this thesis were performed using the AFM in tapping mode, which is gentler on the sample and the tip than the contact mode [8]. In tapping mode, the cantilever vibrates with a frequency close to its resonance frequency. The amplitude of this oscillation is typically 100 nm. Due to forces acting on the cantilever when the tip is approaching the surface, the amplitude of the vibration decreases. The height of the cantilever is modified by the system electronics using a piezoelectric actuator, in such a way that constant amplitude of the cantilever vibrations is kept during the scanning of the surface by the AFM tip. Tracking the cantilever height results in a map of the area that represents the topography of the sample.

2.4.2. Electrical Properties

The electrical and dielectric properties were studied by means of transport measurements, using four probes configuration, and complex impedance spectroscopy, respectively. The electrical and dielectric measurements were carried out as a function of the temperature and/or frequency

2.4.2.1. Electrical Transport

Figure 2.4 shows a schematic diagram of a typical four-point probe. The four-point probe is generally used to measure the resistivity of a single crystal sample [10]. It consists of four

thin wire collinear probes usually made of cooper or tungsten. The errors due to electrical contacts are absent because the current and voltage leads are separate. To measure the resistivity of a sample under study, these probes are placed at equal distance *S* on the sample surface. From a constant-current source, a fixed quantity of electric current *I* is made to flow through the sample using the two outer probes. A voltage drop *V* is measured between the two inner probes. Hence, the resistivity ρ of the sample can be calculated by using the formula $\rho = V/I(A/L)$. In the latter formula *A* represents the cross sectional area of sample in cm^2, and *L* the distance between voltmeter leads in cm.

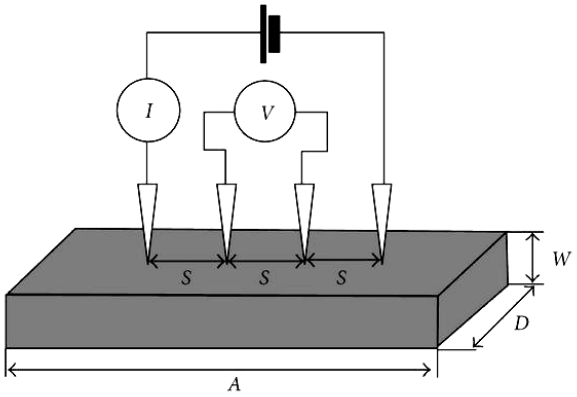

Figure 2.4: Four probes method picture, Four-Point Collinear Probe Resistivity Configuration.

2.4.2.2. Complex impedance spectroscopy

Impedance spectroscopy (IS) is a powerful method to characterize many of the electrical properties of materials and their interfaces with electronically conducting electrodes. It may be used to investigate the dynamics of bound or mobile charge in the bulk or interfacial regions of any kind of solid or liquid material. Moreover, measurements of the capacitance and the dielectric loss of a material can suply valuable information about phase transitions and conduction processes in a dielectric [11]. Sometimes, the accomplishment of such

measurements can be arduous due to issues distinguishing intrinsic and extrinsic behavior. This is particularly difficult in thin films, where leakage currents and interface effects can be important.

In general case, the capacitance and the loss of a dielectric sandwiched in between two parallel electrodes can be written as $C=\varepsilon_0\varepsilon' A/d$ and $\tan(\delta)=\varepsilon''/\varepsilon'$, being ε_0 the permittivity of free space, ε' and ε'' the real and imaginary part of the dielectric permittivity of the material. Moreover, A is the area of the electrodes and d is the thickness of the sample.

The transfer function, $G(j\omega)$, of a system can be determined as the ratio between the output and the input, i.e. $G(j\omega)=[X_{out}(j\omega)]/[X_{in}(j\omega)]$. For the special case where the output signal is the voltage and the input (or excitation function) the current, the transfer function is the system impedance, $Z(j\omega)$. Hence, $G(j\omega)\equiv Z(j\omega)=[E(j\omega)]/[I(j\omega)]$. Since the output may change both in amplitude and phase, with respect to the input, the impedance should be express as a complex number, i.e. $Z(j\omega)$. $=Z'+Z''$.

According to the Debye′s model, dielectric relaxation in a system can occur as a result of a delay of the response of a dipole under an alternating electric field due to a surrounding viscous medium [12]. Within this model, the permittivity is given by the equation $\varepsilon(\omega)=\varepsilon_\infty+(\varepsilon_s-\varepsilon_\infty)/1+j\omega\tau$. In the latter equation, τ is the relaxation time associated with the orientation process, ε_s the static permittivity (zero frequency limit), ε_∞ is the permittivity at optical frequencies, and ω is the (angular) frequency of the applied electric field. The real and imaginary part of the Debye′ equation can be expressed as $\varepsilon'(\omega)=\varepsilon_\infty+(\varepsilon_s-\varepsilon_\infty)/1+(\omega\tau)^2$ and $\varepsilon''(\omega)=\omega\tau(\varepsilon_s-\varepsilon_\infty)/1+(\omega\tau)^2$. Hence, it is expected that in a Debye-like relaxation, ε' and ε'' show a step and a peak, respectively, at the relaxation frequency, τ^{-1}. Interestingly, by

measuring the dependence of the impedance functions on the frequency at a given temperature allows one to calculate the equivalent circuit of a material and separate thus the intrinsic and extrinsic dielectric behavior. This is very important when measuring materials in thin film form. Complex impedance measurements were performed using a HIOKI 3532-50 impedance analyzer. A two-electrode, in-plane configuration and a home-built sample holder were employed for the measurements. Cooper wires were connected to the extremes of the film (separation of about 3 mm) by using silver paint. The complex dielectric properties of the bulk samples were investigated in the 0.1 Hz-5 MHz frequency range at temperatures varying between 300 and 425 K.

2.4.3. Thermal transport

In a crystal, the thermal conductivity is determined by heat carrying quasiparticles. The thermal conductivity κ can be generally expressed by the equation $\kappa=(1/d)cv\ell$, where d denotes the dimensionality, c the specific heat, v the group velocity, and ℓ the mean free path of the respective heat carrying excitations [13]. In most cases two kinds of excitations are responsible for the heat transport: phonons and electrons. The theoretical description is usually based on the Debye model in the first case, and on the electronic gas theory for the latter case. In turn, the thermopower S is defined by $\boldsymbol{S}=\boldsymbol{\varepsilon}/\nabla T$ and describes the electrical field caused by a heat gradient, with the additional condition that no electrical current is allowed to flow. Here, $\boldsymbol{\varepsilon}$ is the sum of the electrostatic field $\boldsymbol{E}$ and the gradient of the chemical potential, $\nabla\mu$, [$\boldsymbol{\varepsilon}=\boldsymbol{E}+(1/e)\nabla\mu$] [14]. The generation of a heat gradient by an electrical current is called Peltier effect. In metals electrons and holes contribute to charge transport. When only electrons are considered and a temperature gradient is applied along the sample, the electrons are faster in the hot side of the sample [15]. Therefore, electrons coming from the

hot side of the sample have a larger velocity, which causes electron diffusion from the hot side to the cold side. Since no current flows, a voltage is generated which leads to a steady state. If electrons and holes are present, the thermo voltage would vanish, if both types of charge carriers move in the same way. This is not the case in reality because of the different mobilities of the quasiparticles. The thermopower vanishes for $T \rightarrow 0$, due to the vanishing of the entropy according to the third law of thermodynamics. Since the mean free path is generally energy dependent, different scattering takes place for the electrons coming from the hot end of the sample compared to the electrons with the opposite direction. The energy dependence of the mean free path is not known well in general, and can cause a complex behavior of *S*. Here, it is important to mention that although the phonons itself do not contribute to the thermopower, they can drag charge carriers by the phonon-electron interaction, and enhance the thermopower in this way. At high temperatures this effect is negligible, because phonon-phonon interaction dominates. At low temperatures the drag effect becomes important.

Measurements of thermal conductivity, and thermopower (Seebeck effect), are done providing a heat supply (external perturbation) to the sample and measuring the heat gradient over the sample. Here, only longitudinal effects are regarded, so the response of the samples is measured in the same spatial direction as the perturbation. The measurements in this thesis were performed in the Instituto de Investigaciones en Materiales at the Universidad Nacional Autonoma de Mexico, using a Physical Property Measurement System (PPMS) of Quantum Design. The Thermal Transport Option (TTO) measures thermal conductivity by monitoring the temperature drop along the sample as a known amount of heat passes through the sample. The TTO measures the thermoelectric Seebeck effect as an electrical voltage drop that

accompanies a temperature drop across certain materials. The TTO system performs these two measurements simultaneously by monitoring both the temperature and voltage drop across a sample as a heat pulse is applied to one end. All three measurement types are essential in order to assess the so-called thermoelectric figure of merit, $ZT=S^2\sigma T/\kappa$ (σ is the electrical conductivity), which is the quantity of main interest for thermoelectric materials.

2.4.4 Magnetic properties

The $Tb_{1-x}Al_xMnO_3$ bulk samples and the thin films were characterized after their magnetic properties using vibrating sample magnetometry (VSM). A versalab VSM magnetometer (Quantum Design) was employed to record the magnetization as a function of the temperature and magnetic field. Shortly, VSM is based on Faraday's law which states that an electromagnetic force is generated in a coil when there is a change in flux through the coil [16]. In the measurement setup, a magnetic sample is moving in the proximity of two pick up coils. The oscillator provides a sinusoidal signal that is translated by the transducer assembly into a vertical vibration. The sample which is fixed to the sample rod vibrates with a given frequency and amplitude (60 to 80 Hz and 1 mm, respectively). It is centered between the two pole pieces of an electromagnet or a superconducting magnet that generate a magnetic field H_0 of high homogeneity. Normally, stationary pickup coils are mounted on the poles of the electromagnet/magnet. The symmetry center of the coils coincides with the magnetic center of the sample. Hence, the change in magnetic flux originating from the vertical movement of the magnetized sample induces a voltage U_{ind} in the coils. The field H_0 is constant and does not affect the voltage. Nevertheless, the field is necessary only for magnetizing the sample [17]. The measurement setup is very sensitive and can detect magnetic moments of down to the μemu range, which corresponds to approximately10^{-9}g of

iron [18]. The measurements of the magnetization of the thin films produced in this thesis were performed using a Quantum Design Magnetic Property Measurement System MPMS7. The MPMS is composed of a liquid-helium cooled SQUID (Superconducting Quantum Interference Device) that measures the changes in the magnetic flux as the sample moves through a superconducting detection coil. This device acts as a very sensitive magnetometer, since it can detect changes as small as one flux quantum, which is appropriate to the measurements on thin films. The MPMS system at the Walther Meissner Institute for low temperatures (Garching, Federal Republic of Germany), used in this thesis, allows the measurement of the magnetic properties from around 2 K up to 400 K under magnetic fields up to ±7 T. The sensitivity of the measurement is 10^{-6}-10^{-8} emu, depending on the setup. However, despite this high sensitivity, measurements on non ferromagnetic ultra-thin films (below 50 nm) are very difficult, as the signal from the layer can be below the sensitivity value and the signal of the substrate may mask that of the film. The samples are inserted in the device by placing them inside a plastic straw (with a low diamagnetic signal) that is attached to the end of the MPMS probe. Most of the measurements presented here are done after zero-field-cooling (ZFC) and field cooling (FC) conditions. For ZFC, the sample is cooled down below its transition temperature under no applied field. A field is then applied at the lowest temperature and the sample is measured upon heating. For the FC measurements, the sample is cooled down through the transition under an applied magnetic field. At the lowest temperature, the field applied during cooling is removed and the same field as used in the ZFC measurement is then applied while the sample magnetization is measured upon heating.

References

[1] S. M. Rossnagel. *Sputter Deposition*. In: W. D. Sproul, K. O. Legg, editors. *Opportunities for Innovation: Advanced Surface Engineering*. Technomic Publishing Co., Switzerland (1995).

[2] R. Behrisch, editor. Sputtering by particle bombardment. In: Applied Physics, **47**, Springer, Berlin (1981).

[3] J. Musil, S. Kadlec, Vacuum **40** (1990) 435.

[4] F. Adibi , I. Petrov , J. E. Greene , L. Hultman, J. E. Sundgren, J. Appl. Phys, **73** (1993) 8580.

[5] W. Friedrich, P. Knipping, M.V. Laue, Acad. Wissen Munich. 303 (1912) 6.

[6] J. C. Anderson, K.D. Leaver, Material Science, Butler and Tanner Ltd (1969).

[7] A. Alyamani and O. M. Lemine. FE-SEM Characterization of Some Nanomaterial, Scanning Electron Microscopy (2012).

[8] Christophe Daumont, Ph.D thesis, University of Groningen (Netherlands), 2009.

[9] S. Issing, P.h.D. thesis, University of Wuerzburg, 2011.

[10] G. P. Panta, D. P. Subedi. Kathmandu university journal of science, 8(2) (2012) 31.

[11] A. K. Jonscher, Dielectrics Relation in Solids, Chelsea Press, London (1983).

[12] P. Debye, Polar Molecules, Dover Publications, New York. 84 (1929).

[13] C. Kittel. Introduction to Solid State Physics, R. Oldenburg Verlag 12. edition (1999).

[14] N.W. Ashcroft and N.D. Mermin. Solid State Physics. Saunders College Publishing New York (1976).

[15] K. Berggold, P.h.D. Thesis, University Köln, 2006.

[16] Vibrating Sample Magnetometry, University of Kiel (Germany) (2015).

[17] K.H.J. Buschow and F.R. de Boer. Physics of Magnetism and Magnetic Materials. Kluwer Academic/Plenum Publishers (2003).

[18] L. Michalowsky, Magnettechnik, Fachbuchverlag Leipzig, (1993).

Chapter 3

Results and discussion

3.1. $TbMn_{1-x}Al_xO_3$ and $Tb_{1-x}Al_xMnO_3$ bulk samples

3.1.1. Structural and microstructural properties

In this section, the experimental results on the characterization of the structural properties of polycrystalline $TbMn_{1-x}Al_xO_3$ and $Tb_{1-x}Al_xMnO_3$ (x=0, 0.05, 0.1, and 0.3) samples synthesized by means of standard solid-state reaction are reported.

It is known that the average size of the A-site cations [1] and the mismatch between the A-site cations [2] decidedly modulate the physical properties of $R_{1-x}A_xMnO_3$ (R = rare earth, A=Ca, Sr, Ba, etc.) compounds. In particular, the $Tb_{1-x}A_xMnO_3$ system is interesting because the Tb-based samples are close to the limit of stability for perovskite compounds and the resulting structure is much distorted [3]. Doping at different sites of $TbMnO_3$ will affect its magnetic, electrical, and structural properties, which may provide insight into the mechanism of this challenging multiferroic material. Due to the difference in the ionic size of Tb^{3+}, Mn^{3+}, and Al^{3+} (the ionic radii are 1.17, 0.535, and 0.645 Å, respectively), it is certainly more reasonable to expect substitution of an Mn^{3+} ion with an Al^{3+} ion instead of substitution of Al^{3+} for Tb^{3+}. Nevertheless, there have been some efforts to substitute Al ions at both the Tb^{3+} and Mn^{3+} sites in $TbMnO_3$ [4, 5]. Indeed, interesting and novel phenomena can occur if the distortion of the $TbMnO_3$ structure is tuned by increasing/reducing the chemical pressure at the Tb^{3+} position. Figure 3.1(a) shows the XRD diffractograms for the $Tb_{1-x}Al_xMnO_3$ polycrystalline samples (x=0, 0.1, and 0.2). The XRD patterns show that all samples are isostructural. Moreover, the recorded diffractograms demonstrate that the compounds are

single-phase within the limit of resolution of the XRD technique. Rietveld refinement of the XRD patterns was used to test the quality of the samples and to obtain the cell parameters with high precision. The results of this procedure confirmed the formation of a single-phase material that adopted the expected orthorhombic structure with the *Pnma* space group. The lattice parameters of the sample with x=0 were *a*=5.305(3) Å, *b*=5.841(8) Å, and *c*=7.408(3) Å at room temperature, and are in accordance with those found in the literature for polycrystalline $TbMnO_3$ samples [6]. The parameters obtained by the Rietveld refinement are listed in Table 3.1. The absence of spurious diffraction peaks is in accordance with a perfect solid solution between Tb^{3+} and Al^{3+} cations in this concentration range. Additional peaks, ascribed to the superstructure and due to the ordering of Al atoms, are also absent in the XRD patterns, at least for samples with $x \leq 0.1$. This result suggests that substitution of Tb^{3+} with Al^{3+} does not lead to an unstable crystal structure. In turn, the sample with x=0.2 shows low-intensity peaks at $2\theta \approx 38°$ and $2\theta \approx 44°$, which can stem from a secondary phase such as $TbMn_2O_5$. The presence of this secondary phase has been reported for the Sn-doped $TbMnO_3$ system at high Sn content [7]. According with the JCPDS 88-0087 crystallographic chart, the peaks at $2\theta \approx 38°$ and $2\theta \approx 44°$ correspond to the (002) and (140) reflections of the $TbMn_2O_5$ phase [8]. Hence it is apparent that doping levels higher than 20 % exceed the saturated solubility in the solid, which could lead to the formation of secondary phases.

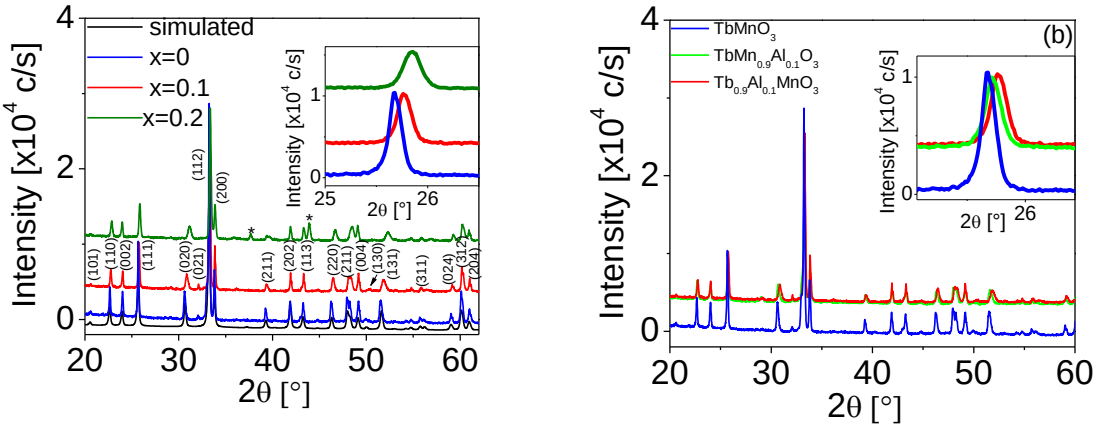

Figure 3.1. (a) XRD powder diffraction patterns for $Tb_{1-x}Al_xMnO_3$ (x=0, 0.1, 0.2) samples recorded at room temperature. The black pattern corresponds to Rietveld refinement for the sample with x=0. Inset: XRD diffractograms plotted on an enlarged scale around the main peaks. (b) XRD patterns of $TbMnO_3$, $Tb_{0.9}Al_{0.1}MnO_3$ and $TbMn_{0.9}Al_{0.1}O_3$ compounds recorded at room temperature. Inset: enlarged plot around 2θ~26 °.

Table 3.1. Parameters obtained by the Rietveld refinement for the undoped and Al-doped $TbMnO_3$ polycrystalline samples.

Compound	**Lattice parameters**			**Cell volume**	**Symmetry**	**Rp**	**Rwp**	**Rexp**	**Chi²**
	a (Å)	**b** (Å)	**c** (Å)						
$TbMnO_3$	5.305(3)	5.841(8)	7.408(3)	229.003	Orthorhombic	38.2	20.1	11.92	2.85
$Tb_{0.9}Al_{0.1}MnO_3$	5.297(6)	5.796(8)	7.414(9)	227.702	Orthorhombic	29.0	17.8	11.19	2.53
$TbMn_{0.9}Al_{0.1}O_3$	5.297(4)	5.828(2)	7.413(9)	228.901	Orthorhombic	27.0	16.2	11.18	2.10

The stability of the $TbMnO_3$ phase upon substitution of Tb with smaller ions (Al, Fe) has also been nicely demonstrated by other authors [3, 9]. A closer examination of the results shown in Fig. 3.1 allows one to observe that the peaks stemming from the Al-doped samples are broadened and slightly shifted to the right side (see inset of Fig. 3.1) as compared to those of the pristine compound (x=0). As already mentioned, it is expected that the substitution of Tb with another cation leads to changes in the unit cell size, according to the tabulated size of the inserted cation [10]. Indeed, the shift of the peaks of the Al-doped sample to higher angles points to a decrease in the interplanar distance. Certainly it is to be expected that isovalent substitution of the large Tb^{3+} ion with the smaller Al^{3+} ion would result in a local

disturbance of the lattice around the Al^{3+} ions in order to relax the strain produced by size mismatch. As a result, the values of the lattice parameters will decrease and the unit cell will shrink as verified by the data listed in Table 3.1. Thus the decrease in cell volume upon Al doping is caused by the size effect. The XRD pattern of a $TbMnO_3$ sample intentionally doped at the Mn site, along with the reference pattern, has also been included for clarity [(Fig. 3.1(b)]. The excellent agreement between the measured and calculated XRD patterns is evidenced in this plot. The absence of spurious diffraction peaks is also verified. Thus all the samples are of single phase. Note that the shifting of the XRD pattern of the $TbMn_{0.9}Al_{0.1}O_3$ sample is less than that of the $Tb_{0.9}Al_{0.1}MnO_3$ one. This is a significant result, which points to the different degree of distortion of the $TbMnO_3$ structure generated by the Al doping on different lattice sites in the compound.

The phase purity of the sample was also examined with Raman spectroscopy. A total of 24 Raman active modes have been identified in orthorhombic $TbMnO_3$ by group theory calculations ($\Gamma=7A_g+7B_{1g}+5B_{2g}+5B_{3g}$) [11]. In an ideal cubic ABO_3 perovskite, all the atoms are situated at centro-symmetric sites and hence do not contribute to Raman modes [12]. In the orthorhombic structure *Pnma*, the atoms occupy four non-equivalent atomic sites (R, Mn, O1 and O2,). Here, only Mn site is at the center of symmetry. The distortion caused due to the motion of oxygen atoms in MnO_6 octahedra around the Mn ion is responsible for the Raman active vibrations. Thus, almost all observed Raman active phonons are mainly displacements of the O^{2-}, the slight frequency shifts (Fig. 3.2) originate then from an indirect effect, namely the doping with Al-ions. Room temperature Raman spectroscopic data for the present $TbMnO_3$ sample is shown in Fig. 3.2. Several Raman modes centered at ~274 cm^{-1} [Ag(7/2)] that corresponds to an Ag in-phase rotation of the MnO_6 octahedra, ~376 cm^{-1} that

corresponds to Ag tilting mode of the MnO_6 octahedra, ~487 cm^{-1} [Ag(1/3)] that corresponds to O2 anti-stretching and MnO_6 bending, ~507 cm^{-1} that corresponds to MnO_6 bending and O2 antistretching, ~610 cm^{-1} [B_{2g}(1)] that corresponds to in-plane O2 stretching (=breathing mode) [13]. The three additional low-frequency modes observed in the spectrum correspond to the vibrational modes of the Tb^{3+} ions [11]. No second-order Raman scattering, attributed mainly to the oxygen vibration mode at 650 cm^{-1}, was observed in the analyzed samples [11]. The peaks ~487 and 610 cm^{-1} related to the modes involving Mn–O bond stretching vary when a mixed Mn valence is present, further confirming the absence of oxygen vacancies in the present $TbMnO_3$ sample [14]. The effect of Al-doping at different sites in the $TbMnO_3$ structure is clearly observed in the Raman peaks. It is important to note that no additional peaks, stemming from additional functional groups, are appearing in the $TbMnO_3$ spectrum upon Al-doping. This suggests a correct dilution of the Al-ions in the structure of the parent compound. The Raman mode positions of the $Tb_{0.9}Al_{0.1}MnO_3$ sample shifts towards the high frequency, whereas those $TbMn_{0.9}Al_{0.1}O_3$ remain in their positions but with increased widths. This remarkable difference is originated by the different degree of distortion of the $TbMnO_3$ structure generated by the Al-doping on different lattice sites in the compound. A general trend observed in the Raman spectra of $RMnO_3$ series is that the phonon frequencies increase with decreasing R^{3+} ion radius [15]. As almost all observed Raman active phonons are mainly displacements of the O^{2-}, the frequency shifts originate from an indirect effect. Certainly, the tilting angle of the MnO_6 octahedra depends on the ionic radii of the R^{3+}. When these are decreased by replacing R^{3+} with another isovalent ion with a smaller ionic radius, the Mn–O–Mn bond angle also further decreases, which is equivalent to an increase of the MnO_6 tilting. This implies a shift of the O^{2-} equilibrium position away from the Mn–Mn axis. This shift, in turn, influences the phonon frequencies of the Raman–active phonons. The amount

of these frequency shifts depends on the individual phonon modes. For instance, the shift of the Ag(7/2) mode can be explained by a displacement of the apical O^{2-} of the MnO_6 octahedra along the orthorhombic *a*-axis and an out-of-phase rotation of the MnO_6 octahedra along the *a*-axis, respectively [15]. It can be visualized, that these Eigendisplacements are sensitive to a change of the Mn–O–Mn tilting angle along the *b*-axis. The frequency of a mode involving stretching vibrations of O(2) atoms in the *xz* planes is determined by the Mn–O(2) distances. In the present investigation when Al is doped on the Mn site, the Mn–O(2) distances should decrease, which leads to a marked broadening of the modes at ~487 and 610 cm^{-1}. These two modes, as signalized above, are due to MnO_6 bending and in-plane O(2) stretching. Thus, the broadening should be a consequence of lattice disorder as induced by Al doping on the Mn site [16]. Finally, the shift in the spectrum observed when Al is doped on the Tb site is accompanied by an increase in the peak intensity ratio upon Al-doping (e.g. $I_{610}/I_{376}\approx 2.9$, and 3.2, for the undoped and Al-doped simple, respectively). This result is consistent with the observations reported in Ref. [13]. This finding can be ascribed to the fact that the Al doping increases the distortion and decreases the bond lengths which lead to increase the Raman intensity [16].

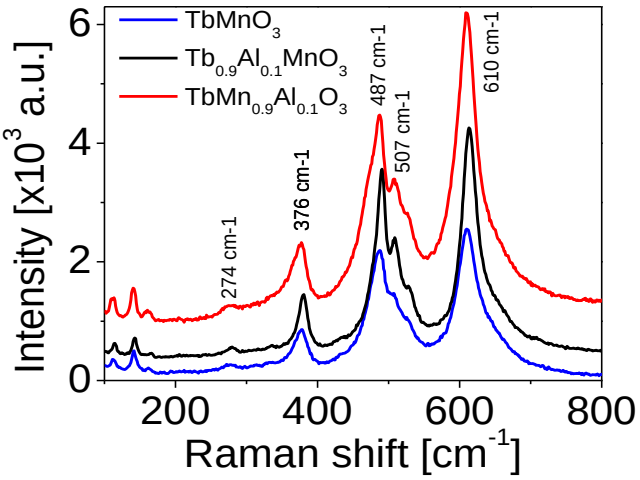

Figure 3.2. Room temperature Raman spectrum of bulk undoped and Al-doped $TbMnO_3$ samples with peaks corresponding to Raman modes indicate by arrows.

3.1.2. Morphological properties

SEM micrographs for the $TbMnO_3$ and $Tb_{0.8}Al_{0.2}MnO_3$ samples are presented in Fig. 3.3. The micrographs show uniform crystallite size distribution ranging between 1 and 3 μm. The size of the crystallite of the Al-doped sample decreases which is concomitant with increasing in the grain boundaries. The decrease in the size of the crystallites is due to the nucleation mechanism of the $TbMnO_3$ phase. The Al doping may enhance the nucleation of the $TbMnO_3$ phase resulting in a smaller crystallite size as a consequence.

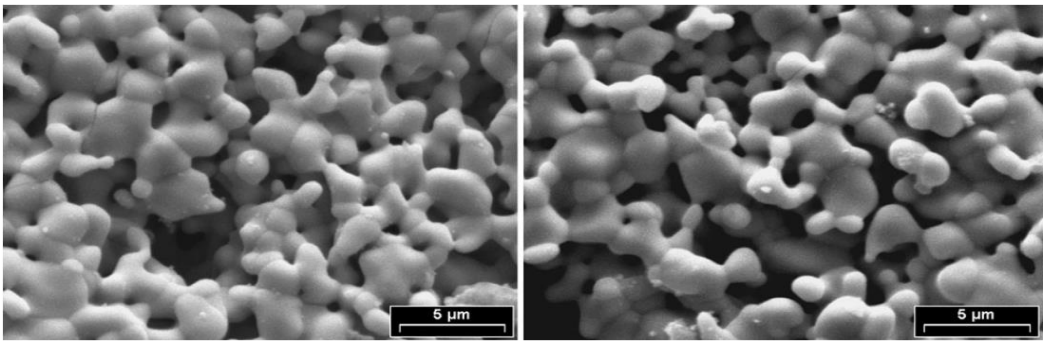

Figure. 3.3. SEM micrographs for the $TbMnO_3$ (left) and $Tb_{0.8}Al_{0.2}MnO_3$ sample (right).

3.1.3. Electrical and dielectric properties

In this section, the experimental results on the electrical and dielectric characterization of polycrystalline $Tb_{1-x}Al_xMnO_3$ (x=0, 0.05, 0.1, and 0.3) samples, synthesized by means of standard solid-state reaction, are presented in detail. As previously expressed, direct current (dc) resistivity measurements were performed using a four point contact method. The dielectric measurements in turn were carried out by complex impedance spectroscopy. Here, a two-electrode configuration [ss|sample|ss (ss: stainless steel)] and a home-built temperature– and atmosphere controlled cell were employed for the measurements. The complex dielectric properties of the ceramic samples were investigated in the 40 Hz to 5 MHz frequency range a temperatures above 300 K.

In the following, we explore the effect of Al doping on the transport properties of $Tb_{1-x}Al_xMnO_3$ samples with Al fraction $0 \leq x \leq 0.2$. The temperature dependence of the electric resistivity of $Tb_{1-x}Al_xMnO_3$ samples is shown in Fig. 3.4. The $\rho(T)$ data were recorded during a heating cycle in absence of an external magnetic field.

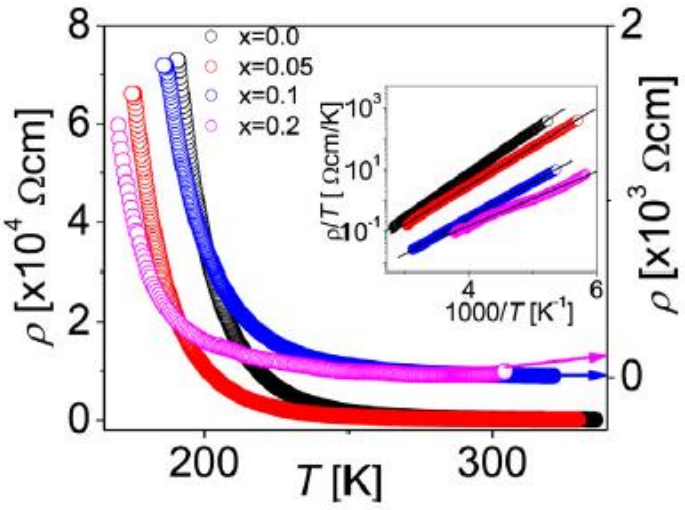

Figure. 3.4. Temperature dependent resistivity for $Tb_{1-x}Al_xMnO_3$ samples with Al content x=0, 0.05, and 0.1 and 0.2. Inset: variation of ln(ρ/T) versus 1000/T for the samples in the main panel.

The semiconductor-type character of the measured samples is vividly recognized from this plot. The value of the resistivity is strongly dependent on the temperature and increases conspicuously as the temperature is lowered. Although the $\rho(T)$ behavior is similar for the three curves, a dramatic reduction of the resistivity is verified upon Al doping. Certainly, whereas the resistivity of the pristine sample amounts to 230 Ωcm at 300 K, this is reduced to 13 Ωcm for the sample with x=0.1. This finding spurs the possibility of application of this material in practical thermoelectric devices. Here, it should be stressed that the low electrical conductivity of the some ceramics represents a major obstacle for thermoelectric applications. In order to understand the temperature dependence of resistivity, the data were first analyzed in terms of thermal activation (TA): log $\rho \propto 1/T$, Efros-Shklovskii-type hopping (ESH): log $\rho \propto T^{-1/2}$, Mott's variable range hopping (VRH): log $\rho \propto T^{-1/4}$, and polaronic transport (PT): log $\rho/T \propto 1/T$ models for conductivity. It is found that the PT model describes the temperature dependence of resistivity variation over the entire temperature range precisely (inset to Fig. 3.4). In this regard, it is well known that a transition in the nature of

carriers from bound polarons at low temperatures to free carriers at elevated temperatures leads to a characteristic resistivity variation, given by $\log \rho/T \propto 1/T$ [17]. Here, it should be pointed out that the temperature dependence of the resistivity, which is well described by the polaronic model, is not linked to a ferromagnetic phase as it is the case for other perovskite-type novel materials [18]. Certainly, for polycrystalline $TbMnO_3$ samples, well-defined ferromagnetism is only observed at temperatures below ~50 K [19]. The activation energies can be calculated from the fitting procedure performed previously using the equation $\rho=\rho_0 T\exp(E_\rho/k_B T)$ (inset to Fig. 3.4). In the latter equation, k_B is Boltzmann's constant and E_ρ the activation energy. The activation energies E_ρ obtained from the slope of the straight line are presented in Table 3.2.

Table 3.2. Values of activation energies (E_ρ and E_S) estimated from resistivity and thermopower measurements on $Tb_{1-x}Al_xMnO_3$ samples. The constant term (α) is also given for the samples.

Al fraction	E_ρ (meV)	E_S (meV)	α
0	280	40	2.5
0.05	240	-	-
0.1	220	38	1.8
0.2	-	44	1.7

The doping of polycrystalline $TbMnO_3$ with other elements normally has the aim of tuning the magnetic properties of the compound. It has also been demonstrated that substitution of Al at the Tb site generates a weak ferromagnetic phase in the parent $TbMnO_3$ [4]. The most commonly used experimental technique for characterizing the dynamic of electrons and ions in a diversity of materials is electrical relaxation measurements [20]. The study of the relaxation phenomena in multiferroic $TbMnO_3$ deserves special attention, because the strong magnetocapacitive effect (strong anomaly of the temperature-dependent dielectric constant ε', in the vicinity of magnetic transitions), observed for a specific direction of the electrical

field, is almost completely governed by magnetic-state induced changes of the relaxation parameters [21]. In this connection, complex impedance spectroscopy (CIS) is a nondestructive method that allows studying the microstructural and electrical properties of polycrystalline oxides. Figure 3.5(a) shows the frequency dependence of the real part of the dielectric permittivity (ε_r') recorded at different temperatures for the undoped $TbMnO_3$ sample. The dielectric permittivity was calculated from the impedance data, employing the relation $\varepsilon'_r = Z''/\omega C_0(Z'^2+Z''^2)$.

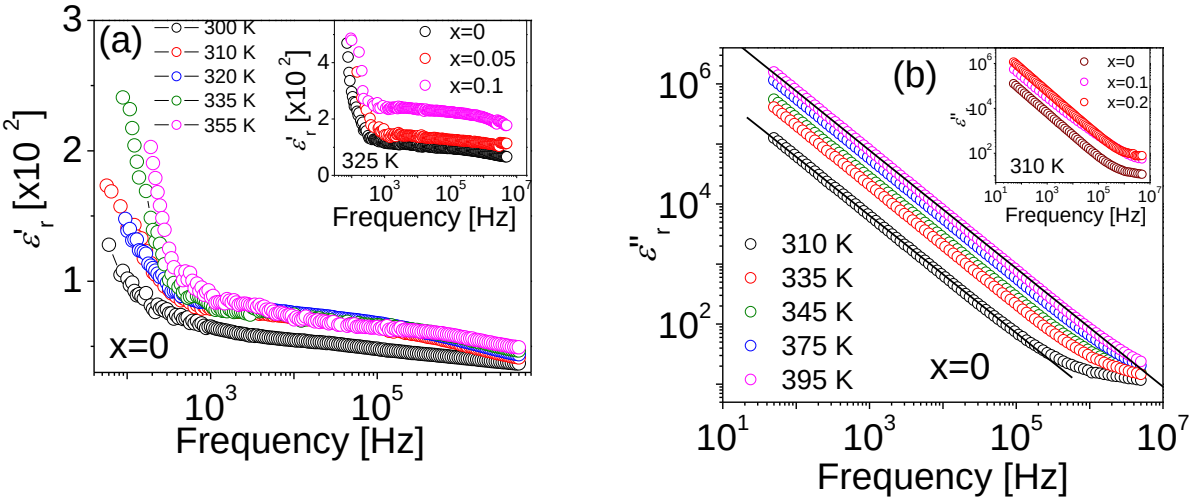

Figure 3.5. (a) Frequency dependence of the real part of the complex permittivity of $TbMnO_3$ measured at various temperatures. Inset: variation of ε'_r with the frequency of $Tb_{1-x}Al_xMnO_3$ (x=0, 0.05, 0.1) at 325 K. (b) Frequency dependence of the imaginary part of the complex permittivity recorded at several temperatures. The solid lines are guides for the eyes. Inset: variation of ε''_r with the frequency of $Tb_{1-x}Al_xMnO_3$ (x=0, 0.1, 0.2) at 310 K.

The dielectric response of the samples is due to the motion of charge carriers, and a strong correlation between the dielectric properties and the crystalline structure should exist in polycrystalline ceramics [22]. The dielectric constant shows a dispersive nature at low frequencies and is considerably affected by the temperature. As the temperature increases,

the dielectric constant rises rapidly at low frequencies, and a strong dispersion is observed at frequencies below ~300 Hz. At higher frequencies, all $\varepsilon_r'(f)$ curves approach a limiting constant value of ε_∞'. The increase in the value of the dielectric constant (particularly in the lower frequency range) with increasing temperature has usually been attributed to the decrease in bond energies [23]. Concretely, an increase in temperature leads to two effects on the dipolar polarization. On the one hand, the increasing temperature weakens the intermolecular forces and thus enhances the capacity for obtaining orientational polarization. On the other hand, a rise in temperature increases the thermal agitation and thus strongly disturbs the capacity for obtaining orientational polarization [24]. Consequently, it was verified that the dielectric constant is larger at higher temperatures and lower frequencies. As the frequency increases, the contribution to the polarizability from ionic and orientational sources decreases and finally disappears, as a consequence of the inertia of the ions. Apart from this, it is also important to examine the dependence of the dielectric constant on the frequency within the framework of the relaxation phenomena in multiferroic materials. Indeed, the relaxation phenomena in such materials are associated with the orientational polarization, which is frequency-dependent. In particular, it has been suggested that the relaxation in $TbMnO_3$ is due to the migration of localized charge carriers [25]. At this point, it is important to point out that many studies on relaxation in multiferroics have mainly been focused on single-crystal samples. Concerning micro-structural and dielectric inhomogeneity, the dielectric response of polycrystalline ceramics is a rather more challenging, open issue. In this connection, the variation of the dielectric properties of $TbMnO_3$ upon Al substitution are probably linked to the structural differences between the crystal lattices of the undoped and Al-doped samples. Certainly it is to be expected that the change in the relative position of ions upon small substitution of Tb^{3+} with Al^{3+} affects the

electronic band structure of $TbMnO_3$. Changes in the structural characteristics, such as the c/a ratio and the cell volume, can produce overlapping bands (or stop the overlapping of two bands, in case of expansion), inducing diverse phenomena such as the creation of a smoother conduction path or a metal– insulator transition [26]. Undoubtedly, further experimental work at the microscopic level is necessary in order to gain a deeper insight into the role of Al in the dielectric behavior of $TbMnO_3$. By using complex impedance analysis, some authors have identified the internal barrier-layer capacitance (IBLC) effects, related to the grain boundaries, as the origin of the high-temperature relaxation in $TbMnO_3$ polycrystals. In turn, the low-temperature relaxation has been ascribed to the dipolar effects induced by charge-carrier-hopping motions inside the grains [27]. Certainly localized charge carriers hopping between spatially fluctuating lattice potentials not only produce the conductivity but also give rise to dipolar effects. With decreasing temperature, the localized carriers become frozen, which reduces the dipolar effects. This leads to a decay in polarization with respect to the applied electric field, which is evidenced by a steep drop in ε_r' at temperatures below ~ 250 K [28]. Moreover, the freezing process leads to a large reduction in the number of the hopping carriers, which greatly increases the resistance, as observed in inset of Fig. 3.4. On the contrary, at high temperatures, the localized holes can promote conductivity through the hopping, which induces the dipolar effect and hence considerable polarization. Consequently, the value of ε_r' increases at high temperatures and lower frequencies, as observed in Fig. 3.5(a). The slight increase in the value of ε_r' with the Al doping [inset of Fig. 3.5(a)] could be linked to changes in the electronic configuration of the Al-doped samples as a consequence of the variation of the chemical pressure at the Tb position, concomitant with lattice distortion. Zhang et al. [29], who observed larger values of ε_r' for La doped $TbMnO_3$

samples in the low frequency region, argued that the increased number of charge carriers in the La-doped sample is probably the mechanism behind the increased values of ε_r'. Nevertheless, no exact information about the doping level and/or lattice site was supplied in that report. The frequency dependence of the imaginary part of the complex permittivity $\varepsilon''_r = Z'/[\omega C_0(Z'^2+Z''^2)]$ for undoped $TbMnO_3$ samples, recorded at different temperatures, is shown in Fig. 3.5(b). The $\varepsilon_r''(f)$ dependence for the Al-doped samples at 310 K is shown correspondingly in the inset of Fig. 3.5(b). The value of ε_r'' increases slightly with the temperature (main panel), with the Al-doping reaching an apparent saturation for concentrations as high as x=0.2 (inset). The curves show that the experimental data fall into a straight line, with a common negative slope of ~ -1 in the frequency range covered, which indicates that the conductivity is the main contribution to ε_r'' [30]. A slight deviation from the straight line is observed at high frequencies for both samples at the lowest temperature (300 K). It is probable that some microdomains (containing small polarized clusters) exist even at such high temperatures. The slow dynamics of the domain walls in these microdomains may contribute to the delay of the response to the external alternating field, particularly at high frequencies [31]. Hence another kind of energy dissipation mechanism arising from "relaxation" first comes into play in the high-frequency range. It is to be expected that at temperatures below 300 K the deviation from the straight line will be more pronounced, which would allow identifying two different regimes, namely a low-frequency dissipation regime related to charge transport, and the relaxation regime, active at higher frequencies and originating from the relaxation of condensed clusters [31].

It is widely known that impedance analysis is a powerful technique often used to separate different dielectric relaxations stemming from the intragrains, intergrains, and electrodes of

ceramic materials [32]. Shown in Fig. 3.6 is the complex impedance plot (Z'' vs. Z') for undoped and 10% Al-doped $TbMnO_3$ samples recorded at different temperatures above 300 K. Only one semicircle, with its center on the real axis, can be observed in this plot. In particular, no arcs can be observed, whether in the low or in the high frequency range. The presence of a semicircle at low frequency is a characteristic of interfacial impedance, while at high frequency the semicircle results from a parallel combination of the bulk capacitance (C_b) and bulk resistance (R_b) of the material [33]. Note also that the semicircles show no inclined spur at low frequency, which normally is due to the electrode polarization. Thus the observed semicircle arcs should correspond to the bulk conduction. The impedance curves show that the resistance of the samples strongly depends on the temperature. With an increase in temperature, the intercept of the arc with the real axis shifts towards the origin, indicating that the bulk resistance of the sample decreases with an increase in temperature, and consequently the conductivity increases. It is also evident from Fig. 3.6 that Al doping leads to reduced values of the bulk resistance of $TbMnO_3$.

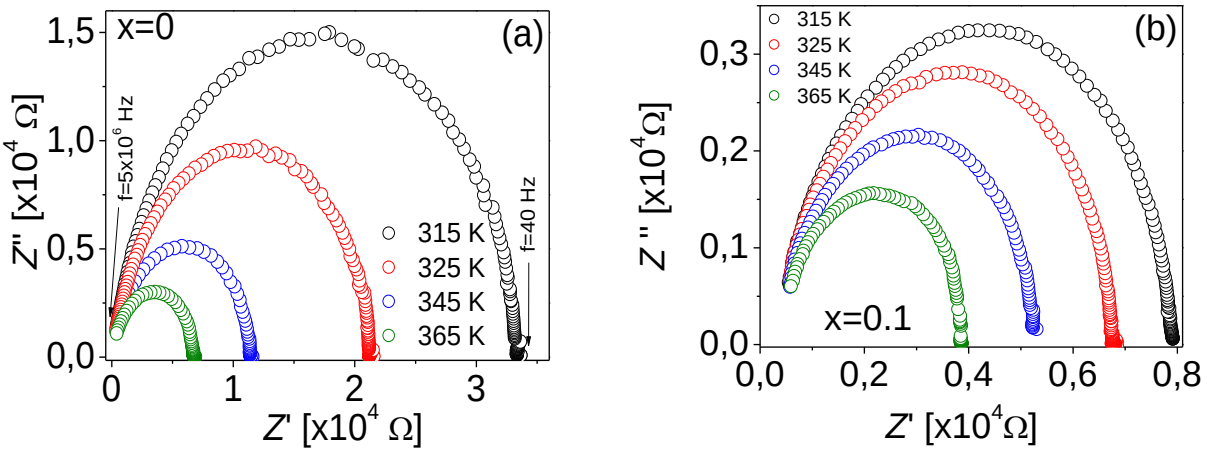

Figure 3.6 Complex impedance plot (Z'' vs Z') for $TbMnO_3$ (a) and $Tb_{0.9}Al_{0.1}MnO_3$ (b) samples recorded at fourth different temperatures.

Figure 3.7(a) and (b) show typical plots of the frequency dependence of the conductance, G, at different temperatures for undoped and 10% Al-doped $TbMnO_3$ samples. Both curves show a medium-frequency plateau, associated with the bulk *dc* conductance of the specimen [$\sigma_0(T)=(d/A)\sigma(0)$] [27]. In this equation, d and A represent the distance between electrodes and the electrode-pellet contact surface, respectively. In addition, Fig. 3.7(a) shows that for a fixed temperature, $G(\omega)$ exhibits dispersion at higher frequencies. The frequency at which dispersion begins to take place (f_p) is the hopping frequency. The characteristic crossover frequency seems to increase with increasing temperature. The increase in the value of the conductance at values higher than f_p suggests a change in the conduction regime in the samples. The same trend is observed for the Al-doped samples, as evidenced in Fig. 3.7(b).

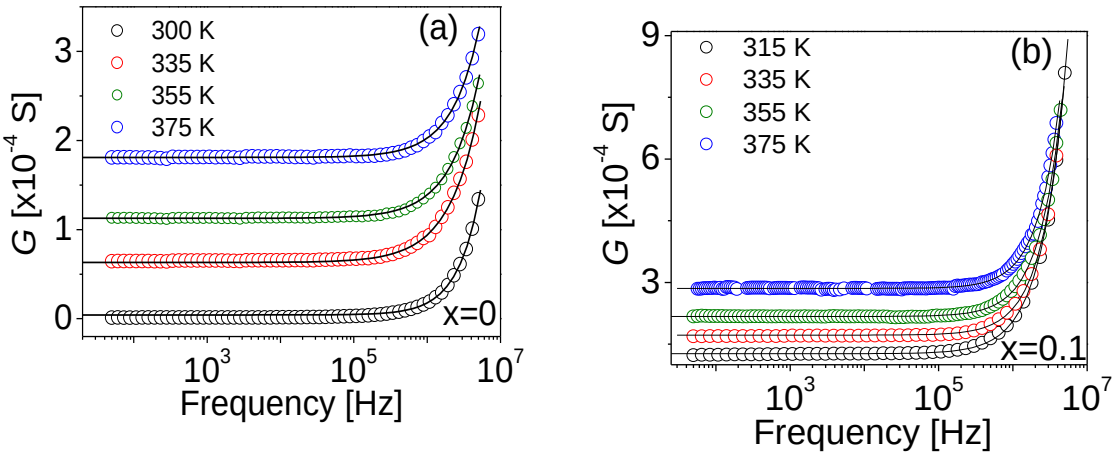

Figure. 3.7. Frequency dependence of the conductance of $TbMnO_3$ (a) and $Tb_{0.9}Al_{0.1}MnO_3$ (b) samples recorded at fourth different temperatures. The solid lines represent the fitting to the experimental data using the universal Jonscher's power law $\sigma(\omega)=\sigma_{dc}+A\omega^n$.

The frequency response of the Al-doped samples [Fig. 3.7(b)] exhibits a behavior similar to the undoped one, although the values of the conductivity are higher at each temperature and the increase in the value of the conductance at frequencies $f>f_p$ is steeply sloped (as opposed to that shown by the undoped samples). Note that the value of $\sigma_0(T)$ increases with increasing

temperature (although the form of the plateau remains unmodified), which means that the conductance is mainly temperature-activated. In this regard, the bulk *dc* conductivity data [$\sigma(0)=\sigma_0$] for undoped and 10 % Al-doped $TbMnO_3$ samples are plotted in Fig. 3.8(a) as log σ_0 versus 1000/T. The conductivity data are well described by the Arrhenius relation, $\sigma=\sigma_0 Exp(E_a/k_BT)$, E_a being the activation energy for *dc* conduction. The value of E_a was recorded as 0.26 eV for the undoped sample, which is in good accordance with that reported in the literature for $TbMnO_3$ [29], and 0.12 eV for the Al-doped one. The lower value of E_a found for the Al-doped sample indicates that the barriers between sites are lower in this sample. Hence the conductivity observed for these samples is higher. As stated above, it is probable that the change in the relative position of the ions upon small substitution of Tb with Al affects the electronic band structure of $TbMnO_3$. A modification of the band structure of the material can create, e.g., as mother conduction path. Figure 3.8(b) shows the temperature dependence of *ac* conductivity versus reciprocal temperature recorded at 2 MHz for the undoped and Al-doped samples. It is evident that the conductivity in the *ac* regime does not obey the Arrhenius relation. Hence the small polaron hopping model given by the relation $\sigma T=\sigma_0 Exp(E_s/k_BT)$ was tested for describing the behavior of the conductivity in the *ac* regime. The slope of the function $\ln\sigma T$ vs. $1/T$ gives the activation energy E_s for the conduction process. The value of E_s for the undoped and Al-doped samples ended up being 0.2 and 0.14 eV, respectively, which follows the same trend as does the *dc* conductivity. It has been suggested that the dielectric relaxation in $TbMnO_3$ at high temperature might be related to hopping conductivity [27]. It is apparent that localized charge carriers hopping between spatially fluctuating lattice potentials not only produce the conductivity but also give rise to dipolar effects. This phenomenon will be discussed in the next section of this thesis.

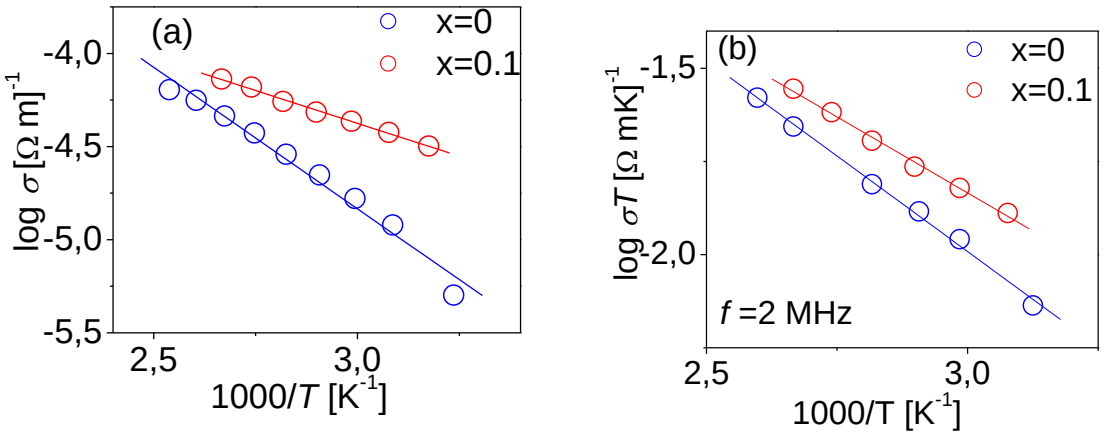

Figure 3.8. (a) *dc* conductivity versus reciprocal temperature for undoped and Al-doped samples. (b) *ac* conductivity versus reciprocal temperature recorded at 2 MHz for the undoped and Al-doped samples.

A convenient formalism for investigating the frequency behavior of conductivity in a variety of materials is based on the power relation proposed by Jonscher, $\sigma_{ac}(\omega)=\sigma_{dc}+A\omega^{n}$, where σ_{ac} and σ_{dc}, where σ_{ac} and σ_{dc} are the *ac* and *dc* conductivities of the sample, respectively [34]. The *dc* conductivity is due to excitation of electrons from a localized state to the conduction bands. Moreover, A is a pre-exponential factor determining the strength of the polarizability and n the frequency exponent, which has an important physical consequence [35]. Indeed, $n\leq1$ implies that the hopping motion involves a translational motion with a sudden hopping (hopping process through long distance), whereas $n>1$ implies that the motion involves localized hopping without the species leaving the neighbors (hopping between neighboring sites). Both A and n are temperature- and material-dependent [36]. By fitting the conductance data of the samples using the mentioned power relation, the A and n values are varied simultaneously in order to get the best fits. It can be observed in Fig. 3.8 that the fitting curves (solid lines) perfectly match the experimental data. The resulting fitting parameters are listed in Table 3.3.

Table 3.3. Fitting parameters obtained by applying the Jonscher power law $\sigma(\omega)=\sigma_{dc}+A\omega^n$ to the experimental data of the conductance versus frequency for $Tb_{1-x}Al_xMnO_3$ (x=0, 0.1) samples at various temperatures.

x=0					x=0.1			
T [K]	σ_{dc} (x10^{-5})	A	n	R^2	σ_{dc} (x10^{-5})	A	n	R^2
300	0.42	5.57x10^{-14}	1.39	0.999	13	7.84x10^{-13}	1.33	0.998
335	6	1.40x10^{-11}	1.05	0.999	17	2.20x10^{-13}	1.41	0.999
355	11	6.38x10^{-12}	1.10	0.998	22	2.25x10^{-13}	1.40	0.999
375	18	2.26x10^{-12}	1.16	0.998	29	9.21x10^{-14}	1.46	0.998

In order to corroborate the strength of the fit, the squared linear correlation coefficients (R^2) have also been included in Table 3.3. It can be observed in this table that the values of n obtained for both samples at all the considered temperatures are larger than 1, which suggests that hopping occurs between neighboring sites. The fact that in general the values of n for the Al-doped samples were larger than those for the undoped ones suggests that the porosity of the $TbMnO_3$ samples was improved by the Al doping.

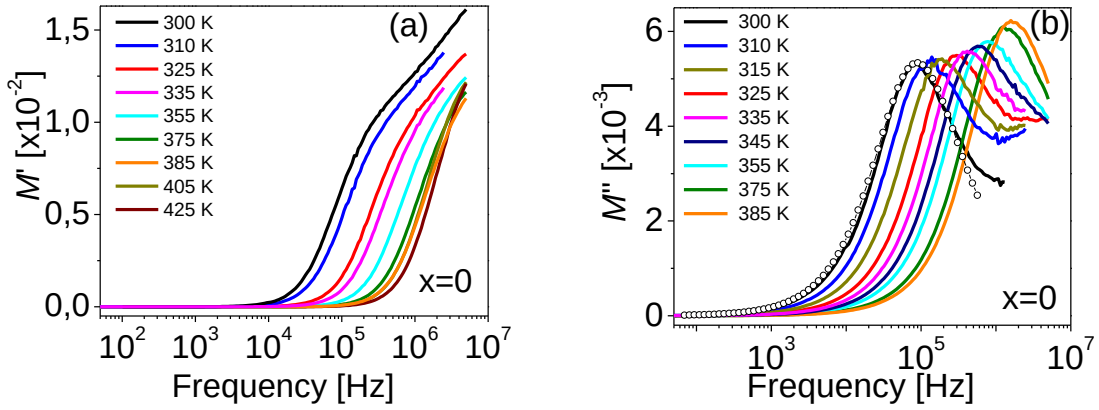

Figure 3.9. Frequency dependence of (a) real (M') and (b) imaginary (M'') dielectric modulus at different temperatures for $Tb_{1-x}Al_xMnO_3$ (x=0). The open symbols represent the best fit to the experimental data at 300 K according to the modified KWW function.

The relaxation phenomena in the system can be analyzed within the framework of the Modulus formalism. It is known that in an equivalent circuit, the $Z''(\omega)$ values are dominated by the resistive elements, whereas the $M''(\omega)$ values are governed by the capacitive elements

[37]. The electric modulus is defined as the reciprocal of the complex dielectric permittivity ($M^*=1/\varepsilon^*$) and corresponds to the relaxation of the electric field in the system when the electric displacement is constant. Hence the electric modulus, defined by the relation $M^*(\omega) = M'(\omega) + iM''(\omega) = (\varepsilon_\infty)^{-1}[1 - \int_0^\infty \exp(-i\omega t)(-d\varphi(t)/dt)dt]$, can be employed to represent the real dielectric relaxation process in a particular system [38]. In this equation, $\varepsilon(\infty)$ represents the asymptotic value of the real part of the dielectric constant [$\varepsilon(\infty)=1/M'_\infty$], and $\phi(t)=\phi(0)\exp[-(t/\tau)^\beta]$, the Kohlrausch–Williams–Watts (KWW) function of the material [39]. The Kohlrausch exponent parameter β ($0<\beta<1$), representing the stretching coefficient, provides information on the degree of correlation between ions during conduction processes. In this regard, a value of one corresponds to completely uncorrelated ionic motion. It has been demonstrated that the calculated values of β are temperature-independent for a given sample composition [37]. Figure 3.9 shows the dependence of M' and M'' on the frequency for $TbMnO_3$ samples recorded at different temperatures. On the basis of this curve, it is evident that $M'(\omega)$ undergoes dispersion, tending towards M_∞, which is the asymptotic value of $M'(\omega)$ at higher frequencies [Fig. 3.9(a)]. At low frequencies, $M'(\omega)$ approaches zero, suggesting that the contribution of the electrode polarization to M^* is negligible. Thus the dispersion of $M'(\omega)$ is mainly due to conductivity relaxation [40]. Note that the onset of dispersion shifts toward higher frequencies with increasing temperature, which indicates that the relaxation processes are spread over a range of frequencies. In turn, the imaginary part of the complex modulus, $M''(\omega)$, features a maximum (M''_{max}) at frequency f_m. The peaks appearing at f_m are generally associated with charge carrier relaxation phenomena. Upon increasing the temperature, the shape of the spectrum remains almost constant (except at higher frequencies) but f_m shifts to higher frequencies. In addition, the

peak height shows a sizeable variation with the temperature, which suggests that the dielectric constant and the distribution of relaxation are not completely invariant upon increasing the temperature [41]. It has been established that in the frequency region below M''_{max}, the charge carriers can move long distances by hopping from one site to another [37]. In contrast, in the frequency region above M''_{max}, the charge carriers are only mobile over short distances. This is a consequence of the fact that the charge carriers in this region are spatially confined to potential wells. Thus their movement is localized within the wells. Furthermore, it can be observed that the obtained $M''(f)$ plots are asymmetric with respect to the peak maxima at all temperatures. The width of the peaks is also considerably broader on both sides of the maxima than would be predicted by the ideal Debye behavior. As the temperature increases, the dielectric relaxation becomes thermally activated. Hence the most probable relaxation time τ_m ($\omega_m \tau_m=1$) can be represented by the Arrhenius relation $\tau_m = \tau_0 \exp(E_\tau/k_B T)$, τ_0 being the relaxation time at an infinite temperature, E_τ the activation energy for the dielectric relaxation, k_B Boltzmann's constant, and T the temperature in K. The value of E_τ calculated from the slope obtained by the least square fitting of data in Fig. 3.10(a) was 0.25 eV in the temperature range 300–425 K. For the Al-doped sample (x=0.1), a value of 0.16 eV was found for E_τ in the same temperature range [Fig. 3.10(b)]. Probably the lattice distortion due to the aluminum substitution facilitates the induction of polarization in the system as compared to pure $TbMnO_3$. Hence the reduced value of E_τ for the Al-doped sample. It is interesting to note that in the present study of undoped and Al-doped samples both the hopping frequency and the *dc* conductivity are thermally activated, indicating that they originate from the migration of the charge carriers. Note that the activation energy calculated from the conductivity relaxation time matches well with the activation energy for the

conduction process, due to the hopping polaron mechanism, as obtained from the curve in Fig. 3.8. This indicates that the charge carriers in the sample have to overcome the same barrier when conductivity by hopping takes place as well as when relaxing. In polar crystals, the presence of charge carriers such as electrons or holes generates polarization of the atoms in the area surrounding these charge carriers. Hence the displacement of the atoms produces a local lattice distortion [42]. The quasiparticle formed by the electron and its self-induced distortion is called a small polaron if the range of the lattice distortion is of the order of the lattice constant [43]. It has been verified that in the transition metal oxides, charge carriers are able to create small polarons [44]. Note that the activation energy for *dc* conduction E_a [Fig. 3.8(a)] is slightly higher than E_p and E_τ. This difference can be reconciled by considering that whereas E_a is given by the sum of both the energy necessary to create charge carriers and the hopping free energy of charge carriers over long distances, the activation energy for relaxation is equal to the free energy of migration of the charge carriers and their hopping between the adjacent lattice sites [45].

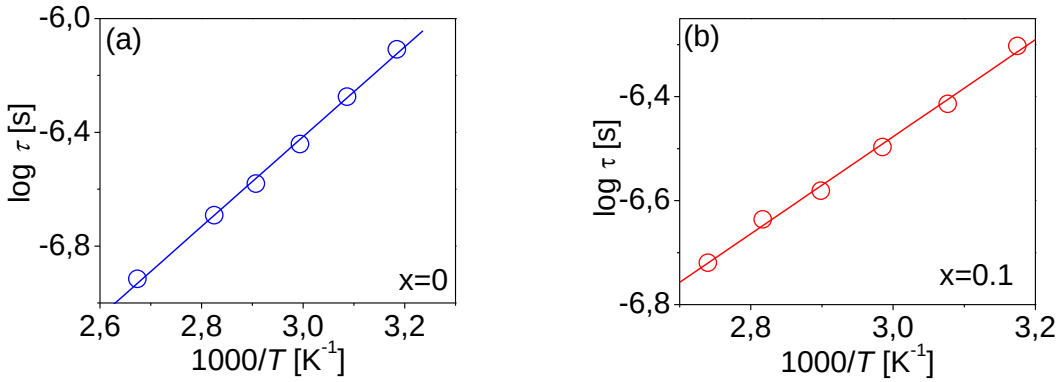

Fig. 3.10. The The log τ vs. 1000/T plot for $TbMnO_3$ (a) and $Tb_{0.9}Al_{0.1}MnO_3$ (b) samples.

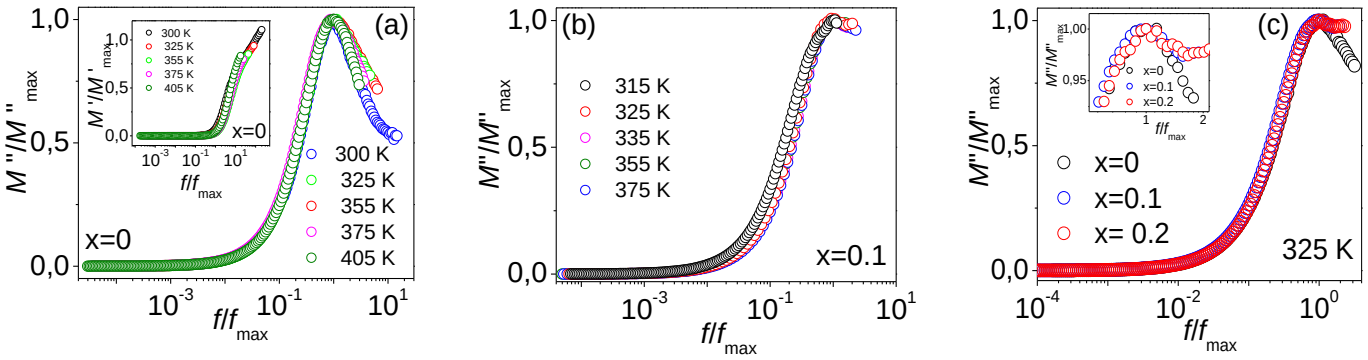

Figure 3.11. Scaled imaginary part of the electric modulus spectra of undoped (a) and Al-doped $TbMnO_3$ samples (b) at various temperatures. Inset to Fig. 3.11(a): scaled real part of the electric modulus of the $TbMnO_3$ sample at several temperatures. (c) Scaling behavior of the imaginary part of the electric modulus into a master curve for $TbMnO_3$ at different Al-concentrations. Inset: master curve of $TbMnO_3$ at different concentrations plotted on an enlarged scale.

As previously stated, it is apparent that the qualitative shape of the modulus curves is temperature-independent [Fig. 3.9(b)]. Hence appropriate scaling could be performed to obtain a master curve that would allow one to gain insight into a possible temperature-independent relaxation mechanism under the modulus formalism. In so doing, the normalized plots of modulus isotherms are plotted versus the frequency scaled by the peak frequency f_m [Fig. 3.11(a)]. Here, M' is scaled by M_∞ and M'' is scaled by M''_{max}. An imperfect overlapping of all curves/peaks on a single master curve, especially at higher frequencies, is verified in Fig. 3.11(a). The lack of coincidence of all curves/peaks of the reduced plots of M''/M''_{max} and M'/M'_∞ versus log (f/f_{max}) on a single master curve at all the temperatures measured suggests that the behavior of the dynamic processes is slightly temperature-dependent. Hence the relaxation process that takes place at various frequencies has slightly different thermal activation energies. Moreover, the imperfect overlapping of the curves at higher frequencies also points to a slightly temperature-dependent stretching coefficient β [37], as described below. At this point, it is important to point out that the representation of the experimental

data as M''/M_{max} versus log (f/f_{max}) allows one to make a direct comparative analysis for each branch of the curves. This, in turn, facilitates easy detection of any type of dispersion phenomenon. Concretely, the scaling of the frequency by the f_{max} parameter gives a distribution of M''/M''_{max} values taking into consideration logarithmic representation of the frequency data around $\log(f/f_{max})=1$. At frequencies above this value, some degree of dispersion can be observed, depending on the Al-doping level and the temperature. It is evident in Fig. 3.11(a) that the normalized modulus plot is non-symmetric. This behavior is in agreement with the non-exponential behavior of the electrical function, well described by the KWW exponential function [39]. The β parameter appearing in the KWW function also gives information about the non-exponential character of the relaxation [38]. In this regard, it has been established that the smaller the value of β, the larger the deviation of the relaxation with respect to the Debye-type model. The value of β can be estimated from the measurements of the electric modulus at various temperatures. In the present study, the electric modulus behavior of all the samples was analyzed by employing the modified KWW function, as suggested by Bergman [46]. In this model, the imaginary part of the electric modulus can be defined as $M''(\omega) = \frac{M''_{max}}{(1-\beta)+\frac{\beta}{1+\beta}\left[\beta\left(\frac{\omega_{max}}{\omega}\right)+\left(\frac{\omega}{\omega_{max}}\right)^{\beta}\right]}$, where M''_{max} is the peak of the $M''(\omega)$ function at the frequency ω_{max}. As an example, the experimental data of the imaginary part of the modulus spectra at various temperatures for the sample with x=0 [Fig. 3.9(b)] were fit according to the above equation, and the results are shown as solid lines in the same plot. It can be readily verified that the experimental data adjust well to this model, except in the high frequency range. The extracted values of β were ~0.7, and they are almost independent of temperature. It was also found that the value of β decreases slightly as the Al content increases in the samples. This indicates that the interaction between the cations

increases with the Al content. As stated above, the β parameter gives the extent to which the mobile charge carriers couple during the conduction processes [47]. In this regard, it has been established that a value of β=1 corresponds to completely uncorrelated charge carrier motion. The value of β~0.7 encountered in the present study for the undoped samples suggests a cooperative motion of the charge carriers. The concept of cooperative motion in the studied system arises from the universal behavior discussed by Jonscher [34]. Within this formalism, a jump of a mobile charge carrier in the compound may not be treated as an isolated event. This means that when the charge carrier jumps from one equilibrium position to another it provokes a time-dependent movement of other charge carriers in its surroundings. This effect then leads to additional relaxation of the applied field. Therefore, the β parameter obtained from the modulus formalism and the frequency exponent parameter *n* obtained from the power law model represent the interaction between the charge carriers [33].

The electric modulus of the 10% Al-doped sample [Fig. 3.11(b)] shows some differences as compared with that of its undoped counterpart [Fig. 3.11(a)]. Although the general trend of the $M''(f)$-curves is similar to that of the undoped samples, the peaks of the doped sample are less defined within the available frequency range. Moreover, the temperature dependence of the $M''(f)$-curves, particularly the shift of the peaks toward higher temperatures, is not as visible as that shown by the undoped samples. These observations show the influence of the Al doping on the conducting and dielectric properties of the parent $TbMnO_3$. Certainly the scaled spectrum of M'' for different Al-concentrations at 325 K does not perfectly overlap on a single master curve, especially at higher frequencies [Fig. 3.11(c)]. The imperfect overlap of the curves on a single master curve implies that the conductivity relaxation is slightly

dependent on the Al doping level. This result is in agreement with the slight difference in the value of the relaxation time obtained for the undoped and 10 % Al-doped samples (Fig. 3.10).

Impedance analysis is commonly employed to separate the different dielectric relaxations caused by the intergrains and electrodes of ceramic materials [29]. The *Z*'' vs. *Z*' plots in Fig. 3.6 clearly show that there is only one type of relaxation behavior at the selected temperatures for both the undoped and the Al-doped samples (there is only one semicircle for each sample at each temperature). The presence of two semicircles (generally observed at low temperatures) in the low- and high-frequency regions indicates that there are two types of relaxation in each frequency region [33]. The two types of relaxation originated from the grain and grain boundaries' Maxwell–Wagner polarization effect (referred to as the internal barrier-layer capacitor [IBLC] low-frequency region) and the electrode-bulk interfacial Maxwell–Wagner polarization (high-frequency region). In our case, it is evident that the difference between the two types of relaxation is not significant at temperatures $T \geq 300$ K. The impedance data of the undoped and 10% Al-doped samples were fit using Zview software.

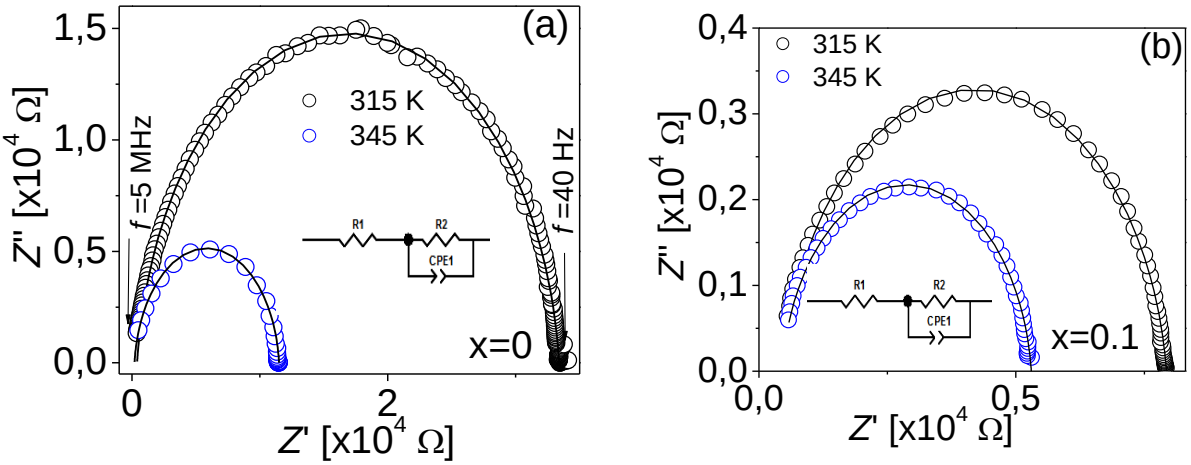

Figure 3.12. Complex impedance plot (Nyquist plot) of undoped (a) and 10% Al-doped $TbMnO_3$ samples (b) at 315 and 345 K. The solid lines represent results of modeling with electrical equivalent circuits [insets to Fig. 3.12].

The fit of the impedance data using equivalent fitting circuits can give valuable information on the direct correlation between the response of a real system and an idealized model circuit composed of discrete components. The best fitting curves (solid lines in Fig. 3.12) were obtained by using an equivalent circuit composed of a resistance R_1 (grain resistance R_g) in series with a parallel combination of a resistance R_2 (grain boundary resistance R_{gb}) and constant phase element impedance (Z_{CPE}). The R_2-CPE unit, representing the intergrains, generates the IBLC effect. The equivalent fitting circuit is shown in the inset of Fig. 3.12. The Z_{CPE} can be written as $Z_{CPE}=1/T(j\omega)^p$ [48], where T (units [Fs^{p-1}] or [Ωs^{-1}]) and p represent the CPE parameter and the CPE exponent ($0 \leq p \leq 1$), respectively. Both T and p are frequency-independent adjustment parameters. In turn, $j = \sqrt{-1}$. It is important to point out that CPE is identical to capacitance when $p = 1$ and to simple resistance when p=0 [49]. When p = 0.5, CPE is identified as Warburg impedance [50]. The impedance can be expressed in terms of a CPE as $Z(\omega)=R_1 +(R_2/(1+TR_2(j\omega)^p)$. Results of the fitting procedure for both studied samples are listed in Table 3.4. Here it can be observed that the general trend of R_1 is to diminish in value as the temperature is increased, which is also consistent with the previous conductance results. In addition, the results shown in Table 3.4 show that the grain boundary resistance R_2 is considerably lower for the Al-doped sample than for the undoped one. Here, it is possible that the grain boundary effect contributes to lowering the barrier to the motion of the charge carriers, paving the way for increased electrical transport with increasing temperature, as corroborated through the conductance measurements (Fig. 3.7)

[27]. Evidence of grain boundary conduction has been observed in ceramic perovskites, ceramic conductors, etc. [40,41].

Table 3.4. Electrical parameters of equivalent electrical circuit obtained from complex impedance spectrum for undoped and Al-doped $TbMnO_3$ samples.

x=0					x=0.1			
T [K]	$R_1=R_g$ (kΩ)	$R_2=R_{gb}$ (kΩ)	T(nF)	p	$R_1=R_g$ (kΩ)	$R_2=R_{gb}$ (kΩ)	T(nF)	p
315	400	33000	8	0.93	480	7450	0.8	0.92
345	200	11300	10	0.94	450	4850	0.8	0.93

It has been proposed that the high values of the dielectric constant observed for $TbMnO_3$ samples at high temperatures and low frequency can predominately be ascribed to the Maxwell–Wagner polarization effect, originating from the interfacial polarization of the oxide/electrode [29]. This relaxation behavior can generate large dielectric loss, as observed in Fig. 3.13. Upon increasing the temperature, the localized carriers become "unfrozen", which favors the dipolar effects. Simultaneously, the "unfreezing" process leads to a large increase in the number of hopping carriers, which greatly decreases the resistance, as confirmed by the temperature dependence of the *dc* resistance (see Fig. 3.4). When the carriers hop to the vicinity of blocking grain boundaries or electrodes and form space charges, the relaxation of the space charges will result in an apparent giant dielectric constant. Due to the lattice distortion generated by the Al-doped $TbMnO_3$, the dielectric constant at 325 K resulted to be slightly larger than that of the undoped one (inset to Fig. 3.5(a)). At low temperatures, there will be lots of space charges between grain boundaries that result in the dielectric relaxation (IBLC effect). With an increase in the temperature, the number of carriers increases, finally generating accumulation on the interface of the oxide/electrode. This, in turn, leads to a gradual increase in the interfacial Maxwell–Wagner polarization,

which to a great extent determines the behavior of the dielectric constant at high temperatures.

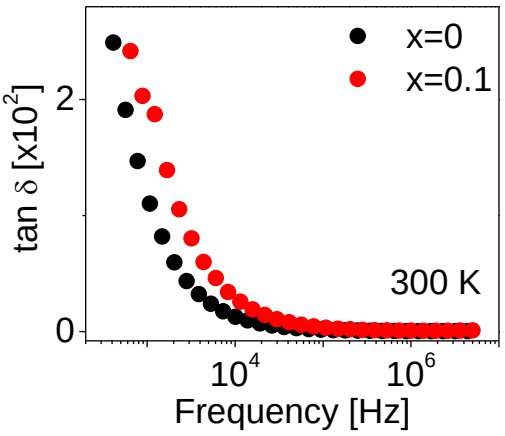

Figure 3.13.Variation of the dielectric loss tanδ at room temperatures for undoped and 10% Al-doped $TbMnO_3$ samples as a function of frequency.

3.1.4. Thermal properties

Although several good thermoelectric materials have been found in both *n*-type and *p*-type conducting oxides so far [51,52], it is still highly required to explore novel high-performance thermoelectric oxides. Although the multiferroic function of $TbMnO_3$ has been carefully studied and reported in several publications, this is not the case with the thermoelectric properties. Since the different magnetic and electric phase transitions strongly couple to lattice degrees of freedom [53], a strong influence of such ordering phenomena (and the related low-lying excitations) on the phonon thermal conductivity can be expected. In this section, results of a experimental study of the thermal conductivity and thermoelectric properties of polycrystalline $Tb_{1-x}A_xMnO_3$ samples are presented. Thermal conductivity measurements were carried out in a physical properties measurement system (PPMS, Quantum Design) with the thermal transport option in the temperature range 1-390 K, using

the continuous scanning mode with a 0.5 K/min cooling rate. Ceramic disks with size of approximately 0.6 mm in diameter and 0.3 in thickness were contacted with silver paste to cernox thermometers heaters and heat sink.

A closer approximation to the nature of the conduction mechanism in $Tb_{1-x}Al_xMnO_3$ multiferroic can be made through thermoelectric power measurements. This versatile and sensitive technique enables one to investigate the scattering mechanism in electronic conduction. The temperature dependence of the Seebeck coefficient of the $Tb_{1-x}Al_xMnO_3$ samples, recorded under cooling cycle, is shown in Fig. 3.14. It is observed that the samples exhibit a quite large room-temperature thermoelectric power response [S(300 K)~350 μV/K], a fact that makes it potentially attractive for thermoelectric applications. Note that S is positive in all the temperature range measured, suggesting that $TbMnO_3$ is p-type semiconductor. The value of the Seebeck coefficient of $TbMnO_3$ decreases with the Al doping. As it is known, the Seebeck coefficient determines the average energy, with respect to the Fermi level E_F, which is transported by charge carriers under the influence of a thermal gradient. In this regard, the Seebeck coefficient can be considered as a direct test of the changes occurring at the Fermi level. In the general case, S is expressed as $S=(\mu-\langle E\rangle)/(|e|xT)$, where μ is the chemical potential and $\langle E\rangle$ is an average energy of the carriers weighted by their contribution to the conductivity [54]. Probably, the Al substitution for Tb induces several changes in the Fermi level of the pristine compound that may stem from considerable changes in the band structure. For instance when S has approximately linear relationship to temperature, this can be expressed as $S=\pi^2k_B^2T/eE_F$ [55]. Hence, the Fermi level increasing with the increase in the doping level will result in a decreasing in the value

of the *S*. This has been reported by other ceramic thermoelectric materials [56]. Without doubt, more theoretical and experimental work should be done to clarify this issue.

It is expected that evidence for polaronic transport in $Tb_{1-x}Al_xMnO_3$ to be also seen in the thermopower measurements. In this regard, it is known that for polaronic transport, the temperature dependent thermopower *S* is given by $S(T)=(k_B/e)(\alpha+E_S/k_BT)$ [17], where *e* is the electron charge, α a sample-dependent constant, which is associated with the spin and the mixing entropy [57], and E_S the activation energy for polaron hopping [17]. The inset to Fig. 3.14 shows a linear variation in the plot of *S* versus $1/T$ in a wide temperature range, suggesting a polaronic transport. The activation energies E_S along with the values of α obtained from the slope of the straight line are listed in Table 3.2. The notable difference between E_ρ and E_S can be explained considering that the activation energy E_ρ derived from resistivity is the total activation energy needed for the creation of the carriers and the activation of the hopping of the carriers. In turn, E_S is just the energy required to activate the hopping of the carriers, as discussed in the polaron model. Moreover, the parameter $\alpha>1$ implies that the transport of the carriers is dominated by the large polaronic conduction.

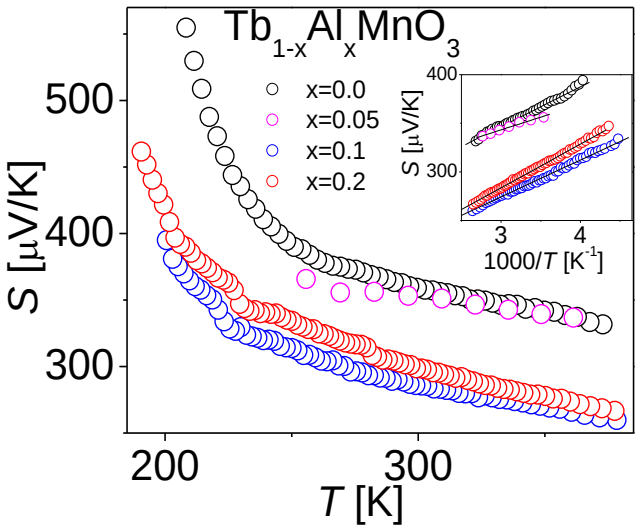

Figure 3.14. Variation of the thermopwer as a function of temperature for polycrystalline $Tb_{1-x}Al_xMnO_3$ samples. Inset: temperature dependence of the thermopower versus $1000/T$ for $Tb_{1-x}Al_xMnO_3$ samples in the temperature range 270-400 K. Linear fits to the polaronic model are represented by lines.

Figure 3.15 shows the temperature dependent zero-field thermal conductivity of polycrystalline $Tb_{1-x}Al_xMnO_3$ samples. Since the results of thermal conductivity provide valuable information about various scattering processes of thermal carriers, the present data would offer an opportunity to probe the interplay between lattice and charge degrees of freedom in this material. First, it is observed that the $\kappa(T)$ values increase with increasing temperature, indicating an usual phonon-mediated scattering mechanism of charge carriers. The total thermal conductivity is then mainly associated with the lattice phonons rather than the charge carriers due to the high electrical resistivity of this perovskite-type material. Indeed, the estimated electronic thermal conductivity (κ_e) contribution from the Wiedemann-Franz law ended up being $3x10^{-6}$ W/mK at room temperature for the pristine sample. This value is much smaller as compare to the total thermal conductivity of $TbMnO_3$ (Fig. 3.15). Consequently, the predominant contribution to the measured κ comes from phonon thermal conductivity (κ_{ph}) with a negligibly small contribution of κ_e. The first interesting aspects of the measured $\kappa(T)$ dependence are related with the disappearance of the low-temperature hump and the magnitude of κ. The absence of a well-defined low-temperature hump is consistent with glass-like conductivity. The glass-like conductivity observed in Fig. 3.15 is typical for complex and highly disordered crystals, in which case the conductivity maximum is largely suppressed and often shifted at higher temperatures, even above room temperature [58, 59]. As to the magnitude of κ, it is noted that the measured values of κ(300 K) are rather small and comparable to those of glassy materials [60]. For typical non-crystalline materials

(bad metals), the magnitude of κ(300 K) lies in the range of 5-65 mW/cmK. For a crystalline solid, such a low value of thermal conductivity can be thought to originate from various disorders present in the lattice, such as random, noncentral distortions of the lattice, etc., resulting in high degree of disorder. Certainly, $\kappa(T)$ displays behavior characteristic of phonon scattering in an amorphous solid ($d\kappa/dT>0$) [60]. Unlike amorphous solids, $d\kappa/dT>0$ observed in the $TbMnO_3$ samples cannot be due to quenched structural disorder but rather to unusually large dynamic lattice distortions accompanying charge transport [61]. The very large anharmonic lattice distortions can be inferred from the Debye-Waller factor [9]. The results encountered for $TbMnO_3$ support the widely accepted assertion that manganites are a unique class of materials from the standpoint of lattice dynamics. Some authors have compared thermal conductivity data of various perovskites manganites [61] and suggested that the mentioned scenario may be attributed to the vibronic interactions of Mn^{3+} (Jahn-Teller) ions, which critically limit the mean free path of phonons.

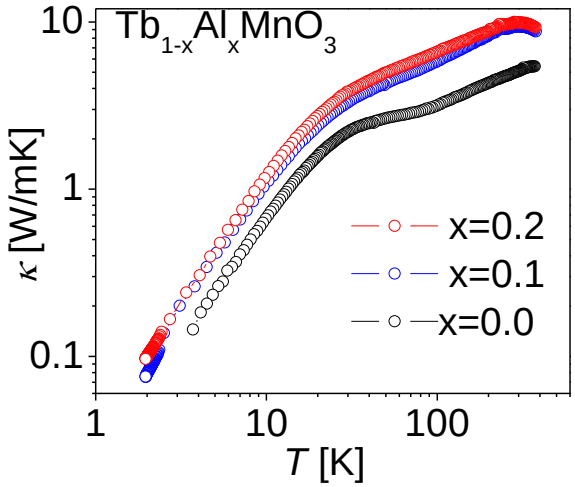

Figure 3.15. Zero-field thermal conductivity, κ, of $Tb_{1-x}Al_xMnO_3$ (x=0,-0.2) recorded in the temperature range 1-390 K.

The results obtained for the thermal conductivity of polycrystalline $TbMnO_3$ are qualitatively in good agreement with those reported for $TbMnO_3$ single crystals measured along the *a* direction [62]. In particular, the slope change at around 90 K (broad minimum in single crystalline samples) seems to be an intrinsic feature of $TbMnO_3$. It is interesting to note that the room-temperature values of κ measured for the polycristalline samples are similar to those reported for $TbMnO_3$ single crystals [63]. Nevertheless, it is observed from Fig. 3.15 that κ continues decreasing below T_{FE} to very low absolute values, which is not observed for $TbMnO_3$ single crystals. For the latter ones, the additional suppression of the thermal conductivity in the low-temperature incommensurate antiferromagnetic phase was attributed to the incommensurability [63]. Certainly, the lowering of the symmetry of the system can provoke additional thermal resistance. Nevertheless, for polycrystalline samples the grain boundary scattering should play an important role. Indeed, it is observed that below a temperature of about 15 K, κ approximately follows a T^n law with $n = 1.5$. This suggests that the low temperature behavior is not dominated by the heat capacity of $TbMnO_3$, which should follow the T^3-Debye law at low temperature. Thus, although the decrease in the value of κ with decreasing temperature is a typical feature for the reduction of thermal scattering in solids at low temperatures, the large difference between the values of the thermal conductivity measured in single crystalline and polycrystalline $TbMnO_3$ should be ascribed to different effects related to the grain boundary scattering. Such grain boundaries would further limit the mean free path of phonons reducing then the thermal conductivity. A remarkable change in the $\kappa(T)$ curve is observed at about 35 K. At this temperature κ reaches a value of about 3 W/Km. For $TbMnO_3$ single crystals a maximum with an absolute value of ~3 W/Km has also been observed at $T \approx 35$ K [63]. By comparing the thermal conductivity

with thermal expansion of single crystals of $TbMnO_3$, it was suggested that suppressed κ of $TbMnO_3$, particularly the broad minimum observed at about 90 K, was caused by a resonant scattering of phonons between different crystal field levels of Tb^{3+} [64]. As stated above, the $TbMnO_3$ samples analyzed in the present work also showed a detectable anomaly at the same temperature. Hence, for the studied samples the origin for an additional scattering channel is probably the resonant scattering between crystal field levels of the 4f shell of Tb^{3+}. The effect of 4f orbitals on the thermal conductivity is known e.g. from rare earth garnets [64], where an additional suppression of κ was observed. In a resonant scattering process, a phonon is absorbed causing a transition between different multiplet levels of a 4f multiplet. The phonon is then reemitted in an arbitrary direction causing additional thermal resistance. Note that the influence of the transition temperatures T_N and T_{FE} on κ is hardly detectable in the measured $\kappa(T)$ dependence of the polycrystalline $TbMnO_3$ samples (this work). Because of the low absolute values of κ, it is plausible that both in single crystals and polycrystals of $TbMnO_3$ the ferroelectric and magnetic transitions at low temperatures play almost no role.

The thermoelectric figure of merit $ZT=S^2\sigma T/\kappa$ of a polycrystalline $TbMnO_3$ sample is presented in Fig. 3.16. Although the rather low thermal conductivity and the relatively large thermopower values for the sample, preconditions for large ZT values, are already fulfilled, the quite low conductivity of $TbMnO_3$ prevents large ZT values. In this regard, it is observed that the values of ZT obtained for the sample with x=0.2 are about one order of magnitude larger than those obtained for the pristine sample. Although these values are certainly too small for technical applications, the results suggest that enhancement of the thermoelectric function of $TbMnO_3$ is possible upon Al doping. Here it should be pointed out that very small values of ZT have also been reported for other perovskite-type manganites [65]. In Ref. [65],

the values obtained for *ZT* are similar to those found for $TbMnO_3$. Thus, the low values of the electrical conductivity observed for various manganites hamper their thermolectric applications.

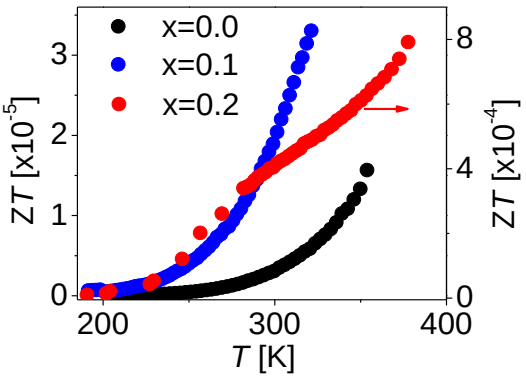

Figure 3.16. Temperature dependence of the dimensionless figure of merit *ZT* for a polycrystalline $TbMnO_3$ sample.

3.1.5. Magnetic properties

As stated in the introduction of this thesis, $TbMnO_3$ is one of the few materials in which the magnetic and electric ordering coexist in a close range of temperatures. This material is one of the representative materials of the so called type II multiferroics in which ferroelectricity is induced by the magnetic ordering. Anomalies in $TbMnO_3$ single crystals have been observed at $T_{N1}\approx41$ K, where the Mn^{3+} magnetic moments have sinusoidal antiferromagnetic (AF) order. At $T_{lock}\approx27$ K electric polarization appears. At $T_{N2}\approx7$ K, where the Tb^{3+} magnetic moments are AF ordered [66]. Studies in more complex compounds like $R_{1-x}A_xMnO_3$ (R=rare earth; A=Ba, Sr, Ca) present a wide variety of magnetic structures and charge ordering [67]. Thus, adding cation is an often-adopted strategy to tailor the physicochemical properties of perovskite-type ceramics. Furthermore, it has been reported that polycrystalline

$TbMnO_3$ doped with elements such as Na in the Tb site produces a shift of the AF ordering of the Tb^{3+} magnetic moments toward high temperatures [68]. Based on these results, it is evident that the exploration of the manner in which the magnetic properties of $TbMnO_3$ are affected by the substitution of Tb or Mn by Al deserves special attention.

In this section, experimental results on the magnetic characterization of polycrystalline $Tb_{1-x}Al_xMnO_3$ (x=0, 0.05, 0.07, 0.1, and 0.3) samples synthesized by means of standard solid state reaction are reported. It is apparent that the Al-doping enhance the ferromagnetic behavior of the $TbMnO_3$ pellets, improving the magnetic performance of this material.

The temperature dependence of the magnetization, *M*(T), recorded in zero field cooling mode (ZFC) for $Tb_{1-x}Al_xMnO_3$ samples with composition x=0, 0.1, 0.2, 0.3 is shown in Fig. 3.17. The huge increase in the magnetization observed for the doped samples suggests that drastic changes are generated in the magnetic properties of the parent $TbMnO_3$ by varying the aluminum content. Indeed, it is apparent that doping levels as low as 5 % (x=0.05) already change the magnetic order from antiferromagnetic to weak ferromagnetic. Note that the ferromagnetic correlation increases as the Al content does in the $Tb_{1-x}Al_xMnO_3$ samples. Although the observed effect should carefully be analyzed, the *M*(*T*)-curve in Fig. 3.17(a) clearly shows that remarkable changes in the magnetic response of $TbMnO_3$ are induced by the substitution of Tb by Al ions. The Curie temperature (T_C) for the three compositions is close to 50 K. Moreover, the heavier the Al doping (x=0.3), the greater the increase in the magnetization. Certainly, for the sample with x=0.3, the magnetization increases up to one order of magnitude. This behavior is different to that reported in Ref. [4]. There, $Tb_{1-x}Al_xMnO_3$ samples with Al concentrations larger than 0.1 showed a peak in the magnetization at about 33 K. This behavior was explained by the authors assuming that the crystalline

structure presents canted spins [5]. The reciprocal magnetic susceptibility [$\chi^{-1}=H/M=(T-\Theta_{CW})/C$] of the samples with x=0.2, and 0.3 features a Curie–Weiss behavior at temperatures above ~50 K [Fig. 3.17(b)], whereas the parent $TbMnO_3$ followed the Curie-Weiss law down to the lowest temperature reached as a consequence of the ordering of Mn magnetic moments [3]. The fit to the experimental data of the undoped sample is also displayed in the Fig. 3.17(b). From the slope of the fitted straight line, the Curie-Weiss temperatures, Θ_{CW}, was obtained (~-40 K). The negative value obtained for Θ_{CW} point out to a dominant antiferromagnetic character of the exchange interactions between Mn ions. In turn, magnetization measurements as function of applied magnetic field at 5 K for $Tb_{(1-x)}Al_xMnO_3$ samples with x=0, 0.2, and 0.3 are shown in Fig. 3.18. By comparing the results obtained for the pristine sample and the Al-doped sample, it is evident that the Al-doping leads to ferromagnetic ordering as suggested by the magnetic hysteresis loop.

Although the appearing of weak ferromagnetism in Al-doped $TbMnO_3$ was explained in terms of canted spins [5], the effect is certainly not trivial and should be analyzed within a more precise framework. From start, it is evident that a plausible approach of modifying the magnetism in $TbMnO_3$ is the substitution of Tb^{3+} or Mn^{3+} by Al^{3+} ions, which may provoke a local disturbance of the lattice around the Al^{3+} ions to relax the strain produced by a size mismatch [5]. Thus, the size of the Al^{3+} ion disturbs the orbital order of some of its neighbors. The change in the orbital order, in turn, disturbs the magnetic order. The substitution is certainly isovalent but there is a 48 and 17 % difference in ionic size of Tb^{3+}, Mn^{3+} and Al^{3+} (0.535, 0.645, and 1.04 Å for Al^{3+}, Mn^{3+} and Tb^{3+}, respectively). Hence, it is certainly more reasonable to expect substitution of Mn^{3+} ions with an Al^{3+} ions instead of substitution of Al^{3+} for Tb^{3+}. Nevertheless, there have been some efforts to substitute Al ions at both the

Tb^{3+} and Mn^{3+} sites in $TbMnO_3$ [6,13]. Indeed, interesting and novel phenomena can occur if the distortion of the $TbMnO_3$ structure is tuned by increasing/reducing the chemical pressure at the Tb^{3+} position. As previously stated, the isovalent substitution of the large Tb^{3+} ion with the smaller Al^{3+} ion would result in a local disturbance of the lattice around the Al^{3+} ions in order to relax the strain produced by size mismatch. As a result, the values of the lattice parameters will decrease and the unit cell will shrink. Thus, the decrease in cell volume upon Al doping is caused by the size effect. The increase in the phonon frequencies observed in the Raman spectrum of the $Tb_{0.9}Al_{0.1}MnO_3$ sample is in accordance with the general trend observed in the Raman spectra of the $RMnO_3$ series with decreasing R^{3+} ion radius [69]. It is expect that partial replacement of Tb^{3+} with a smaller trivalent ion (X) in Tb-X-Mn-O could significantly alter the bond lengths and the bond angles and hence the magnetic interactions between two adjacent Mn-O layers which, in turn, could influence the magnetic behavior. In general, the stability of the perovskite structure of a compound ABO_3 is defined by the tolerance factor t which should be close to the unit. The factor t has already definied as $t=(r_A+r_O)/[\sqrt{2}(r_B+r_O)]$, where r_A, r_B, and r_O are the ionic radii of A, B and oxygen, respectively [70]. By geometry, the ideal cubic perovskite structure will have $t=1$, where regular BO_6 octahedra share comers of the cubic unit cell to form a threedimensional array with the A ions (at body centered sites) occupying the volume between these octahedra. However, when A is not large enough, the structure becomes distorted as the BO_6 octahedra tilt and rotate in order to fill the extra space around A, to optimize the A-O bond length [71]. An orthorhombically distorted perovskite structure is observed in the case of $TbMnO_3$. The buckling of the MnO_6 octahedron causes the Mn-O-Mn bond angle θ to become less than its ideal value of 180°. The Mn-O-Mn bond angle signifies the extent of Mn (e_g) and O (2p)

orbital overlap and hence plays an important role in determining the electronic bandwidth and the magnetic exchange interaction [72]. Thus, the tilting angle of the MnO_6 octahedra depends on the ionic radii of the R^{3+}. When these are decreased by replacing R^{3+} with another isovalent rare–earth ion with a smaller ionic radius, the Mn–O–Mn bond angle also further decreases, which is equivalent to an increase of the MnO_6 tilting. Therefore, the disturbance of the orthorhombic perovskite structure of $RMnO_3$ by means of Al-doping can influence the Mn–O–Mn bond angle and thus the Mn–Mn exchange. This, in turn, can results in decreasing of the T_N and corresponding transformation of the complex magnetic structures with simultaneous contribution of the Tb and Mn magnetic moments [73]. In other words, the variation of the interatomic distances can change the delicate energy balance of magnetic interactions, which depend on these distances in different ways [74]. In addition, it is known that the effect of the R ions is their direct (para)magnetic contribution at low temperatures which results in a significant anisotropy of magnetic properties as recently observed in $PrMnO_3$ and $NdMnO_3$ [75]. Certainly, the presence of the magnetic rare-earth subsystem significantly affects the stability of various magnetic configurations owing to the anisotropic exchange interaction with the Mn^{3+} ions (for instance, there are three purely antiferromagnetic structures with the 120° spin configurations in the *z* layers). The dilution of the rare-earth subsystem in $Tb_{1-x}Al_xMnO_3$ apparently promotes a decrease in the anisotropy energy, which determines the observed smooth character of the transition to the weakly ferromagnetic state. Thus, the observed transition to the weakly ferromagnetic phase in $Tb_{1-x}Al_xMnO_3$ can be attributed to the energy gain appearing because the magnetic moments of Tb^{3+} ions located at nonequivalent crystallographic positions 4*b* and 2*a* are polarized along the *c* axis [76].

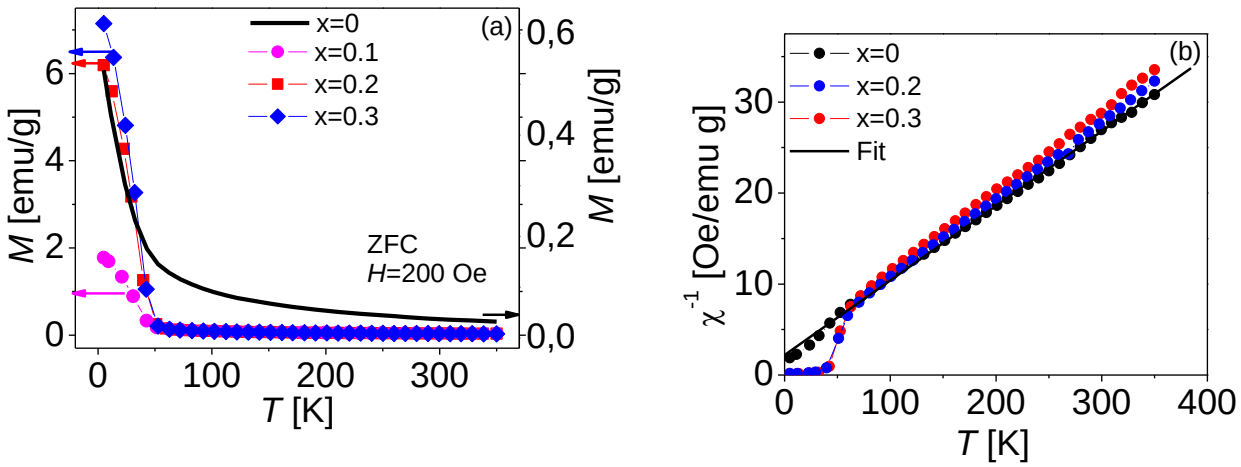

Figure 3.17. (a) Temperature dependence of the magnetization, *M*(T), in zero field cooling mode (ZFC) for $Tb_{1-x}Al_xMnO_3$ polycrystalline samples with compositions; x = 0, 0.1, 0.2, and 0.3. (b) FC temperature dependence of the reciprocal susceptibility (χ^{-1}) of the $Tb_{1-x}Al_xMnO_3$ polycrystalline samples obtained from magnetic measurements in a magnetic field of 200 Oe.

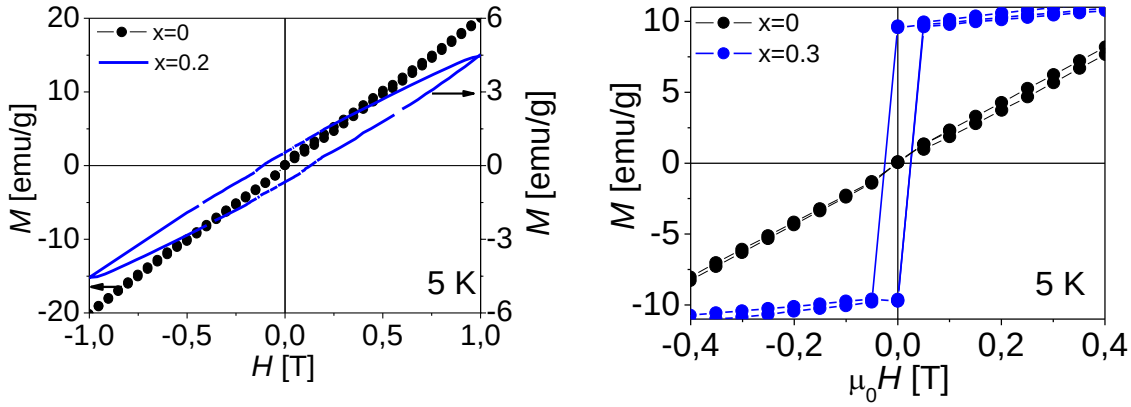

Figure 3.18. Magnetization as a function of magnetic field recorded at 5 K, for $Tb_{1-x}Al_xMnO_3$ samples with x=0, 0.2 and x=0.3.

From the previous discussion it is apparent that the local distortion drives the orbital order and the orbital order drives the magnetism. In the literature, there are some reports on the effect of the substitution of Mn^{3+} by Al^{3+} on the magnetoelectrical properties of $TbMnO_3$ single-crystals [5]. It is evidenced that although the substitution is isovalent, the difference in the ionic size of Mn^{3+} and Al^{3+} (~ 17 %) may also lead to a local disturbance of the lattice

around the Al^{3+} ions to relax the strain produced by the size mismatch. In the case of polycrystalline $TbMn_{1-x}Al_xO_3$ samples ($x \leq 0.1$), it was verified that the contraction was mainly produced by the *b* axis shrinking ($\Delta b = -0.48$ Å/x) [5]. A small reduction in the value of *a* axis ($\Delta a = -0.09$ Å/x) was also reported for the same concentration range [5]. Moreover, the reduction of the orthorhombic distortion in the *ab* plane has been ascribed to the partial replacement of strongly distorted MnO_6 octahedra (Jahn-Teller-like) by the regular AlO_6 ones [16]. By using powerful characterization techniques such as neutron diffraction, it was argued that the dilution of magnetic ions (Mn^{3+} by Al^{3+}) leads to weakening of the superexchange Mn-O-Mn interaction [5]. As a consequence the transition temperature T_{N1} shifted to lower temperatures by increasing the Al-doping level. In an interesting study, substitution of Mn with a nonmagnetic ions has been carried out in order to test the role of the $J_{Mn\text{-}Tb}$ interaction [17]. It was shown that the Mn magnetic ordering vanished for $x \sim 0.3$, which is well above the percolation limit for a metal with octahedral coordination. It was also reported that small substitutions of Mn^{3+} have little effect on the magnetoelectric properties of the Mn sublattice but can strongly affect the magnetic ordering of Tb moments [17]. The authors suggested that such an ordering comes from the competition between $J_{Mn\text{-}Tb}$ and the direct coupling between Tb moments, $J_{Tb\text{-}Tb}$. A deeper insight into the mechanism leading to the appearance of ferromagnetism in Al-doped can be gained if one start from the basic knowledge on the physiochemical properties of the $TbMnO_3$ system. Stoichiometric $TbMnO_3$ is an insulator whose A-type antiferromagnetic structure at low temperature is mainly connected to the Jahn-Teller distortion of the MnO_6 octahedra. The Jahn–Teller distortions around a manganese ion depend on the local coordinates of the neighbouring oxygen ions, each of which is shared with another Mn ion in the parent structure [77].

Certainly, in manganite compounds with perovskite structure, the manganese ion is surrounded by six oxygen ions. This octahedral environment lifts the degeneracy of the *d* orbitals into three low energy t_{2g} orbitals and two high energy e_g orbitals. In $TbMnO_3$, the MnO_6 octahedra are additionally distorted by the Jahn-Teller effect. This effect is related to the fact that Mn^{3+} is a d^4 high spin ion. Therefore, the system can reduce its energy if the degeneracy of the e_g levels is lifted. This is achieved by decreasing the symmetry of the octahedral, i.e., in $TbMnO_3$, the regular MnO_6 octahedra are deformed into elongated octahedra. Thus, the Jahn–Teller interaction of the e_g states in $TbMnO_3$ causes the Mn ions to have two long, 2.18 Å, and two short bonds, 1.90 Å, to neighboring oxygen ions in the x–y plane. These are arranged such that each oxygen in the *x–y* plane is farther from one Mn^{3+} and closer to the other. In the x–y plane, each line of ions Mn–O–Mn has one long Mn–O bond and one short bond. This arrangement of long and short Mn-O bonds, which occurs below T_{JT} (Jahn-Teller transition temperature) is called a cooperative Jahn-Teller effect. This structural feature leads to orbital ordering (OO) because the occupied e_g orbitals are along the longest Mn-O bonds. A large amount of experimental data has shown that the three-dimensional manganese oxygen network (made up of corner-sharing MnO_6 octahedra) is probably a key feature of the physics of manganites [78]. The magnetic structure of $TbMnO_3$ is the result of the superexchange (SE) interactions between the Mn^{3+} ions in the orbitally ordered manganese-oxygen network. In order to ascertain the relative importance of removing a Jahn–Teller active ion and doping with mobile carriers, the parent compound $TbMnO_3$ should be diluted with non-magnetic non-Jahn–Teller active ions such as Ga^{3+}, Sc^{3+} or Al^{3+} [79]. These elements preserve the valence of the Mn at 3+ and all the compounds are insulating. In an interesting work by Goodenough *et al.* [80], the relationship between the static Jahn–Teller distortion of the MnO_6 octahedron and the orthorhombic distortion of the

unit cell thatwas demonstrated. The replacement of Mn^{3+} by Al^{3+} reduces both distortions, which is coupled with the appearing of spontaneous magnetization [81]. Several explanations have successively been given to account for these properties. For instance it has been suggested that ferromagnetic interactions isare related to a change from static Jahn–Teller ordering to a cooperative dynamic Jahn–Teller ordering. Such change is favored by diluting Mn^{3+} by a nonmagnetic ion (Ga^{3+}, Sc^{3+} or Al^{3+}) in the unit cell. Therefore, the dynamic cooperative Jahn–Teller deformations would induce an isotropic ferromagnetic interaction [81].

In oxides with a perovskite-like structure, two orthorhombic phases can be distinguished according to the lattice parameters [82]. One is the so-called O′ phase with $c/\sqrt{2}>a>b$ that appears for $x<0.5$. The samples analyzed in the present thesis are included within this range. The other orthorhombic structure is a pseudocubic phase with $a>b\approx c/\sqrt{2}$ for $x>0.6$. The O′-phase is related to a cooperative deformation of the MnO_6 octahedra. Although there is least lattice distortion for Al^{3+}, it is expected that the doping affect strongly the physicochemical properties of the parent $TMnO_3$, even if it does not induce double exchange interactions since Al^{3+} is isovalent to Mn^{3+}. It has been verified that as x increases, both the crystallographic distortions disappear and the A-type antiferromagnetism is rapidly suppressed as the material becomes a ferromagnet [77]. In other words, the orthorhombic distortion decreases as the content of Mn increases. The substitution of non-magnetic Al^{3+} ions on the manganese site interferes with the superexchange interactions present in the $TbMnO_3$ parent compounds and disrupts the orbital and spin orderings of the manganese ions. This, in turn, has a strong influence on the physicochemical properties of the parent compound. Similar to other magnanites with different rare-earth elements and doped in the Mn site with non-magnetic

ions, the $TbMn_{1-x}Al_xO_3$ samples could be classified into three groups according to their magnetic structures. For doping levels x<0.4, the magnetic ground state evolves from the AFM of A-type to a canted FM structure. Samples with x=0.5 and 0.6 have a FM ground state whereas samples with x=0.8 and 0.9 do not develop long-range magnetic ordering [83]. As already mentioned, the crystal structure of these samples is the orthorhombic O′ in a wide temperature range. the presence of magnetic peaks characteristics of the A-type structure together with a FM contribution have been clearly corroborated in $LaMn_{1-x}Ga_xO_3$ (0.15<x<0.4) samples by neutron thermodiffractograms patterns [83]. The FM contribuition was explained involing the presence of an AFM canted structure in the considered doping range. The canted structure implies that the AFM component lies in the y-axis while the FM component lies in the *z*-axis. Therefore, the resulting magnetic moments are along the direction [0yz] and [0-yz] in consecutive layers (*z*-direction). Interestingly, the canted structure in $LaMn_{1-x}Ga_xO_3$ (0.15<x<0.4) samples was observed below T_N=60 K, which is consistent with the magnetic measurements on the $TbMn_{1-x}Al_xO_3$ samples. The evolution from an AFM state into a canted FM state was predicted in the past [84] for mixed valence manganites and it was observed in some of them [85]. The results presented in this section show that such kind of canted structures are also possible in systems without formal Mn^{4+}. Note that $TbMn_{1-x}Al_xO_3$ samples with x=0.05 and 0.1 (fig. 3.19) the remanence increases with increasing the Al^{3+} content, while there is no significant changes for the coercive field. These features suggest a canting of the AF ordering [83].

The ZFC and FC $M(T)$ curves of $TbMn_{0.95}Al_{0.05}O_3$ and $TbMn_{0.9}Al_{0.1}O_3$ polycrystalline samples, recorded in a field of 200 Oe, are shown in Fig. 3.19(a) and Fig. 3.19(b). The magnetization increases abruptly at temperatures T<~50K, which is consistent with the

results obtained for the $TbMnO_3$ samples doped in the Tb site. A peak can be appreciated on ZFC curve at around 42 K and at the same temperature both branches separate leading to irreversibility. It is important to note that the magnitude of the magnetization obtained for the $TbMn_{0.9}Al_{0.1}O_3$ sample is lower than that obtained for the $Tb_{0.9}Al_{0.1}MnO_3$ counterpart [Fig. 3.17(a)]. Thus, it is apparent that the ferromagnetism is stronger when Al^{3+} occupies the Tb sites than when it occupies the Mn sites. This effect is probably linked to the fact that when Al^{3+} occupies the Tb sites the chemical pressure in the environment is larger than that generated around the Mn when it is replaced by Al^{3+}. This is a consequence of the larger difference in the ionic radii of Tb and Al. Thus, the strong disturbance of the orbital order of some neighbors can increase the canting angle of the antiferromagnetic structure, which would be responsible for the strong ferromagnetic component. The respective $M(H)$ dependence for the $TbMn_{0.9}Al_{0.1}O_3$ sample, recorded at 5 K, is plotted in Fig. 3.19(c). A clear hysteresis magnetic is also observed for this sample confirming the existence of a ferromagnetic component in the compound.

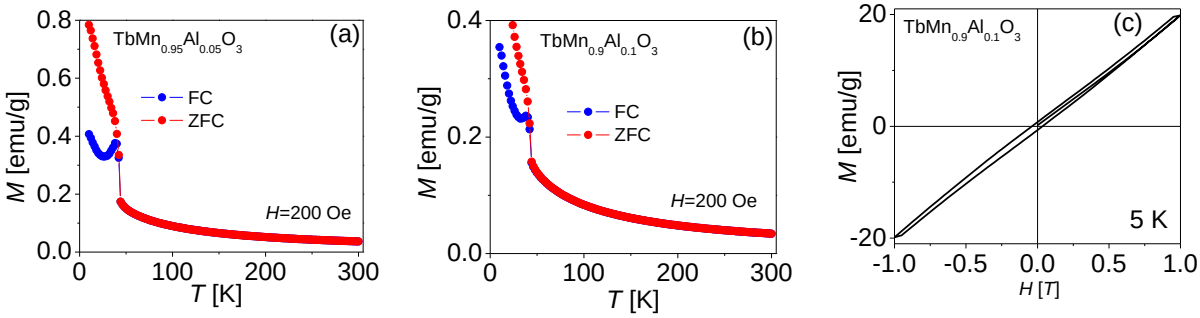

Figure 3.19. ZFC and FC magnetization as a function of the temperature for $TbMn_{0.95}Al_{0.05}O_3$ (a) and $TbMn_{0.9}Al_{0.1}O_3$ (b) polycrystalline samples. (c) Dependence of the magnetization on the magnetic field for $TbMn_{0.9}Al_{0.1}O_3$ recorded at 5 K.

By summarizing, one could say that it is apparent that the structural and magnetic data for $TbMn_{1-x}Al_xO_3$ may be fitted at least qualitatively from the assumption that the size of the

Al^{3+} ion disturbs the orbital order of some of its neighbors. The change in the orbital order, in turn, disturbs the magnetic order. Probably the undertaken analysis has consequences for the understanding of other manganites because it is a case study of a scenario where the local distortion drives the orbital order and the orbital order drives the magnetism. This question is actively debated in other materials where the lattice contribution has been measured directly [86].

References

[1] H. Y. Hwang, S-W. Cheong, P. G. Radaelli, M. Marezio, and B. Batlogg, Lattice Effects on the Magnetoresistance in Doped $LaMnO_3$, Phys. Rev. Lett. **75** (1995) 914.

[2] L. M. Rodriguez-Martinez and J. P. Attfield, Cation disorder and size effects in magnetoresistive manganese oxide perovskites, Phys. Rev. B **54** (1996) R15622.

[3] J. Blasco, C. Ritter, J. Garcia, J. de Teresa, J. Perez-Cacho, M. Ibarra, Structural and magnetic study of $Tb_{1-x}Ca_xMnO_3$ perovskites, Phys. Rev. B **62** (9) (2000) 5609.

[4] F. Pérez, J. Heiras, R. Escudero, Magnetic properties of multiferroic $TbMnO_3$ doped with Al, Physica Status Solidi (c) **4** (2007) 4049.

[5] V. Cuartero, J. Blasco, J. Rodríguez-Velamazan, J. García, G. Subías, C. Ritter, J. Stankiewicz, and L. Canadillas-Delgado, Effects of Al substitution on the multiferroic properties of $TbMnO_3$ Phys. Rev. B **86** (2012) 104413.

[6] T. Kimura, T. Goto, H. Shitani, K. Ishizaka, T. Arima, and Y. Tokura, Magnetic control of ferroelectric polarization, Nature **426** (2003) 55.

[7] M. Pekała, V. Drozd, J.F. Fagnard, Ph. Vanderbemden, M. Ausloos, Magneto transport characterization of the Sn-doped $TbMnO_3$ manganites, J. Alloys and Compounds **467** (2009) 35.

[8] J-T Han, Y-H. Huang, W. Huang, and J. B. Goodenough, Selective Synthesis of $TbMn_2O_5$ Nanorods and $TbMnO_3$ Micron Crystals, J. Am. Chem. Soc. **128** (2006) 14454

[9] D. Varshney, I. Mansuri, N. Kaurav, W.Q. Lung, Y.K. Kuo, Influence of Ce doping on electrical and thermal properties of $La_{0.7-x}Ce_xCa_{0.3}MnO_3$ ($0.0 \leq x \leq 0.7$) manganites, J. Magn. Mag. Mater. **324** (2012) 3276.

[10] R.D. Shannon, Revised Effective Ionic Radii and Systematic Studies of Interatomic Distances in Halides and Chaleogenides, Acta Crystallogr. Sect. A Cryst. Phys. Diffr. Theor. Gen. Crystallogr. **32** (1976) 751.

[11] L. Martin-Carrión, A.D. Andrés, M.J. Martínez-Lope, M.T. Casais, and J.A. Alonso, Phys. Rev. B **66** (2002) 174303.

[12] A. Chaturvedi, V. Sathe, Thin Sol. Films, **548** (2013) 75.

[13] M. N. Iliev, M. V. Abrashev, J. Laverdiere, S. Jandl, M. M. Gospodinov, Y.-Q. Wa ng, and Y.-Y. Sun, Phys. Rev. B **73** (2006) 064302.

[14] M. Staruch, P.h.D. thesis, University of Connecticut, 2013.

[15] S. Issing, P.h.D. thesis, University Würzburg, 2011.

[16] A. Kumar, P. Shahi, S. Kumar, K.K. Shukla, R. Kr. Singh, A.K. Ghosh, A.K. Nigam, and S. Chatterjee, J. Phys. D: Appl. Phys. **46** (2013) 125001.

[17] C.H. Sun, H.S. Yang, Y.S. Chai, J. Liu, H.X. Gao, L. Cheng, J.B. Wang, L.Z. Cao, The transport properties in $Nd_{0.75}Sr_{1.25}CoO_4$ film: Evidence for polaronic transport, J. Phys. Chem. Sol. **70** (2009) 286.

[18] N. Thirumurugan, C.S. Sundar, A. Bharathi, Polaronic transport in the ferromagnetic phase of $Gd_{1-x}Ca_xBaCo_2O_{5.53}$, Solid State Comm. **151** (2011) 1511.

[19] A. Astudillo, J. Izquierdo, F.J. Bonilla, G. Bolaños, and O. Morán, Emergence of Ferromagnetism in $TbMnO_3$ Bulk by Al-Doping, IEEE Trans. Mag. **49** (2013) 4590.

[20] K.L. Nagai, C. León, Phys. Rev. B **60** (1999) 9396.

[21] F. Schrettle, P. Lunkenheimer, J. Hemberger, V.Yu. Ivanov, A.A. Mukhin, A.M. Balbashov, and A. Loidl, Phys. Rev. Lett. **102**. (2009) 207208.

[22] L.G.D. Silveira, G.S. Dias, L.F. Cotica, J.A. Eiras, D. Garcia, J.A. Sampaio, F. Yokaichiya, I.A. Santos, Charge carriers and small polaron migration as the origin of intrinsic dielectric anomalies in multiferroic $TbMnO_3$ polycrystals, J. Phys.:Condens. Matter **25** (2013) 475401.

[23] Mohamad M. Ahmad, Yousef El Sayed, Moustafa El Sayed, Dielectric properties of the ternary $TeO_2/Nb_2O_5/ZnO$ glasses, Physica B **371** (2006) 74.

[24] V. Lyahovitskaya, I. Zon, Y. Feldman, S.R. Cohen, A.K. Tagantsev, I. Lubomirsky, Pyroelectricity in highly stressed quasi-amorphous thin films, Adv. Mater. **15** (2003) 1826.

[25] T. Goto, T. Kimura, G. Lawes, A.P. Ramirez, Y. Tokura, Ferroelectricity and giant magnetocapacitance in perovskite rare-earth manganites, Phys. Rev. Lett. **92** (2004) 257201.
[26] N.F. Mott, Metal–Insulator Transitions, 2nd ed., TaylorandFrancis, London, 1990.
[27] C.C. Wang, Y. M. Cui, L. W. Zhang, Dielectric properties of $TbMnO_3$ ceramics, Appl. Phys. Lett. **90** (2007) 012904.
[28] J.B. Wu, C.W. Nan, Y.H. Lin, Y. Deng, Giant dielectric permittivity observed in Li and Ti doped NiO, Phys. Rev. Lett. **89** (2002) 217601.
[29] Y. Zhang, T. Tong, W. Kinsman, P. Jiang, G. Yin, S. Li, Dielectric and impedance analysis of La doped-$TbMnO_3$, J. Alloys Compd. **549** (2013) 358.
[30] Y.M. Cui, L.W. Liu, G.L. Xie, R.M. Wang, Magnetic and transport and dielectric properties of polycrystalline $TbMnO_3$, Solid State Commun. **138** (2006) 481.
[31] C.C. Wang, Y.M. Cui, G.L. Xie, C.P. Chen, L.W. Zhang, Phase separation in La_2CuO_{4+y} ceramics probed by dielectric measurements, Phys. Rev. B **72** (2005) 064513.
[32] A. Pimenov, A.A. Mukhin, V. Yu., V.D. Ivanov, A.M. Travkin, Balbashov, A. Loidl, Possible evidence for electromagnons in multiferroic manganites, Nat. Phys. **2** (2006) 97.
[33] A.M. Al-syadi, E. Yousef, M.M. El-Desoky, M.S. Al-Assiri, Impedance spectroscopy of V_2O_5–Bi_2O_3–$BaTiO_3$ glass-ceramics, Solid State Sci. **26** (2013) 72.
[34] A.K. Jonscher, Dielectric Relaxation in Solids, Chelsea Dielectrics Press, London, 1983.
[35] K. Funke, Jump relaxation in solid electrolytes, Prog. Solid State Chem. **22** (1993) 111.
[36] D.P. Almond, A.R. West, R.J. Grant, Temperature dependence of the a.c. conductivity of Naβ-alumina, Solid State Commun. **44** (1982) 1277.
[37] M. Sindhu, N. Ahlawat, S. Sanghi, A. Agarwal, R. Dahiya, N. Ahlawat, Rietveld refinement and impedance spectroscopy of calcium titanate, Curr. Appl. Phys. **12** (2012) 1429.
[38] C. Leon, P. Lunkenheimer, K.L. Ngai, Test of universal scaling of *ac* conductivity in ionic conductors, Phys. Rev. B **64** (2001) 184304.
[39] G. Williams, D.C. Watts, Non-symmetrical dielectric relaxation behavior arising from a simple empirical decay function, Trans. Faraday Soc. **66** (1970) 80.
[40] B.V.R. Chowdari, R. Gopalakrishnan, AC conductivity analysis of glassy silver iodomolybdate system, Solid State Ion. **23** (1987) 225.

[41] J.M. Reau, S. Rossignol, B. Tanguy, J.M. Rojo, P. Herrero, R.M. Rojas, J. Sanz, Conductivity relaxation parameters of some Ag^+ conducting tellurite glasses containing AgI orthe $(AgI)_{0.75}(TlI)_{0.25}$ eutectic mixture, Solid. State Ion.**74** (1994) 65.

[42] T. Maxisch, F. Zhou, G. Ceder, Ab initio study of the migration of small polarons in olivine Li_xFePO_4 and their association with lithium ions and vacancies, Phys. Rev. B **73** (2006) 104301.

[43] S.R. Elliot, AC conduction in amorphous chalcogenide and pnictide semiconductors, Adv. Phys. **36** (1987) 135.

[44] T. Srikumar, C.h. Srinvasa Rao, Y. Gandhi, N. Venkatramaiah, V. Ravikumar, N. Veeraiah, Microstructural, dielectric and spectroscopic properties of $Li_2O–Nb_2O_5–ZrO_2–SiO_2$ glass system crystallized with V2O5, J. Phys. Chem. Solids **72** (2011) 190.

[45] I.W. Kim, C.W. Ahn, J.S. Kim, J.S. Bae, B.C. Choi, J.H. Jheong, J.S. Lee, Low-frequency dielectric relaxation and ac conduction of $SrBi_2Ta_2O_9$ thin film grown by pulsed laser deposition, Appl. Phys. Lett. **80** (2002) 4006.

[46] R. Bergman, General susceptibility functions for relaxations in disordered systems, J. Appl. Phys. **88** (2000) 1356.

[47] K.L. Ngai, J.N. Mundy, H. Jain, G. Balzer-Jollenbeck, O. Kanert, Correlation between the activation enthalpy and Kohlrausch exponent for ionic conductivity in alkali aluminogermanate glasses, Phys. Rev. B **39** (1989) 6169.

[48] B. Hirschorn, M.E. Orazema, B. Tribollet, V. Vivier, I. Frateur, M. Musiani, Determination of effective capacitance and film thickness from constant-phase-element parameters, Electrochim. Acta **55** (2010) 6218.

[49] P. Zoltowski, On the electrical capacitance of interfaces revealing constant phase element behavior, J. Electroanal. Chem. **443** (1998) 149.

[50] Z. Stoynov, D. Vladikova, Differential Impedance Analysis, Marin Drinov Academic Publishing House, Sofia, 2005.

[51] N. Wang, H. He, Y. Ba, C. Wan, K. Koumoto, Thermoelectric properties of Nb-doped $SrTiO_3$ ceramics enhanced by potassium titanate nanowires addition, J. Ceram. Soc. Jpn. **118** (2010) 1098.

[52] M. Ohtaki, T. Tsubota, K. Eguchi, H. Arai, Hightemperature thermoelectric properties of $(Zn_{1-x}Al_x)O$, J. Appl. Phys. **79** (1996) 1816.

[53] D. Meier, N. Aliouane, D. N. Argyriou, J. A. Mydosh, and T. Lorenz, New features in the phase diagram of $TbMnO_3$, New J. Phys. **9** (2007)100.

[54] J. Androulakis, Pantelis Migiakis, and J. Giapintzakis, $La_{0.95}Sr_{0.05}CoO_3$*:* An efficient room-temperature thermoelectric oxide, Appl. Phys. Lett. **84** (2004) 1099.

[55] D. Li, X.Y. Qin, J. Liu, H.S. Yang, Electrical resistivity and thermopower of intercalation compounds Bi_xTiS_2, Phys. Lett. A **328** (2004) 493.

[56] H.C. Wang, C.L. Wang,W.B. Su, J. Liu, H. Peng, J.L. Zhang, M.L. Zhao, J.C. Li, N. Yin, L.M. Mei, Substitution effect on the thermoelectric properties of reduced Nb-doped $Sr_{0.95}La_{0.05}TiO_3$ ceramics, J. Alloys and Compounds **486** (2009) 693.

[57] M. Jaime, M.B. Salamon, High-temperature thermopower in $La_{2/3}Ca_{1/3}MnO_3$ films: Evidence for polaronic transport, Phys. Rev. B **54** (1996) 11914.

[58] K. Kato, M. Yamamoto, S. Ohta, H. Muta, K. Kurosaki, S. Yamanaka, H. Iwasaki, H. Ohta, and K. Koumoto, The effect of Eu substitution on thermoelectric properties of $SrTi_{0.8}Nb_{0.2}O_3$. J. Appl Phys. **102 (**2007)116107.

[59] P.A. Popov, V.D. Solomennik, E.E. Lomonova, M.A. Borik, V.A. Myzina, Thermal conductivity of single-crystal ZrO_2-Y_2O_3 solid solutions in the temperature range 50-300 K, Phys. Solid State **54 (**2012) 658.

[60] R. Berman, *Thermal Conduction in Solids*, Clarendon, Oxford, 1976, p. 105.

[61] D.W. Visser, A.P. Ramirez, M.A. Subramanian, Thermal Conductivity of Manganite Perovskites: Colossal Magnetoresistance as a Lattice-Dynamics Transition, Phys. Rev. Lett. **78** (1997) 3947.

[62] K. Berggold, Multiferroic perovskites under epitaxial strain: The case of $TbMnO_3$ thin films, Ph.D thesis, University of Colonia (Germany), 2006.

[63] K. Berggold, J. Baier, D. Meier, J. A. Mydosh, and T. Lorenz, J. Hemberger, A. Balbashov, N. Aliouane and D. N. Argyriou, Anomalous thermal expansion and strong damping of the thermal conductivity of $NdMnO_3$ and $TbMnO_3$ due to 4f crystal-field excitations, Phys. Rev. B **76** (2007) 094418.

[64] G.A. Slack and D.W. Oliver, Thermal Conductivity of Garnets and Phonon Scattering by Rare-Earth Ions, Phys. Rev. B **4** (1971) 592.

[65] J. Yang, Y. P. Sun, W. H. Song, and Y. P. Lee, Thermopower and thermal conductivity of the electron-doped manganite $La_{0.9}Te_{0.1}MnO_3$, J. Appl. Phys. **100** (2006) 123701,

[66] Tokura Y., "Multiferroics as Quantum Electromagnets" *Science* **312**, 1481 (2006).

[67] Z. Jirák, S. Kupricka, Z. Simsa, M. Dlouhá, and S. Vratislav, J. Magn. Magn. Mater. **53** (1985)153.

[68] T. S. Chan, R. S. Liu, Y. H. Lien, C. Y. Huang, and J. G. Lin, Chin. J. Phys. (Taipei) **43** (3-II) (2005) 757.

[69] J. Issing P.h.D. thesis, Koln University, 2011.

[70] J.B. Goodenough and J.M. Longo, Landolt-Bornstien, Neue Serie, Vol.III/4a (Springer, Berlin, 1970).

[71] A. Asamitsu, Y. Moritomo, Y. Tomlaka, T. Arima and Y. Tokura, Nature **373** (1995) 407.

[72] G.A. Swatzky, W. Geertsma and C. Haas, J. Magn. Magn. Mater. **3** (1976) 37.

[73] P.R. Pauthenet, C. Veyret, J. Phys. (France) **31** (1970) 65.

[74] O.L. Makarova, I. Mirebeau, S.E. Kichanov, J. Rodriguez-Carvajal, and A. Forget, Phys. Rev. B **84** (2011) 020408(R).

[75] A.A. Mukhin, V.Yu. Ivanov, V.D. Travkin, A.M. Balbashov, J. Magn. Magn. Mater. **226–230** (2001) 1139.

[76] V. Yu. Ivanov, A. A. Mukhin, A. S. Prokhorov, A. M. Balbashov, and L. D. Iskhakov, JETP Letters **91** (2010) 3927.

[77] J. Farrell, and G A Gehring, New Journal of Physics **6** (2004) 168.

[78] J.M.D. Coey, M. Viret, S. von Molnar, Adv. Phys. **48**, (1999) 167.

[79] J B Goodenough, R I Dass, and J. Zhou, Solid State Sci. **4** (2002) 297.

[80] J. B. Goodenough, A. Wold, R. J. Arnott, and N. Menyuk, Phys. Rev. **124** (1961) 373.

[81] J.-S. Zhou, H. Q. Yin, and J. B. Goodenough, Phys. Rev. B **63** (2001) 184423.

[82] J. Töpfer and J. B. Goodenough, Eur. J. Solid State Inorg. Chem. **34** (1997) 467.

[83] J. J. Blasco, J. García, J. Campo, M.C. Sánchez, and G. Subías, Phys. Rev B **66** (2002) 174431.

[84] P. G. De Gennes, Phys. Rev. **118** (1960) 141.

[85] D. N. Argyriou, J. F. Mitchell, C. D. Potter, D. G. Hinks, J. D. Jorgensen, and S. D. Bader, Phys. Rev. Lett. **76** (1996) 3826.

[86] S B Wilkins, P D Spencer, P D Hatton, S P Collins, M D Roper, D Prabhakaran and A T Boothroyd, *Phys. Rev. Lett.* **91** 2003 167205.

Chapter 4

$Tb_{1-x}Al_xMnO_3$ and $TbMn_{1-x}Al_xO_3$ thin films

Studies of rare earth manganites ($RMnO_3$, R=rare earth ion) in thin film form started to be available only since 2005 and have been performed in various compositions for R changing from La to Ho [1]. The most studied being $LaMnO_3$, due to its colossal magnetoresistance observed in bulk, upon doping by Sr or Ca. Several reports have revealed induced or enhanced ferromagnetic interactions in $RMnO_3$ (i.e. R=Ho, Y, Tb), which are absent in the bulk form [2]. Although no clear statement is offered about the nature of the weak ferromagnetism observed in $RMnO_3$ thin films, two possible origins were discussed. One of them relates the weak ferromagnetism to spin canting, as previously discussed, and the other one to uncompensated spins at the boundaries of AFM domain walls [3], giving as example the weak ferromagnetism observed in AFM nanoparticles [4]. Although these reports are very recent, the origin of the weak ferromagnetism in the $RMnO_3$ family is controversially discussed and should still be confirmed. Thus, multiferroic materials represent a grand scientific challenge on understanding complex solid state systems with strong correlations between multiple degrees of freedom. In this regard, the research on multiferroic thin films can help to shed light on the physics of the phenomenon because the multiferroic properties of thin films can be enhanced, compared to those of the bulk counterparts, through careful tuning of synthesis conditions. Particularly, strain (either tensile or compressive) engineering is an effective tool to induce lattice distortion and to optimize physical properties [5]. In the case of epitaxial multiferroic thin films, the properties can be engineered by substrate-induced strain. Epitaxial stabilization of metastable structures is also possible. $YMnO_3$ was grown on $SrTiO_3$ with an orthorhombic (o-) structure by X. Marti *et al.* [6], by using pulsed

laser deposition. A ZFC-FC hysteresis was also found below the antiferromagnetic ordering temperature, associated with a ferromagnetic response. The strain state (and specially the contraction of the b-axis) of the films was suggested as the likely origin of the ferromagnetic signal in the films [6]. In general, by revising the literature in the last two years, it is easily recognized that induced/enhanced magnetization for different manganite thin films was consistently reported, although a clear explanation has not been offered yet. Nevertheless, a general origin for the induced ferromagnetism observed in epitaxially stabilized $RMnO_3$ thin films cannot be discarded. As explained above, the structural distortion of the orthorhombic perovskite unit cell can lead to large modifications of the ferroelectric, magnetic and electronic properties of rare earth manganites. The advantage of the thin films is that they allow one to change the crystallographic structure without modifying the cation on the rare earth site. This permits a detailed understanding of the relationships between the structure and the physical properties in thin film form. Thus, the ultimate goal of this last part of the thesis is to try to tune the physical properties of the material using epitaxial strain, imposed by the substrate. In the present thesis, thin films of $TbMnO_3$ under epitaxial strain were deposited on single crystals of (001)-oriented $SrTiO_3$ and MgO substrates using magnetron sputtering. Detailed structural and magnetic characterization has been performed in order to learn from the thin film behavior of $Tb_{1-x}Al_xMnO_3$ about the properties of multiferroics and manganites in general. As the practical applications of advanced materials in fields related with microelectronic and/or sensors and actuators require the fabrication of epitaxial thin films, several approximations were tested in the course of this thesis until the ultimate objective was achieved. This means that several deposition parameters needed to be optimized before epitaxial thin films could reliably be grown. For this reason, the

experimental results of measurements on the different thin films are sequentially presented according with the respective deposition parameters used to the fabrication of each film. The last results correspond to the ideal epitaxial $TbMnO_3$ thin films grown on $SrTiO_3$ substrates.

Figure 4.1 shows the XRD patterns of $Tb_{0.7}Al_{0.3}MnO_3$ films (~100 nm thick) deposited on a (001)-$SrTiO_3$ (a=3.90 Å) and (001)-MgO (a=4.12 Å) substrates. The films were deposited using rf sputtering (60 W). Substrate temperature varied between 700° C and 750° C and the Ar-pressure was $1x10^{-2}$ mbar. It is evident from the plot that the substrate material strongly influences the orientation of the films. Indeed, the films grow highly oriented in two different directions on the chosen substrates with no peaks identifiable as originating from by spurious phases.

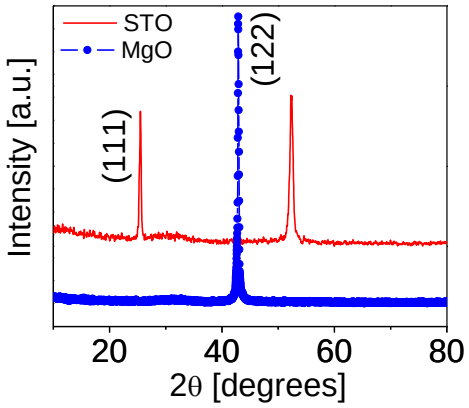

Figure 4.1. XRD spectra from $Tb_{0.7}Al_{0.3}MnO_3$ films grown on $SrTiO_3$ and MgO substrates by rf-sputtering.

The well defined peaks suggest that the crystal structure of the films is distinctly formed on both substrates. Furthermore, the absence of additional $TbMnO_3$ reflections in the XRD patterns of both samples suggests a (111) and (122) oriented textured growth of the films deposited on $SrTiO_3$ and MgO substrates, respectively. As mentioned above, bulk $TbMnO_3$

has an orthorhombic perovskite structure which (in the pseudocubic conventional) has lattice parameters of 3.93 Å in-plane and 3.70 Å out-of-plane [5]. Therefore, the films should be compressively strained by the $SrTiO_3$ substrate resulting in the tetragonally distorted orthorhombic phase of $TbMnO_3$. In turn, the films on MgO should be subjected to tensile strain. Recently, the successful growth of $Tb_{1-x}Al_xMnO_3$ thin films (x=5 % and 10 %) on $SrTiO_3$ substrates with thicknesses varying between 10 and 100 nm by the pulsed laser deposition (PLD) technique was reported [7]. The introduction of Al in the films caused the displacement of the transition temperatures due to the Mn^{3+} and Tb^{3+} ordering toward higher temperatures for all samples. Nevertheless, the most important effect of the Al doping was the enhancement of the ferromagnetic behavior of the $TbMnO_3$ thin films, improving the magnetic performance of this material. In an interesting work by Marti *et al*., a ferromagnetic response was observed in *c*-textured $TbMnO_3$ thin films grown on (001)-oriented $SrTiO_3$ substrates by PLD technique [8]. The emergence of ferromagnetism was attributed to epitaxially induced strain. Here, the unit cell volume was tuned (contracting up to a 2 %) by varying thickness and deposition conditions. The ferromagnetic response of the films correlated then with the unit cell deformation.

Figure 4.2(a) shows the zero-field cooling (ZFC) temperature dependent magnetization of $Tb_{0.7}Al_{0.3}MnO_3$ films deposited on STO and MgO substrates. The films were measured in a field of 1000 Oe applied parallel to the film plane (in-plane geometry). Data were plotted up to 100 K to appreciate the transitions occurring at low temperatures. The $M(T)$ curves plotted in the main panel of Fig. 4.2(a) show two anomalies at T~45 K and T~10 K, which were identified as changes in the slope of the first derivative curves. These temperatures indicated are related with the magnetic ordering of the Mn^{3+} and Tb^{3+}, respectively [9]. In the inset of

Fig. 4.2(a), the *M*(T) dependence of an undoped and doped (x=0.3) $TbMnO_3$ in bulk form is replotted. The dramatic influence of the Al doping on the magnetic behavior of the compound is clearly appreciated in this plot. The $TbMnO_3$ film (not shown) showed a *M*(H) behavior that resembles that showed by the bulk counterpart. Magnetization measurements as a function of applied magnetic field at 5 K for $Tb_{0.7}Al_{0.3}MnO_3$ films deposited on STO and MgO substrates are shown in Fig. 4.2(b). Although the ferromagnetic response is weak, well defined hysteresis loops are achieved for the studied films. Nevertheless, the more interesting effect here is the decided influence of the substrate material on the ferromagnetic behavior of the films. Evidently, the performance of films grown on MgO substrates is higher than that of films grown on STO. As both films have the same thickness, the effect of the strain between film and substrate should play a major role in the magnetic response of the films. As for the origin of ferromagnetism in Al-doped $TbMnO_3$, it is probable that this effect is linked to the coupling between magnetization and strain. In this regard, there is an analogy between the induction of ferromagnetism in epitaxial antiferromagnets and the well-known induced ferroelectricity in incipient ferroelectrics [10]. Indeed, antiferromagnets are piezomagnetics and the epitaxial strain should induce a magnetic moment in the films. In turn, the results presented in Fig. 4.2(a) (inset) show that the introduction of Al in the $TbMnO_3$ lattice increases the magnetization. This result is a consequence of the substitution of Tb (ionic radius r_{Tb}=1.04 Å) for an ion having almost half the radius (r_{Al}=0.535 Å), leading to a deformation of the cell that result in spin canting. The strong coupling of the magnetic structure of $TbMnO_3$ to the lattice has been recently demonstrated [11]. The behavior observed in Al-doped $TbMnO_3$ is similar to that reported by Goto *et al*. in Gd doped $TbMnO_3$ crystals [12]. The Gd doping leads to a canted AFM state (weak ferromagnetism) product of the Gd incorporation into the cell. Here, it should be mentioned that the weak ferromagnetic

signal observed in $TbMnO_3$ films is more difficult to explain. To determine if the net magnetization is truly intrinsic to the $TbMnO_3$ film, more sophisticated experiments such as polarized neutron reflectometry should be conducted [13]. Although weak ferromagnetism in $TbMnO_3$ films grown on (001)-oriented $SrTiO_3$ substrates has been reported in the literature, the authors could not completely rule out extrinsic effects such as uniform distribution of impurities as the origin of ferromagnetism in the undoped films [13].

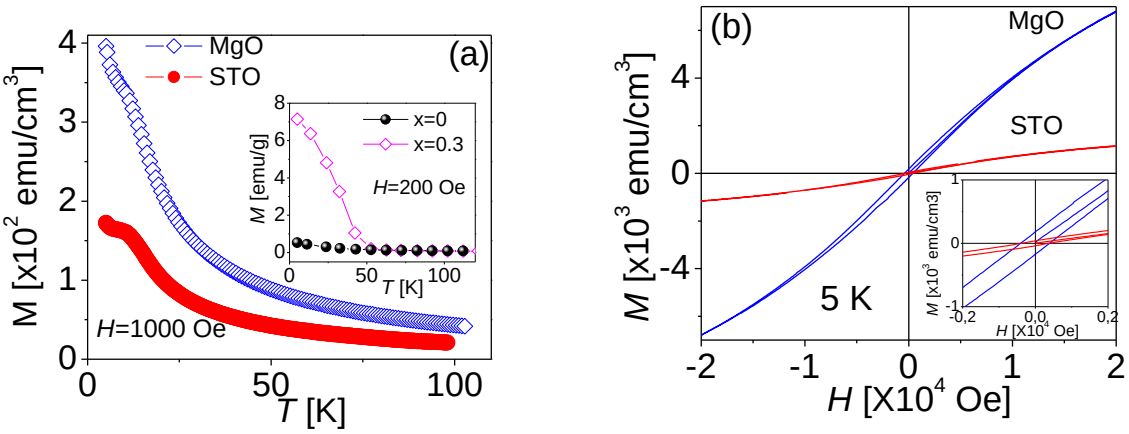

Figure. 4.2. (a) Temperature-dependent magnetization curves for Al-doped $TbMnO_3$ films measured with a 1000 Oe magnetic field in in-plane geometry after ZFC procedure. Inset: Temperature-dependent magnetization curves for polycrystalline $Tb_{1-x}Al_xMnO_3$ (x=0, 0.3) samples measured with a 200 Oe magnetic field after ZFC procedure. (b) Magnetic-field-dependent magnetization curves for Al-doped $TbMnO_3$ films at 5 K. The inset shows an enlarged picture of the low-field data with a clear hysteresis.

Figure 4.3 shows the XRD patterns of a $TbMnO_3$ film grown on an (100)-STO substrate using *dc* sputtering technique. The growth took place at 750° C under an oxygen pressure of 3 mbar and a power of 150 mW. After deposition, the chamber was flooded with oxygen under a pressure of 1000 mbar, and then kept there for 1 h before cooling down to room temperature. The XRD patterns were recorded in grazing incidence configuration in order to avoid the superposition with the peaks stemming from the substrate. Only one peak is observed in this plot, which was indexed as the (220) reflection of $TbMnO_3$. No peaks

identifiable as originating from additional phases are observed in this plot. The appearance of only (*hh*0) reflections confirms that the as-deposited films are single phase and grown with the (*hh*0) planes parallel to the sample surface. It is widely known that while in bulk materials the lattice distortions can be varied by applying hydrostatic or chemical pressure, and for thin epitaxial ABO_3 perovskite films a substrate-induced biaxial stress is an effective tool to modify the electron-lattice coupling. For heteroepitaxial film growth on single crystal substrates, lattice mismatch is the critical parameter which influences the resultant film lattice distortion and strain. The lattice mismatch is defined as $m=(a_0-a_s)/a_s$, where a_0 and a_s are the unstrained layer and substrate in-plane lattice parameters, respectively [14]. In the present study, $TbMnO_3$ thin films were deposited on (001)-oriented $SrTiO_3$ substrates. (001)-oriented $SrTiO_3$ is preferred in studies of epitaxy in perovskites because it can be obtained with atomically flat surfaces, favoring high-quality growth. The $SrTiO_3$ substrate is a cubic perovskite with lattice constant of a=3.905 Å. The highly distorted perovskite $TbMnO_3$ crystallizes in an orthorhombic structure (space group: *Pbnm*) with lattice constants of a_0=5.309 Å, b_0=5.812 Å, c_0=7.386 Å, $(a_0^2+b_0^2)^{1/2}$=7.4025 Å [15]. At this point, it should be mentioned that lattice parameters reported for the bulk/single-crystal $TbMnO_3$ system, particularly the *c*-lattice parameter, vary considerably. This has been attributed to different growth conditions [16]. Based on the lattice parameters of bulk, orthorrombic $TbMnO_3$ and cubic $SrTiO_3$, it is expected that the lattice mismatch for the *a*- and *b*-parameters of $TbMnO_3$ with respect to the diagonal line of the *ab*-plane of (001)- $SrTiO_3$ is -3.7 % along the [100] direction of $SrTiO_3$ crystal, and of 5.4 % along the [010] direction of $SrTiO_3$ crystal. If the *c*-parameter of $TbMnO_3$ is placed within the spacing of 2*a* or 2*b* of (001)-$SrTiO_3$, it suffers a tensile strain of -5.3 %. Therefore, the energy cost for *c*-axis of $TbMnO_3$ lying on the surface of (100)-$SrTiO_3$ substrate is comparable to that for *ab*-plane lying on the surface of (100)-

$SrTiO_3$. The expectation based on the estimation of directional strain is consistent with the data of XRD in Fig. 4.3. $TbMnO_3$ films grown over single-crystalline STO substrates by PLD featured an orthorhombic structure and were [00ℓ]-oriented (with the *c*-axis perpendicular to the surface) [9]. These films shared the pseudocubic lattice parameters of the substrate (3.905 Å) and were, therefore, compressed in the plane directions. Although (001)-oriented $SrTiO_3$ were used for depositing the $TbMnO_3$ films by sputtering, the (00ℓ) orientation of the films was not verified. Instead, the films were [*hh*0] oriented. In this regard, it is apparent from the reports on $TbMnO_3$ films grown on $SrTiO_3$ substrates using PLD technique that the growing parameters (say substrate temperature, Laser fluency, oxygen partial pressure, etc.) to obtain (00ℓ)-oriented films are as far as optimized. This is not the case for $TbMnO_3$ films grown by sputtering. The sputtering is a much slower process as compared with PLD. Hence, the thermodynamic of the growing process should be different. Probably, the energy involved in the sputtering process, consistent with the deposition parameters, is still not tuned so as to allow an epitaxial growth similar to that achieved by PLD technique.

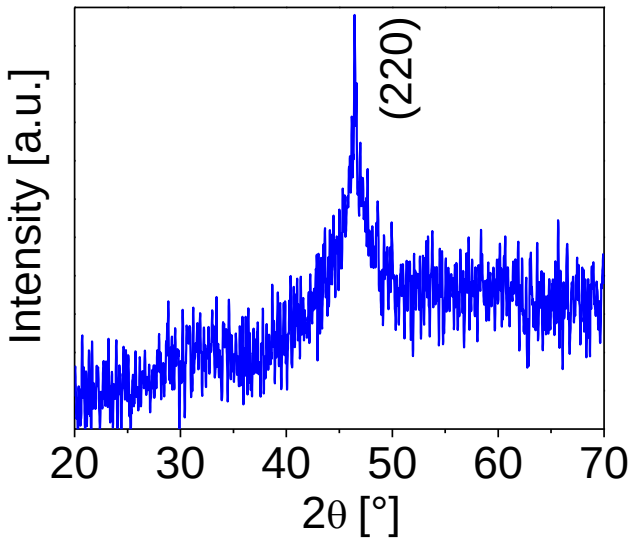

Figure 4.3. XRD pattern of a $TbMnO_3$ film grown on an $SrTiO_3$ substrate.

The temperature dependence of the in-plane magnetization of an $TbMnO_3$ film recorded in a magnetic field of 1000 Oe is presented in Fig. 4.4(a). Interestingly, the $M(T)$ profile shows well defined features near ~45 and ~30 K (inset), close to those observed in single-crystalline $TbMnO_3$ corresponding to the sine wave ordering of Mn^{3+} moments and the incommensurate–commensurate (T_{lock}) transition. Clear signatures in $M(T)$ for the ordering of the Mn moments have hardly been reported for $TbMnO_3$ thin films grown by PLD technique [17]. Interesting information regarding the magnetic properties of TMO films is obtained through magnetization isotherms. The $M(H)$ isotherms for a $TbMnO_3$ film measured at different temperatures in magnetic fields up to 10 kOe applied along the substrate after ZFC is presented in Fig. 4.4(b). The hysteretic behavior is clearly observed up to temperatures as high as 70 K indicating ferromagnetism order in the $TbMnO_3$ film. This is in clear opposition to the antiferromagnetic order observed for bulk $TbMnO_3$. At this point, it is important to signalize that special attention should be paid to the possible existence of Mn_3O_4 impurities, which are ferrimagnetic with a T_C of 44 K [18]. The presence of this impurity could account for the presence of ferromagnetism in the sample at low temperatures. Nevertheless, additional peaks stemming from Mn_3O_4 were not detected by X-ray diffraction neither in the target nor in the film. A magnetic signal generated by Mn_3O_4 would imply a too large amount of the impurity in the films, which would have been detected by X-ray diffraction. One of the possible origins of the observed ferromagnetism in thin films may be the coupling between magnetization and strain imposed by the substrate [9]. In this regard, the epitaxial growth of $TbMnO_3$ films on STO substrates using PLD technique has been reported by several groups [13]. The origin of the net magnetic moments exhibited by some of the $TbMnO_3$ films grown by this technique has been attributed to epitaxial strain-induced

unit cell deformation, leading to changes in their magnetic interaction [6]. Certainly, the magnetic coupling in a compound can strongly depend on the unit-cell geometry. When a compound gets strained, the change in geometry can therefore lead to a change of the magnetic ordering temperature or even alter the type of order. Strain can have tremendous effects on orbital ordering [19], which determines the magnetic properties of $TbMnO_3$. Nevertheless, the study of the mechanism behind the ferromagnetism in $TbMnO_3$ films is difficult because crucial factors such as the subtle competition between ferromagnetic and antiferromagnetic exchange constants in this material [20] and the likely influence of the Tb ions. This conduces to the need of a more complex analysis of the magnetic structure of the films is needed, including the oxygen atomic positions. As it was previously mentioned, the possible origin of the observed ferromagnetism in the $TbMnO_3$ films is the direct coupling between magnetization and strain. This possibility is supported by the analogy between the induction of ferromagnetism in epitaxial antiferromagnets and the well-known induced ferroelectricity in incipient ferroelectrics [10,21]. In this regard, the strong coupling of the magnetic structure of $TbMnO_3$ to the lattice has been recently demonstrated [11]. Finally, the possibility that the origin of ferromagnetism lies in the microstructure has been explored [22]. There, TEM images revealed that the size of the orthorhombic domains decreases for decreasing thickness, leading to a larger volume ratio of domain walls as the films get thinner. This seemed to be more relevant in order to understand the induced ferromagnetism, and the absence of a lock-in transition in such films. It was argued that although the orthorhombic domains of the bulk material are antiferromagnetic in character, the interactions at the crystallographic domain walls could give rise to the observed ferromagnetic component. Moreover, the long range order of the spin cycloid that gives rise to the lock-in and ferroelectric transition would be disturbed by the presence of crystallographic domain

walls/boundaries, which prevented the appearance of long-range order and macroscopic polarization in the films grown by PLD technique.

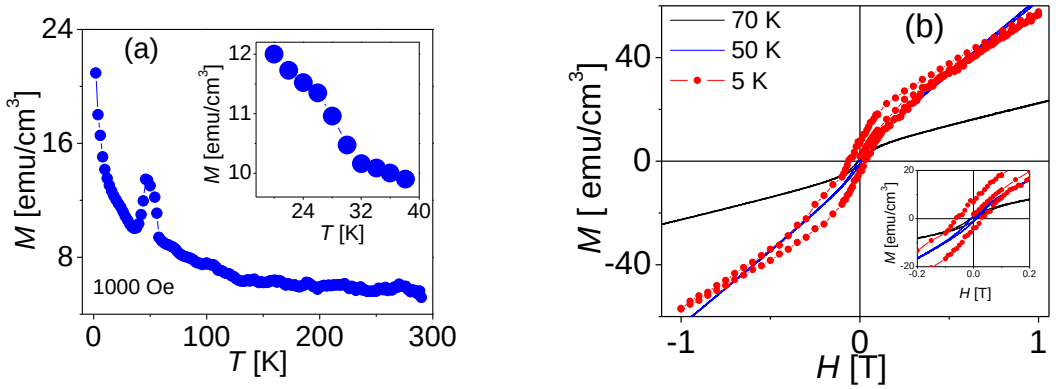

Figure 4.4. (a). Temperature-dependent magnetization curve for a TMO film on STO measured with a 1000 Oe magnetic field applied along the substrate after ZFC. Inset: enlarged picture of the low-temperature data. (b) Magnetic-field-dependent magnetization curves at 5, 50, and 70 K. The inset shows an enlarged picture of the low-field data taken at the different temperatures with a clear hysteresis. The diamagnetic contribution of the substrate has been deduced of the raw data. The paramagnetic contribution stems from the Tb ions.

Although, some work has been carried out for epitaxial films grown by PLD, this is still lacking for films grown by sputtering. In this section, experimental results of the growth and characterization of epitaxial $TbMnO_3$, and $TbMn0_{.9}Al_{0.1}O_3$ thin films (~100 nm thin) on (001)-oriented $SrTiO_3$ substrates are presented. The films were grown using a high oxygen pressure *dc* magnetron sputtering system. $TbMnO_3$ films (~100 nm) were deposited in oxygen atmosphere at a pressure of 3 mbar, power of 30 W, and a substrate temperature of 780° C. After deposition, the substrate temperature was lowered to 450° C and the chamber was then flooded with oxygen at a pressure of ~800 mbar. The films were annealed under these conditions for 1 h.

From the structural studies, it is confirmed that both the undoped and Al-doped $TbMnO_3$ films were epitaxially grown with their *c* axes normal to the substrate plane. Figure 4.5 shows

broader 2θ-ω scans of both films including both the (001) and the (002) $SrTiO_3$ Bragg reflections. No secondary or impurity phases could be observed for these samples. Particularly, the absence of spurious diffraction peaks in the XRD data of the doped film points to an adequate solid solution between Mn^{3+} and Al^{3+} cations in the chosen concentration range. Thus, XRD shows that the films are single phase and (00ℓ)-oriented. The inset of Fig. 4.5 shows that the full width at half maximum in the rocking curve of the (002) peak is about 0.4° and 0.3° for the undoped and Al-doped samples, respectively. This finding suggests a good crystalline quality of the $TbMn_{1-x}Al_xO_3$ films ($x \leq 0.1$) grown by DC sputtering. From the position of the XRD peaks, an out-of-plane lattice parameter of 0.747 and 0.754 nm was determined for the undoped and Al-doped films, respectively. The lattice parameters of the films are larger than the c=0.740 nm reported for $TbMnO_3$ in bulk form. Therefore, a small in-plane compressive strain should be present in the films, resulting in the tetragonally distorted orthorhombic phase of $TbMnO_3$. It is expected the orthorhombic unit cell of $TbMnO_3$ to be grown on a $3.905\sqrt{2}$x$3.905\sqrt{2}$ Å square $SrTiO_3$ lattice, which can accommodate the in-plane film lattice better. The achieved results are in good concordance with previous reports on $TbMnO_3$ thin films grown on STO substrates [23]. At this point, it is important to note that an out-of-plane lattice parameter of 7.474 was reported for $TbMnO_3$ films (~100 nm thin) fabricated by pulsed laser deposition in oxygen atmosphere at a pressure of 0.25 mbar [22]. This value of the c-axis was considered to be larger than that expected for the compressively strained samples. Here, it was suggested that a larger out-of-plane lattice parameter than the expected one could be explained by a film whose strain is relaxed by means of oxygen vacancies, because these vacancies can expand the unit cell [24]. The authors in Ref [22] varied the oxygen pressure during deposition up to 0.9 mbar and observed

a linear decrease of the out-of-plane lattice parameter with increasing oxygen pressure, consistent with the number of oxygen vacancies decreasing for increasing pressures. Nevertheless, the larger value of the *c*-axis encountered for the films grown at oxygen pressures as high as 3 mbar (present work) suggests that the role of the oxygen vacancies in determining the value of the *c*-axis in TMO films should be further investigated. In this regard, the most remarkable effect generated by the substitution of Mn^{3+} by Al^{3+} ions is the increase in the value of the *c*-axis. Accordingly, the orthorhombic distortion should be reduced in the *ab* plane, which is expected because of the size difference between Mn^{3+} and Al^{3+} cations [25]. As previously stated, in the case of polycrystalline $TbMn_{1-x}Al_xO_3$ samples ($x \leq 0.1$), it was verified that the contraction produced by the *b* axis shrinking $\Delta b = -0.48$ Å/x), and that of the *a* axis $\Delta a = -0.09$ Å/x) for the same concentration range [26]. Moreover, the reduction of the orthorhombic distortion in the *ab* plane has been ascribed to the partial replacement of strongly distorted MnO_6 octahedra (Jahn-Teller-like) by the regular AlO_6 ones [27]. X-ray diffraction was also used to map selected areas of the reciprocal space. Figure 4.6 shows a typical X-ray reciprocal space map (RSM) around the (103) STO Bragg reflection for an epitaxially grown $TbMn_{0.9}Al_{0.1}O_3$ film (~100 nm). The central sharp spot corresponds to the position of the STO Bragg peak and the other broader visible reflection around it is from the film. It is observed that the (116) diffraction peak of the film is not located near the dashed line and somewhat diffused along the transverse scan direction. The not coincidence of the two reflections and the shape of the peak is a result of partial strain relaxation which, for the analyzed films, seems to occurs at thicknesses lower than 100 nm.

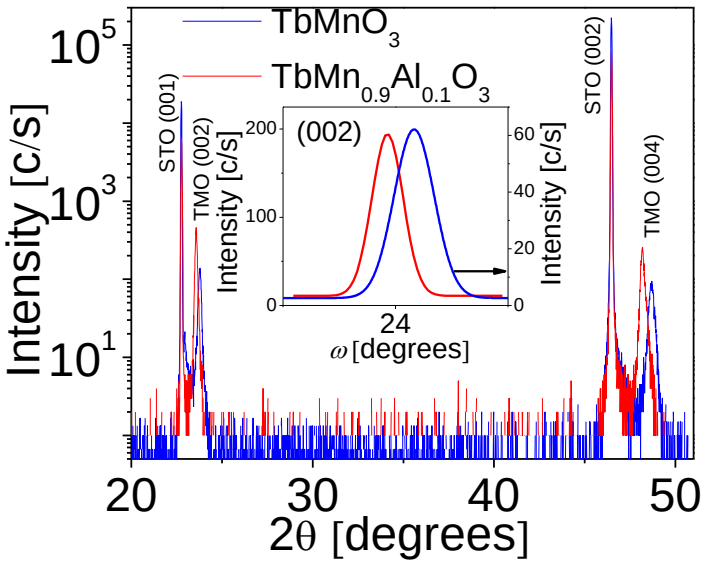

Figure 4.5. 2θ-ω scans of ~100 nm thin $TbMn_{1-x}Al_xO_3$ (x=0, 0.1) films grown on a (001)-oriented STO substrate. Inset: rocking curves recorded around the TMO (002) peak.

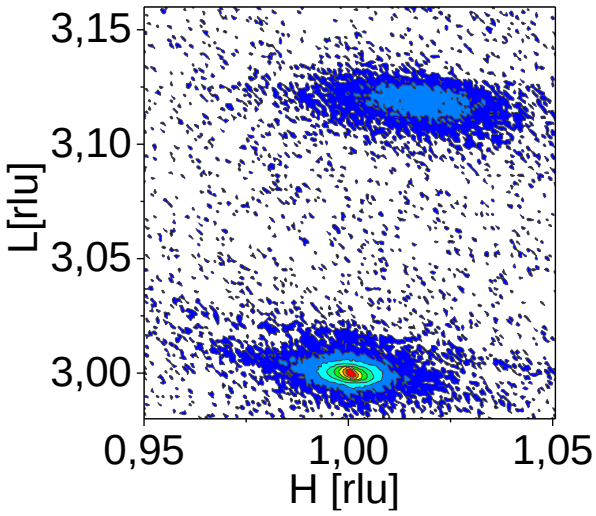

Figure 4.6. RSM around the (103) STO Bragg reflection for a ~100 nm thin $TbMn_{0.9}Al_{0.1}O_3$ film.

The field-cooling (FC) temperature dependences of the susceptibility, M/H, for representative $TbMnO_3$ and $TbMn_{0.9}Al_{0.1}O_3$ films grown on STO substrates are shown in Fig. 4.7. The magnetization curves in Fig. 4.7 show a sharp increase in magnetization with

decreasing temperature at T~40 K. This is verified by the first derivative of both curves [insets to Fig. 4.7(a) and 4.7(b)], which shows a well-defined anomaly around 40 K. This temperature is very close to T_{N1}≈42 K, where the Mn^{3+} magnetic moments have sinusoidal antiferromagnetic (AF) order [28]. In turn, Figure 4.8 shows the magnetic hysteresis loops recorded at 5 K for $TbMnO_3$ and $TbMn_{0.9}Al_{0.1}O3$ thin films grown on STO substrates. Well-defined magnetic loops and spontaneous magnetization are clearly distinguished in both samples. Magnetization does achieve a complete magnetic saturation in the considered magnetic field range. No metamagnetic transitions, as those observed in $TbMnO_3$ and $TbMn_{0.9}Al_{0.1}O_3$ single-crystals [26], are evidenced for the thin films. Although the presence of low temperature ferromagnetism in the undoped $TbMnO_3$ films should be carefully analyzed, it is apparent that this anomalous ferromagnetism is associated with the strain-induced distortion generated by the lattice mismatch between the film and substrate. A modified microstructure is the direct consequence of this effect. For instance, it has been reported that the ground state of $YMnO_3$/STO thin films can be changed from E-AFM to spiral-spin-order (SSO) by strain corresponding to the reduced othorhombicity of the films [29]. It was also verified that the non-collinear SSO phase in bulk $BiFeO_3$ crystals can be easily replaced with a collinear spin order through strain engineering (either compressive or tensile) in thin films [30].

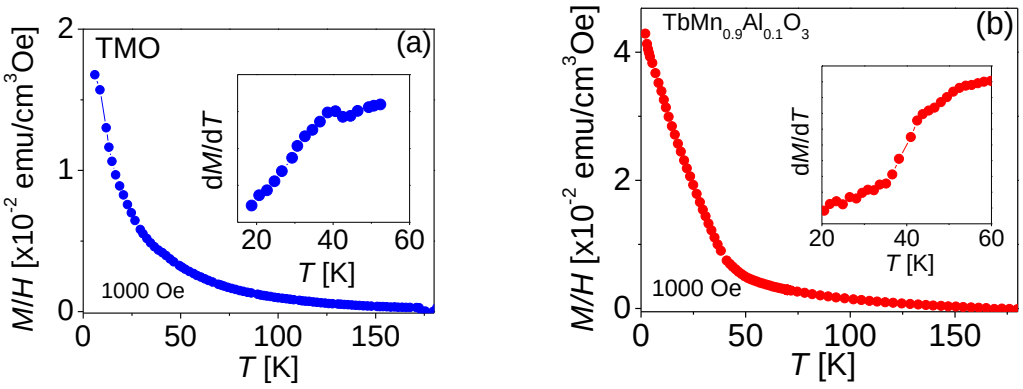

Figure 4.7. Temperature-dependent magnetization curves measured with a 1000 Oe magnetic field applied along the substrate after FC procedure for an undoped (a) und Al-doped (b) $TbMnO_3$ film. Insets show the first derivative of the $M(T)$ curves plotted around 40 K.

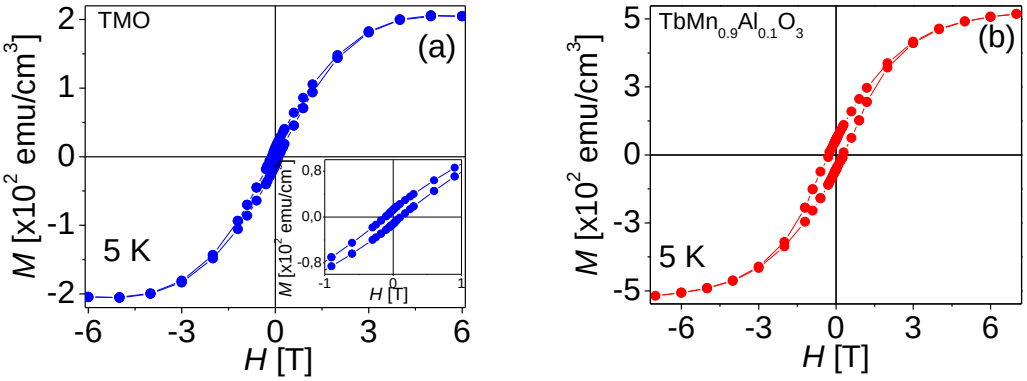

Figure 4.8. Magnetic-field-dependent magnetization curves at 5 K for a ~100 nm thin undoped (a) und Al-doped (b) $TbMnO_3$ film. The insets show an enlarged picture of the low-field data taken at 5 K with a clear hysteresis.

By comparing the $M(T)$ and $M(H)$ dependences shown in Fig. 4.7 and Fig. 4.8, it is evident that the Al-doping enhances the ferromagnetism in $TbMnO_3$. The larger values of the remnant magnetization, maximum magnetization, and coercive field of the Al-doped films support the latter statement. By using powerful characterization techniques such as neutron diffraction, it was argued that the dilution of magnetic ions (Mn^{3+} by Al^{3+}) leads to weakening of the superexchange Mn-O-Mn interaction [26]. As a consequence the transition temperature T_{N1} shifted to lower temperatures by increasing the Al-doping level. The trend

observed in Fig. 4.7 is consistent with the results reported in Ref [26]. In an interesting study, substitution of Mn with a nonmagnetic ions has been carried out in order to test the role of the $J_{Mn\text{-}Tb}$ interaction [31]. It was shown that the Mn magnetic ordering vanished for x∼0.3, which is well above the percolation limit for a metal with octahedral coordination. It was also reported that small substitutions of Mn have little effect on the magnetoelectric properties of the Mn sublattice but can strongly affect the magnetic ordering of Tb moments [31]. The authors suggested that such an ordering comes from the competition between $J_{Mn\text{-}Tb}$ and the direct coupling between Tb moments, $J_{Tb\text{-}Tb}$. Finally, the origin of ferromagnetism could be in the microstructure [22]. Certainly, TEM images taken on $TbMnO_3$ thin films grown on $SrTiO_3$ substrates by PLD revealed that the size of the orthorhombic domains decreases for decreasing thickness and, thus, that the thinner the films, the larger the volume ratio of domain walls present. This fact was considered as most relevant in order to understand the physical properties observed in the films, that is the induced ferromagnetism. Although the orthorhombic domains of the bulk material are known to be antiferromagnetic in character, also in agreement with the negative Curie-Weiss temperature measured in the films, the interactions at the crystallographic domain walls could give rise to the observed ferromagnetic component. Moreover, it was argued that the long range order of the spin cycloid that gives rise to the lock-in and ferroelectric transition, is disturbed by the presence of crystallographic domain walls/boundaries, which precludes the appearance of long range order and macroscopic polarization, consistent with the absence of the ferroelectric transition at ~30 K. Without doubt further studies are necessary in order to gain a deeper insight into the mechanism leading to the enhanced ferromagnetism in Al-doped $TbMnO_3$ thin films.

In order to have a complete characterization of the epitaxial $TbMnO_3$ and $TbMn_{0.9}Al_{0.1}O_3$ thin films, the morphological and electronic properties were analyzed using AFM and XPS techniques. Figure 4.9 shows an AFM image for a $TbMnO_3$ film (~100 nm thin) grown on an $SrTiO_3$ substrate. The corresponding AFM image for the $TbMn_{0.9}Al_{0.1}O_3$ film is shown in Fig. 4.10. It is observed that groups of columns dominate the film morphology of both films. Some ridges (not deep) between groups of columns can also be appreciated on these images. The films are atomically flat with average roughness of 1.45 and 1.27 nm for the undoped and Al-doped films, respectively.

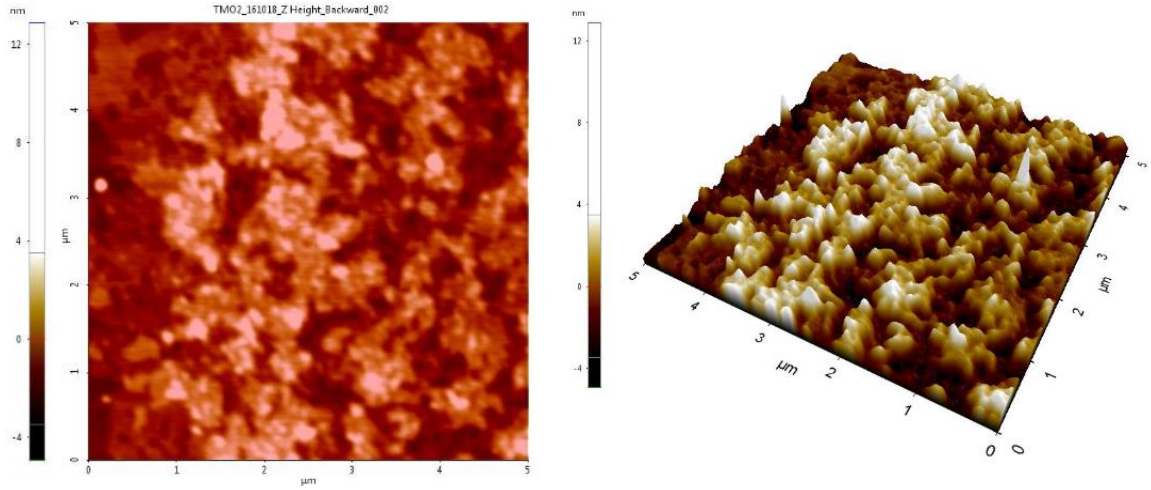

Figure 4.9: (a) AFM images of a 100 nm thin $TbMnO_3$ film grown on an $SrTiO_3$ substrate.

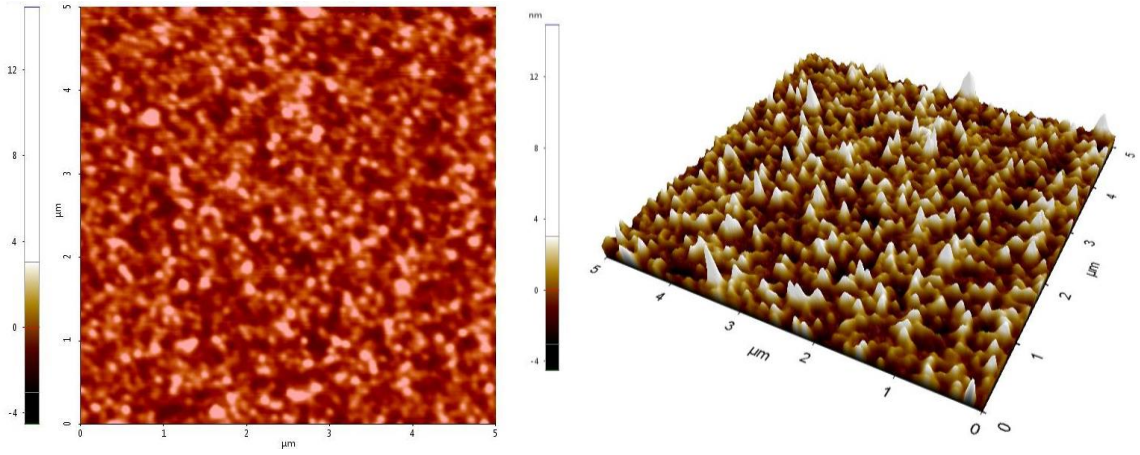

Figure 4.10: AFM images of a 100 nm thin $TbMn_{0.9}Al_{0.1}O_3$ film grown on an $SrTiO_3$ substrate.

X-ray photo-emission spectroscopy (XPS) was used to determine the possible oxidation states of the elements present in the $TbMnO_3$ films grown on $SrTiO_3$ substrates. XPS is a powerful tool to investigate the surface chemistry [32]. The general measurements indicate that the concentration of Mn and Tb on the film surface is not uniform. Light colored patches were identified on the sample using the photo taken at the sample introduction port [Fig. 4.11(a)]. Using imaging treatment software, one of these patches was identified by a light area that is surrounded by a darker region. Survey spectra of each region were obtained using a 50 µm diameter, 12 W, X-ray beam. The results of the survey spectrum showed that the dark area contained no metals while the light area contained a small (<1%) amount of Tb and Mn. High resolution spectra of C 1s, O 1s, Mn $2p_{3/2}$ and Tb 4d were taken using the same X-ray beam size on only the lighter colored area. Information of elements in the thin films and contamination adsorbed on the surface can be given from the wide scan spectra of XPS. Figure 4.11(b) shows the XPS survey scan, recorded at 20 take-off angle for an $TbMnO_3$ thin film. From the XPS survey spectra only Tb, Mn, and O are identified with a small contribution of C and Sr from the substrate.

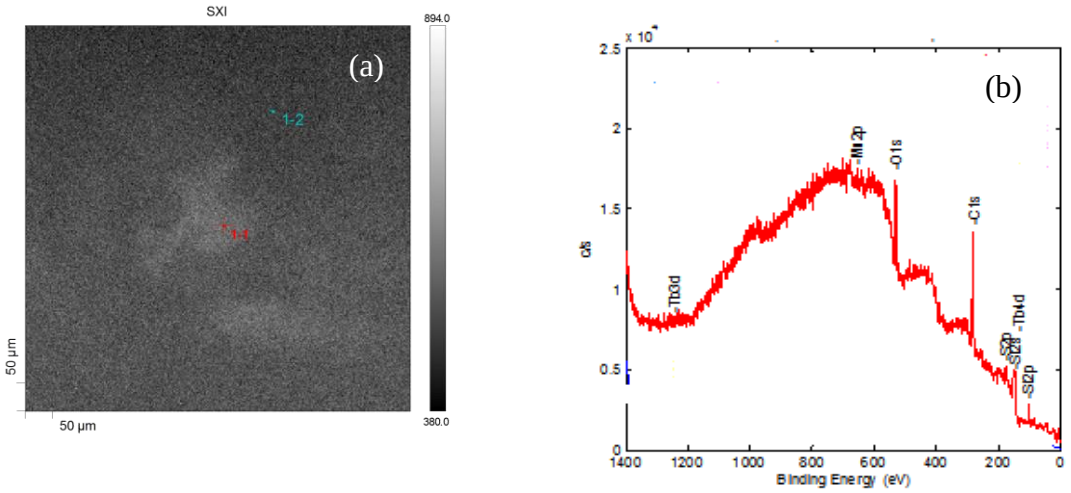

Figure 4.11. (a) Image of a the surface of an $TbMnO_3$ film on an $SrTiO_3$ substrate. Presence of small amount of Tb and Mn are marked with red crosses. In the region distinguished with green crosses no Tb and Mn elements were detected. (b) Survey scans of X-ray photoemission spectra for an $TbMnO_3$ thin film deposited on an $SrTiO_3$ substrate.

Even though the study of the Mn2p core level is not an easy task, due to the deconvolution of this core level into multiplets [33], the manganese Mn2p level [Fig. 4.12(a)] exhibits the typical features of this core shell for a valence of 3+. This valence features a peak at a binding energy of 641.7 eV (Mn $2p_{3/2}$) with an FWHM) of ~3 eV. Thus, the low binding energy peak at 641.8 eV is consistent with a nominal Mn valence of +3. In addition, the splitting between the two Mn2p peaks, shown in Fig. 4.12(a), is about 11.7 eV, consistent with that expected for Mn^{3+}. Note that the Mn2p core level shows no shake-up satellites typical for the presence of Mn^{2+}. The Tb 4d peak is shown in Fig. 4.12(b). This peak features the typical asymmetric form beginning with a binding energy of ~150 ev, which correspond to the Tb $4d_{5/2}$ [34].

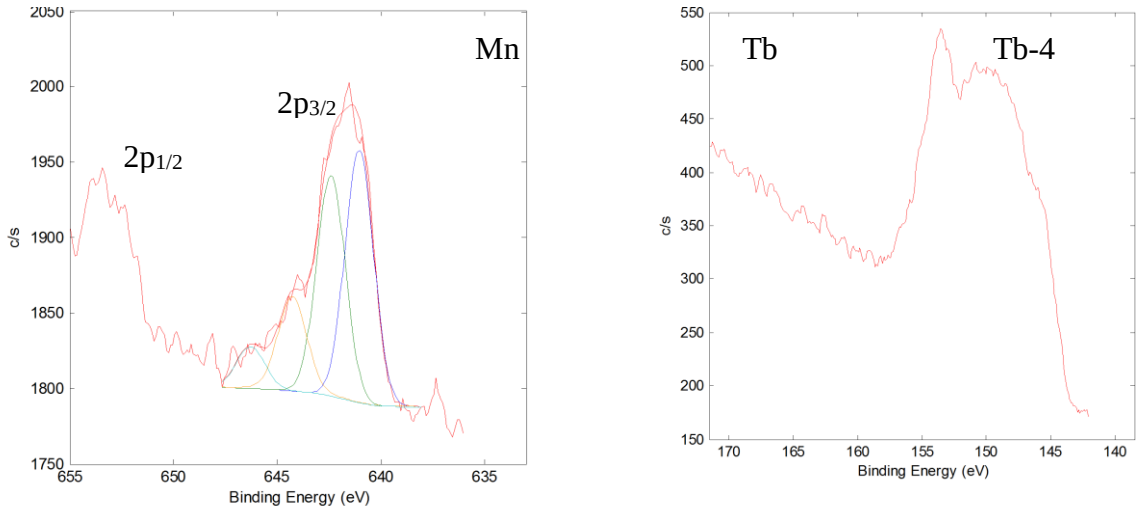

Figure 4.12. High-resolution XPS spectrum for the Mn 2p (a) and Tb 4d (b) of an $TbMnO_3$ thin film deposited on an $SrTiO_3$ substrate.

References

[1] Y. M. Cui, L. W. Zhang, C. C. Wang, and G. L. Xie, C. P. Chen, B. S. Cao, App. Phys. Lett. **86** (2005) 203501].

[2] M. Fujimura, N. Shigemitsu, T. Takahashi, A. Ashida, T. Yoshimura, H. Fukumura, and D. Harima, Philosophical Magazine Letters **87** (2007) 193.

[3] T. H. Lin, H. C. Shih, C. C. Hsieh, C.W. Luo, J.-Y. Lin, J. L. Her, H. D. Yang, C.-H. Hsu, T.M. Uen, and J. Y. Juang, J. Phys.: Condens. Mat. **21** (2009) 026013]

[4] S. Morup, D. E.Madsen, C. Frandsen, C. R. H. Bahl, andM. F. Hansen, J. Phys.: Condens. Mat. **21** (2007) 3202].

[5] J. A. Alonso, M. J. Martinez-Lope, M. T. Casais, and M. T. Fernandez Diaz, Inorg. Chem. **39**, 917 (2000).

[6] X. Marti, V. Skumryev, A. Cattoni, A. Bertaco, V. Laukhin, C. Ferrater, M. García-Cuenca, M. Varela, F. Sánchez, and J. Fontcuberta, J. of Magn. And Magn. Mat. **321** (2009) 1719]

[7] F. Perez-Osuna, J. M. Siqueiros, A. Dur_an, M. P. Cruz, L. Salamanca Riba, and J. Heiras, J. Appl. Phys. **112**, 033914 (2012).

[8] X. Marti, V. Skumryev, C. Ferrater, M. V. García-Cuenca, M. Varela, F. S_anchez, and J. Fontcuberta, Appl. Phys. Lett. **96**, 222505 (2010).

[9] D. Rubi, C. de Graaf, C. J. M. Daumont, D. Mannix, R. Broer, and B. Noheda, Phys. Rev. B. **79**, 014416 (2009).

[10] A. R. Akbarzadeh, L. Bellaiche, J. Iniguez, and D. Vanderbilt, Appl. Phys. Lett. **90**, 242918 (2007).

[11] D. Meier, N. Allouane, D. N. Argyriou, J. A. Mydosh, and T. Lorenz, New J. Phys. **9**, 100 (2007).

[12] T. Goto, Y. Yamasaki, H. Watanabe, T. Kimura, and Y. Tokura, Phys. Rev. B. **72**, 220403 (2005).

[13] B. J. Kirby, D. Kan, A. Luykx, M. Murakami, D. Kundaliya, and I. Takeuchi, J. Appl. Phys. **105**, 07D917 (2009).

[14] A. Vailionis, H. Boschker, W. Siemons, E.P. Houwman, D.H.A. Blank, G. Rijnders, G. KosterA, H.Vailionis, W. Boschker, E.P. Siemons, D.H.A. Houwman, G. Blank, G.Koster Rijnders, Phys. Rev. B **83**, 064101 (2011)

[15] J. Blasco, C. Ritter, J. García, J.M. de Teresa, J. Pérez-Cacho, M.R. Ibarra, Phys. Rev. B **62**, 5609 (2000)

[16]. N. Aliouane, D. N. Argyriou, J. Strempfer, I. Zegkinoglou, S. Landsgesell, M. V. Zimmermann, Phys. Rev. B **73**, 020102R (2006)

[17]. Y. Cui, C. Wang, B. Cao, Solid State Commun. **133**, 641 (2005)

[18]. R. Tackett, G. Lawes, B.C. Melot, M. Grossman, E.S. Toberer, R. Seshadri, Phys. Rev. B **76**, 024409 (2007)

[19]. Y. Konishi, Z. Fang, M. Izumi, T. Manako, M. Kasai, H. Kuwahara, M. Kawasaki, K. Terakura, Y. Tokura, J. Phys. Soc. Jpn. **68**, 3790 (1999)

[20]. H.J. Xiang, S.-H. Wei, M.-H. Whangbo, J.L.F.D. Silva, Phys. Rev. Lett. **101**, 037209 (2008)

[21]. N. Pertsev, A. Tagantsev, N. Setter, Phys. Rev. B **61**, R825 (2000)

[22] C. Daumont, Ph.D thesis, University of Groningen (Netherlands), 2009

[23] S. Venkatesan, C. Daumont, B. J. Kooi, B. Noheda, and J. T. M. D. Hosson, Phys. Rev. B **80** (2009) 214111.

[24] M. Babei and D. K. Ross, Physica C: Superconductivity **425** (2005) 130.

[25] R. D. Shannon, Acta Crystallogr. Sect. A **32** (1976) 751.

[26] V. Cuartero, J. Blasco, J.A. Rodríguez-Velamazán, J. García, G. Subías, C. Ritter, J. Stankiewicz, and L. Canadillas-Delgado, Phys. Rev. B **86** (2012)104413.

[27] A. Bombik, B. Lesnewska, J. Mayer, and A. W. Pacyna, J. Magn. Magn. Mater. **257** (2003) 206.

[28] K. Kimura, T. Goto, H. Shintani, K. Ishizka, T. Arima, and Y. Tokura, Nature (London) **426** (2003) 55.

[29] F. Jiménez-Villacorta, J. A. Gallastegui, I. Fina, X. Marti, and J. Fontcuberta, Phys. Rev. B **86** (2012) 024420.

[30] D. Sando, A. Agbelele, D. Rahmedov, J. Liu, P. Rovillain, C. Toulouse, I. C. Infante, A. P. Pyatakov, S. Fusil, E. Jacquet, C. Carrétéro, C. Deranlot, S. Lisenkov, D. Wang, J-M. Le Breton, M. Cazayous, A. Sacuto, J. Juraszek, A. K. Zvezdin, L. Bellaiche, B. Dkhil, A. Barthélémy, and M. Bibes, Nat. Mater. **12** (2013) 641.

[31] O. Prokhnenko, N. Aliouane, R. Feyerherm, E. Dudzik, A. U. B. Wolter, A. Maljuk, K. Kiefer, and D. N. Argyriou, Phys. Rev. B **81** (2010) 024419.

[32] C. Fadley, Electron Spectroscopy **781** (1972).

[33] R. P. Gupta and S. K. Sen, Phys. Rev. B **12**, 1215 (1975).

[34] F. Pérez, P.h.D. thesis, Centro de investigación científica y de educación superior de Ensenada (2013).

Conclusions

- We fabricated polycrystalline samples of the $Tb_{(1-x)}Al_xMnO_3$ system by solid-state reaction method. The introduction of Al in the bulk $TbMnO_3$ lattice decidedly modifies its physical properties. Ferromagnetic behavior was observed in Al-doped samples, which represent changes in its magnetic properties compared to those of the undoped samples.

- The effects of the partial substitution of Tb^{3+} with Al^{3+} on the electrical properties of $TbMnO_3$ were carefully studied by means of complex impedance spectroscopy at temperatures above 300 K. It was verified that the incorporation of Al ions in the $TbMnO_3$ lattice leads to increased values of the dielectric constant and the conductivity.

- We have presented a systematic study of the resistivity, thermopower, and thermal conductivity of polycrystalline $Tb_{1-x}Al_xMnO_3$ (x =0-0.2). The transport properties indicated that $Tb_{1-x}Al_xMnO_3$ is p-type semiconductor over the entire temperature range measured. The polaronic model gave an adequate description of the temperature dependence of the resistivity and thermopower.

- Compressively strained thin films of $Tb_{1-x}Al_xMnO_3$ and $TbAMn_{1-x}Al_xO_3$, with thicknesses of ~100 nm were successfully grown on $SrTiO_3$ substrates by the sputtering technique. The films were single phase and (00ℓ)-oriented Although epitaxial strain contributes to the weak ferromagnetism found in undoped TMO films, the larger values of t M_r, M_s, and H_c (0.3 T) of the doped samples suggest that the Al-doping decidedly improves the magnetic performance of TMO. Nevertheless, the mechanism behind this effect need further investigation.

List of publications

1. A. Astudillo, J. Izquierdo, F. J. Bonilla, G. Bolaños, and O. Morán, "Emergence of ferromagnetism in $TbMnO_3$ bulk by Al-doping", IEEE Trans. Magn., **49** (2013) 4590.

2. J.L. Izquierdo, G. Bolaños, V.H. Zapata, O. Morán, "Dielectric relaxation and ac conduction in multiferroic $TbMnO_3$ ceramics: impedance spectroscopy analysis", Curr. Appl. Phys., **14** (2014) 1492.

3. J. Izquierdo, A. Astudillo, G. Bolaños, O. Arnache, and O. Morán, "Ferromagnetic response of multiferroic $TbMnO_3$ films mediated by epitaxial strain and chemical pressure", J. Appl. Phys., **115** (2014) 17D909.

4. J.L. Izquierdo, A. Forero, G. Bolaños, V.H. Zapata, O. Morán, "Role of aluminum ions on the dielectric and conducting properties of multiferroic $Tb_{1-x}Al_xMnO_3$: study at high temperatures", Solid State Sci., **38** (2014) 62.

5. J.L. Izquierdo, A. Astudillo, G. Bolaños, A. Gómez, O. Arnache, C. Parra, and O. Morán, "Evidence of Ferromagnetic Response of $TbMnO_3$ Thin Films at High Temperatures", J. Low. Tem. Phys., **179** (2015) 48.

6. J.L. Izquierdo, G. Bolaños, O. Morán, "Effect of the Al-doping on the electrical and thermoelectric response of $TbMnO_3$ polycrystalline samples: evidence of polaronic transport", J. Alloys Compd., **652** (2015) 292.

7. J.L. Izquierdo, A. Astudillo, G. Bolaños, V.H. Zapata, O. Morán, "Dielectric response of Al-substituted multiferroic $TbMnO_3$ at high temperatures", Ceram. Int., **41** (2015)1285.

Participations

• 58th Conference on Magnetism and Magnetic Materials, Denver, Colorado, Nov 4-8, 2013.

• Latin American Workshop on Magnetism, Magnetic Materials and their Applications (X-LAW3M), Buenos Aires, Argentina, April 8-12, 2013.

• 21th Latin American Symposium On Solid State Physic (SLAFES XXI), Villa de Leyva, Colombia, September 30st to October 4st of 2013.

• Advanced Topics in Magnetism and Superconductivity (ATOMS 2014), San Carlos de Bariloche, Argentina, July 31st to August 4st of 2014.

Perspectives

- To fabricate $Tb_{1-x}A_xMnO_3$-based condensators in order to measure the possible ferroelectric and dielectric properties of $Tb_{1-x}Al_xMnO_3$ in thin film form.
- To characterize the dielectric properties of the $Tb_{1-x}Al_xMnO_3$ and $TbMn_{1-x}Al_xO_3$ thin films.
- To study the magnetoelectric properties both in bulk form and thin films.